

# Effect of Hydrofoil Trailing Edge Geometry on the Wake Dynamics

THÈSE N° 5218 (2012)

PRÉSENTÉE LE 20 JANVIER 2012

À LA FACULTÉ SCIENCES ET TECHNIQUES DE L'INGÉNIEUR  
LABORATOIRE DE MACHINES HYDRAULIQUES  
PROGRAMME DOCTORAL EN MÉCANIQUE

ÉCOLE POLYTECHNIQUE FÉDÉRALE DE LAUSANNE

POUR L'OBTENTION DU GRADE DE DOCTEUR ÈS SCIENCES

PAR

**Amirreza ZOBEIRI**

acceptée sur proposition du jury:

Dr F. Maréchal, président du jury  
Prof. F. Avellan, Dr M. Farhat, directeurs de thèse  
Prof. E. Egusquiza, rapporteur  
Dr J. Koutnik, rapporteur  
Prof. A. Spadoni, rapporteur



ÉCOLE POLYTECHNIQUE  
FÉDÉRALE DE LAUSANNE

Suisse  
2012





*To my incredible parents, Farideh and Mahmoud  
To my lovely wife, Atefeh*



*If your result needs a statistician  
then you should design a better experiment*

Ernest Rutherford,  
Physicist



# Acknowledgements

Foremost, I would like to express my sincere gratitude to my advisors Prof. François Avellan and Dr. Mohamed Farhat for the continuous support of my PhD study and research, for their patience, motivation, enthusiasm, and immense knowledge. Their guidance helped me in all the time of research and writing of this thesis.

Besides my advisors, I would like to thank the rest of my thesis committee: Dr. François Maréchal, Prof. Eduard Egusquiza, Dr. Jiri Koutnik, and Prof. Alessandro Spadoni, for their encouragement, insightful comments, and nice questions.

I would like to thank the HYDRODYNA partners with ALSTOM Hydro, ANDRITZ Hydro, VOITH Hydro and UPC-CDIF, Swiss Federal Commission for the Technology and Innovation (CTI), Swisselectric Research, and Swiss Competence Center of Energy and Mobility (CCEM) for their financial support.

During this work I have collaborated with many colleagues for whom I have great regard, and I wish to extend my warmest thanks to all those who have helped me with my work in the Laboratory for Hydraulic Machine (LMH) like Philippe, Vlad, Marc, Francisco, Andrey, Mattieu, and Christian.

It was a pleasure to share doctoral studies and life with wonderful people like Oliver, Stefan, Cécile, Sébastien, Pierre, Christophe, Nicolas, Steven, Martin, Martino, Danail, Ebrahim, Olivier, Andres and Christian.

I thank the rest of Laboratory for Hydraulic Machine at the EPFL including the mechanical group, especially Mr. Louis Bezencon, the design group, and GEM group. I like to thank also Isabelle, and Dr. Philippe Cerutti for their help with the administrative, and informatics.

I must acknowledge as well the many friends, colleagues, students, teachers, archivists, and other librarians who assisted, advised, and supported my research and writing efforts over the years.

My deepest gratitude goes to my family for their unflagging love and support throughout my life; this dissertation is simply impossible without them. I am indebted to my father for his care and love. I remember his constant support when I encountered difficulties. He is always my role model in my life. I cannot ask for more from my mother, as she is simply perfect. I have no suitable word that can fully describe her everlasting love to me. Mother, I love you. My special gratitude is due to my brothers, Ali and Omid, my sister, Elnaz, my sister-in-law, Faezeh, my brother-in-law, Mohamed hossein, and my parent-in-law for their support.

I owe my loving thanks to my wife Atefeh for providing a loving environment for me. Without her encouragement and understanding it would have been impossible for me to finish this work. I love you my angle.

# Résumé

Cette étude concerne l'influence de la géométrie du bord de fuite d'un hydrofoil sur la réduction des vibrations dues au détachement tourbillonnaire dans le sillage. Cela conduira à une meilleure description des phénomènes physiques réduisant les vibrations lors de l'utilisation d'un bord de fuite oblique ou de type Donaldson par rapport à un bord de fuite tronqué droit. Pour cela, des hydrofoils Naca 0009 avec un bord de fuite oblique ou de Donaldson sont testés à hautes vitesses et angle d'incidence nul, dans la veine d'essais du tunnel de cavitation à grande vitesse de l'EPFL-Laboratoire de Machines Hydrauliques. L'hydrofoil avec le bord de fuite tronqué fait office de référence dans la caractérisation des autres profils. Les moyens expérimentaux comprennent un vibromètre laser, des mesures de vitesse par laser Doppler (LDV) et par images de particules (PIV), ainsi qu'une caméra digitale à haute vitesse. La décomposition orthogonale en modes propres (POD) est utilisée pour extraire les structures cohérentes des données obtenues par PIV. De plus, les effets d'un déclenchement de couche limite turbulente sur les caractéristiques du sillage sont étudiés et comparés avec une transition de couche limite naturelle.

Une diminution significative des vibrations est constatée dans les cas des bords de fuite obliques et de Donaldson en comparaison avec le cas tronqué; un minimum est atteint pour un bord de fuite de Donaldson. Les vidéos à hautes vitesses montrent clairement que, pour les trois hydrofoils testés, les tourbillons se détachent alternativement du côté haute et basse pression du bord de fuite. Toutefois, pour le profil avec un bord de fuite oblique ou de Donaldson, le point de séparation du tourbillon inférieur est distinctement déplacé en amont par rapport au tourbillon supérieur. Cette particularité amène le point d'enroulement du tourbillon supérieur à coïncider avec le passage du tourbillon inférieur, ce qui entraîne leur collision. Cette forte interaction conduit à une redistribution de la vorticit , qui ne se concentre alors plus dans le coeur des tourbillons de Karman. Le d phasage spatial entre le point de s paration du tourbillon sup rieur et inf rieur est cependant diff rent dans le cas du bord de fuite oblique et de Donaldson, d    la libert  qu'  l' coulement pour se s parer du profil avec ce dernier.

Des mesures LDV moyenn es sur la phase des oscillations en condition de lock-in ont  t  r alis es pour les profils au bord de fuite tronqu  droit, oblique et de Donaldson. Le bord de fuite tronqu  droit pr sente un sillage sym trique alors que, dans le cas des bords de fuite obliques et de type Donaldson, un  paississement asym trique du sillage est observ . Dans le cas du bord de fuite tronqu  droit, les tourbillons sup rieurs et inf rieurs ont le m me diam tre, tandis qu'avec un bord de fuite oblique, le vortex inf rieur pr sente un diam tre plus important que son homologue sup rieur. Dans le cas du bord de fuite de Donaldson, les mesures LDV moyenn es sur la phase des oscillations sont effectu es avec une couche limite turbulente d clench e, afin d'avoir une amplitude suffisante pour d tecter ladite phase. Les mesures montrent le passage d'un tourbillon dans le sillage

proche après la collision, contrairement au cas d'un bord de fuite oblique. Cependant, le passage des deux tourbillons, correspondants aux tourbillons supérieurs et inférieurs, se trouve loin du bord de fuite avec l'utilisation d'une coupe de Donaldson. Les mesures LDV montrent que la collision des tourbillons observée lors du lock-in vaut également en condition de lock-off pour les profils ayant un bord de fuite oblique ou de Donaldson.

La comparaison des profils de vitesse dans la zone de formation des tourbillons montre qu'avec la coupe de Donaldson, la largeur du sillage augmente considérablement par rapport aux deux autres types de bord de fuite. Le minimum de fluctuation de vitesse est d'ailleurs obtenu pour un bord de fuite de Donaldson. La similarité des résultats obtenus en condition de lock-in et de lock-off indique que la collision entre les tourbillons supérieurs et inférieurs, bien visible lors du lock-in, se produit également en condition de lock-off.

Cette collision entre les tourbillons supérieurs et inférieurs est également observée pour une couche limite turbulente, à la différence que le diamètre du tourbillon est plus grand et que la fréquence de lâché est plus petite que dans le cas d'une transition de couche limite naturelle.

Ces observations nous incitent à croire que la collision entre les tourbillons supérieurs et inférieurs, ainsi que la redistribution de vortacité qui en résulte, est la principale raison de la réduction des vibrations obtenue avec les bords de fuite obliques et de type Donaldson. Ce résultat ouvre la voie à d'avantage d'optimisation de la géométrie des hydrofoils pour une nouvelle réduction des vibrations.

**Mots-clés:** Allée tourbillonnaire de von Kármán, cavitation, couche limite, détachement tourbillonnaire, lock-in, lock-off, résonance, sillage, transition de couche limite, vibration



# Abstract

In the present study, the effect of a hydrofoil trailing edge shape on the wake dynamic and its interaction with the mechanical structure is investigated. This would help better describe the physical reasons for vibration reduction when using oblique and Donaldson trailing edges in comparison to a truncated trailing edge and subsequently allow its further optimization. Thus, hydrofoils with oblique and Donaldson trailing edges are tested in a high-speed cavitation tunnel at zero angle of attack and high Reynolds numbers,  $Re_L = 5 \cdot 10^5 - 3 \cdot 10^6$ . The truncated trailing edge hydrofoil is selected as reference. A velocity survey is performed via Laser Doppler Velocimetry, LDV, and Particle Image Velocimetry, PIV. Proper-Orthogonal-Decomposition, POD, is used to extract coherent structures from PIV data. In addition, flow induced vibration measurements and high-speed visualizations are performed. Finally, the effects of a tripped boundary layer transition on the wake are investigated and compared with the natural boundary layer transition.

Vortex-induced vibration is found to decrease significantly for oblique and Donaldson trailing edges in comparison to the truncated case, specially under lock-off condition. However, minimum vibration corresponds to the Donaldson trailing edge. The high-speed videos clearly show that for three tested hydrofoils the alternate vortices clearly detach from suction and pressure sides of the trailing edge. However, for the oblique and Donaldson trailing edges the location of the lower vortex detachment is obviously shifted upstream with respect to the upper one. As a result, when the upper vortex rolls up, it coincides with the passage of the lower vortex, leading to their collision. This strong interaction leads to a redistribution of the vorticity, which does not concentrate within the core of Karman vortices any more. However, the spatial phase shift between the separation point of the upper and the lower vortices is different in the case of oblique and Donaldson trailing edges due to the being free the separation point on the Donaldson curve.

LDV phase-locked averaging under lock-in condition is performed for truncated, oblique and Donaldson trailing edges. The truncated trailing edge exhibits a symmetric wake. However, in the case of the oblique and Donaldson trailing edges, an asymmetric thickening of the downward near wake is observed. The stream wise velocity fluctuation shows two peaks of different amplitudes. In the case of the truncated trailing edge, the upper and lower vortices have the same core diameter, contrary to the oblique trailing edge, where a larger vortex core diameter is found for the lower vortex. In the case of Donaldson trailing edge, the LDV phase-locked averaging is performed for the tripped transition where the vibration amplitude is high enough to perform the phase-locked average. The measurements show the passage of one vortex after the collision in the near wake contrary to the oblique one. However, the passage of two vortices corresponding to the upper and lower vortex is found far from the Donaldson trailing edge.

LDV measurements show that the collision of the vortices for the oblique trailing edge, observed under lock-in conditions, also prevails for the lock-off condition in the case of oblique and Donaldson trailing edges. The velocity profile comparison at the vortex formation length for three trailing edges shows that in the case of the Donaldson trailing edge, the wake width increases significantly in comparison to two other trailing edges. Moreover, the minimum stream wise and transverse velocity fluctuation profiles obtained for the three trailing edges correspond to the Donaldson trailing edge. The strong similarity of results obtained for lock-in and lock-off conditions indicates that the collision between upper and lower vortices, clearly observed under lock-in, also occurs for lock-off condition.

A thicker boundary layer with laminar-to-turbulent transition occurring further upstream is observed for the pressure side of the Donaldson trailing edge in comparison with the suction side. In contrast to the truncated trailing edge, both sides have a similar boundary layer structure and a similar transition location. Moreover, a thicker boundary layer is found for the Donaldson trailing edge in comparison to the truncated case.

The collision between upper and lower vortices is also observed in the case of a tripped transition. However, the vortices are shed with a larger core diameter, greater strength, and lower frequency than for the natural transition.

These investigations let us believe that the collision between upper and lower vortices and the resulting vorticity redistribution is the main reason for the vibration reduction obtained with oblique and Donaldson trailing edges. This result opens the way for more effective hydrofoil geometry optimization for further reduction of flow induced vibration.

**Keywords:** Vortex-induced vibration, vortex shedding, wake, boundary layer, boundary layer tripping, trailing edge geometry, lock-in, lock-off

# Contents

<b>I</b>	<b>Introduction</b>	<b>1</b>
<b>1</b>	<b>Problem overview</b>	<b>3</b>
1.1	Flow past a bluff body . . . . .	4
1.1.1	Vortex shedding and wake . . . . .	4
1.1.2	Vortex street stability . . . . .	5
1.1.3	Overview of regimes . . . . .	6
1.2	Flow-induced vibration . . . . .	8
1.2.1	Lock-in . . . . .	8
1.2.2	Strouhal number . . . . .	9
1.3	Wake flow control . . . . .	10
1.3.1	Control of flow-induced vibration . . . . .	10
1.4	Boundary layer . . . . .	15
1.4.1	Boundary layer definition . . . . .	15
1.4.2	Laminar boundary layer . . . . .	16
1.4.3	Laminar-to-turbulent transition boundary layer . . . . .	17
1.4.4	Turbulent boundary layer . . . . .	19
1.4.5	Boundary layer separation . . . . .	20
1.5	Purpose of the present work . . . . .	21
1.6	Structure of the document . . . . .	22
<b>II</b>	<b>Case study and experimental setup</b>	<b>23</b>
<b>2</b>	<b>Test facility and case study</b>	<b>25</b>
2.1	High speed cavitation tunnel . . . . .	25
2.2	Experimental hydrofoil . . . . .	27
2.2.1	Leading edge roughness . . . . .	31
<b>3</b>	<b>Measurement techniques</b>	<b>33</b>
3.1	Vortex-induced vibration measurement . . . . .	33
3.1.1	Accelerometer . . . . .	33
3.1.2	Laser Doppler vibrometer . . . . .	34
3.1.3	Data acquisition system . . . . .	35
3.2	Hydrodynamic load cell . . . . .	35
3.3	Flow measurement . . . . .	36
3.3.1	Laser Doppler velocimetry . . . . .	36
3.3.2	Particle Image Velocimetry . . . . .	40

3.4	Flow visualization . . . . .	43
<b>III</b>	<b>Results and Analysis</b>	<b>45</b>
<b>4</b>	<b>Effect of trailing edge shape on boundary layer</b>	<b>47</b>
4.1	Development along the hydrofoil chord . . . . .	47
4.1.1	Boundary layer thickness . . . . .	49
4.1.2	Boundary layer structure . . . . .	50
4.2	Development at trailing edge . . . . .	51
4.2.1	Reynolds effects on the velocity profile thickness at trailing edge .	51
<b>5</b>	<b>Effect of trailing edge shape on vortex-induced vibration</b>	<b>53</b>
5.1	Vibration amplitude . . . . .	53
5.2	Vortex shedding frequency and Strouhal number . . . . .	55
<b>6</b>	<b>Effect of trailing edge shape on vortex formation mechanism</b>	<b>59</b>
6.1	Lock-in . . . . .	60
6.2	Lock-off . . . . .	63
<b>7</b>	<b>Effect of trailing edge shape on wake flow</b>	<b>65</b>
7.1	Wake flow under lock-in condition . . . . .	65
7.1.1	Time-averaged velocity profiles . . . . .	65
7.1.2	Velocity profiles at the passage time of the vortex . . . . .	68
7.1.3	Vortex properties . . . . .	68
7.1.4	Inter-vortex spacings . . . . .	72
7.2	Wake flow under lock-off condition . . . . .	74
7.2.1	Time-averaged velocity profiles . . . . .	75
<b>IV</b>	<b>Effect of boundary layer state on the wake dynamics</b>	<b>79</b>
<b>8</b>	<b>Effect of trailing edge shape on vortex-induced vibration</b>	<b>81</b>
8.1	Vibration amplitude . . . . .	81
8.2	Vortex shedding frequency and Strouhal number . . . . .	81
8.3	Flow visualization . . . . .	85
<b>9</b>	<b>Effect of trailing edge shape on wake flow</b>	<b>89</b>
9.1	LDV phase-locked average: Lock-in . . . . .	89
9.1.1	Instantaneous velocity profiles at the passage time of the vortex .	89
9.1.2	Vortex characteristics . . . . .	93
9.2	Time-averaged velocity profiles . . . . .	95
<b>V</b>	<b>Conclusions and Perspectives</b>	<b>97</b>
<b>10</b>	<b>Conclusions</b>	<b>99</b>

<b>11 Perspectives</b>	<b>101</b>
<b>References</b>	<b>105</b>
<b>Curriculum Vitae</b>	<b>111</b>



# Notations

## Latin

$a_s$	Stream-wise inter-vortex spacing	[m]
$b_s$	Cross-stream inter-vortex spacing	[m]
$f_s$	Vortex shedding frequency	[Hz]
$f_n$	Hydrofoil natural frequency	[Hz]
$l_f$	Vortex formation region length	[m]
$h$	Hydrofoil thickness	[m]
$h_t$	Hydrofoil trailing edge thickness	[m]
$p_{ref}$	Static pressure at the test section inlet	[Pa]
$p_v$	Saturation vapor pressure	[Pa]
$t$	Time	[s]
$y_f$	Wake width	[m]
$B$	Hydrofoil span	[m]
$L$	Hydrofoil chord	[m]
$C_{ref}$	Velocity at the test section inlet, free-stream velocity	[m/s]
$C_{x_{mean}}$	Mean stream-wise velocity	[m/s]
$C_{y_{mean}}$	Mean transverse velocity	[m/s]
$C_{x_{stdv}}$	Fluctuating stream-wise velocity	[m/s]
$C_{y_{stdv}}$	Fluctuating transverse velocity	[m/s]

## Greek

$\alpha$	Hydrofoil angle of attack	[°]
$\delta$	Boundary-layer thickness	[m]
$\delta_1$	Boundary-layer displacement thickness	[m]
$\delta_2$	Boundary-layer momentum thickness	[m]
$\eta_i$	Transit time weighting factor	[-]
$\Gamma$	Vortex strength	[m <sup>2</sup> /s]

## Subscripts

---

<i>crit</i>	Turbulent boundary-layer transition location quantity
<i>max</i>	Maximum quantity
<i>min</i>	Minimum quantity
<i>mean</i>	Mean quantity
<i>n</i>	Eigen quantity
<i>ref</i>	Free-stream quantity
<i>stdv</i>	Standard deviation quantity
<i>s</i>	Vortex shedding quantity
<i>x, y, z</i>	Referred to cartesian directions

### Dimensionless Numbers

$Re_h$	Reynolds number	$Re_h = \frac{C_{ref} h}{\nu} [-]$
$St$	Strouhal number	$St = \frac{f_s h}{C_{ref}} [-]$
$\sigma$	Cavitation number	$\sigma = \frac{p_{ref} - p_v}{\frac{1}{2} \rho C_{ref}^2} [-]$



**Acronyms**

EPFL	Ecole Polytechnique Fédérale de Lausanne
LMH	Laboratoire de Machines Hydrauliques
CFD	Computational Fluid Dynamics
FFT	Fast Fourier Transform
LDV	Laser Doppler Velocimetry
PIV	Particle Image Velocimetry
VIV	Vortex-Induced Vibration
POD	Proper-Orthogonal-Decomposition



# Part I

## Introduction



# Chapter 1

## Problem overview

Beyond a certain value of Reynolds number, hydrodynamic instabilities develop in the wake of a bluff body leads to a periodic and alternate vortex shedding. The issue of vortex-induced vibration due to this vortex shedding phenomenon is a major problem in different domains such as hydraulic machinery, e.g. vortex shedding from stay vanes and guide vanes of a hydraulic machine, Figure 1.1. As a result, the fluctuating force transverse to the flow may lead to excessive vibrations. The structural vibration amplitude is amplified when the vortex shedding frequency coincides with one of the natural frequencies of the structure. As a result, the structure can control the vortex shedding and synchronize its frequency with the structure motion frequency for a wide range of free-stream velocities, producing what is known as the lock-in phenomenon. Under this condition, fatigue failure of the structure and premature cracks may be provoked in the hydraulic machines.

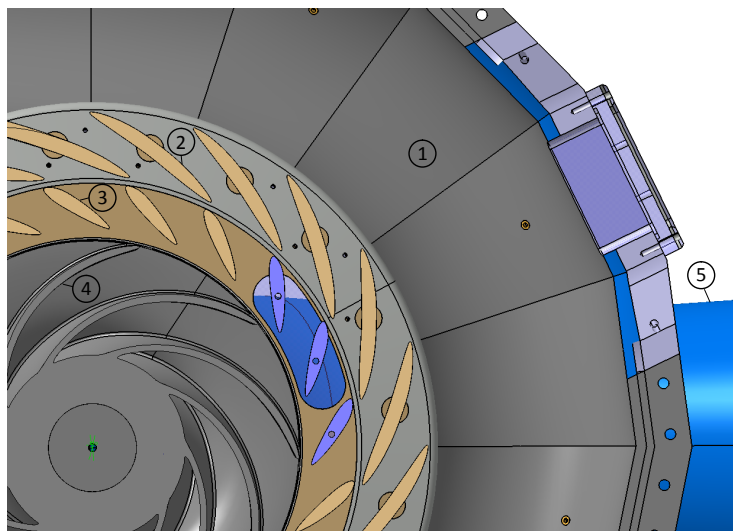


Figure 1.1: Components of a Pump-Turbine model test. 1. Spiral case, 2. Stay vanes, 3. Guide vanes, 4. Runner and 5. Diffuser

## 1.1 Flow past a bluff body

Formation of vortex streets is observed in the wake of bluff bodies over a wide range of Reynolds numbers. Consequently, the vortex shedding past a bluff body has been the main point of interest for many works, studying the physics of vortex street formation and vortex shedding regimes for different Reynolds numbers.

### 1.1.1 Vortex shedding and wake

The formation process of alternate vortices has been studied by many authors such as Roshko [64], Gerrard [25], Bearman [8], Griffin [32], and Williamson [82]. The interaction between two separating shear layers is the origin of vortex street formation. Once the vortex is generated, it grows and is fed by circulation from its connected shear layer. As the vortex becomes strong enough, it draws the opposing shear layer across the near wake. As a result, further circulation to the growing vortex is cut off by vorticity of opposite sign and the vortex is then shed downstream. Entrainment plays an important role in vortex formation. It is partly entrained into the growing vortex, *a*, entrained into the separated shear layer, *b*, and partly canceled in the next half of the shedding cycle, *c*, Figure 1.2.

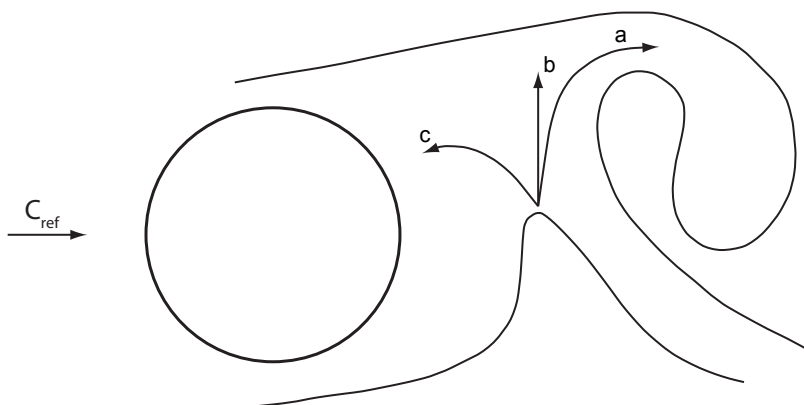


Figure 1.2: Vortex-formation model showing entrainment flows, Gerrard [25]

Several definitions have been proposed to determine the vortex formation length in the stream wise direction, Griffen [32]. The position of the maximum stream wise velocity fluctuation off or on the wake center line is commonly used as the vortex formation length,  $L_f$ , as observed in Figure 1.3, Bearman [6]. The stream wise velocity fluctuation peak becomes sharper off the wake centerline. The velocity fluctuation peak off the wake centerline appears at the same location along the wake as on the wake centerline. If the scale of the formation region is reduced, the vortex shedding frequency increases due to the shear layers coming closer together, Roshko [64]. As a result, the interaction between the shear layers is facilitated and the periodic time is reduced. Another major effect on the vortex shedding frequency is the thickness of the shear layer when it reaches the region of strong interaction at the end of the formation region, Gerrard [25]. Ausoni [3] performed an experimental investigation on turbulent vortex shedding from a blunt trailing edge hydrofoil. He found that as the Reynolds number increases, the vortex

formation length and the position of the maximum stream wise fluctuations off the wake centerline decreases. In addition, a symmetric mean stream wise and velocity fluctuation profile in the wake is observed for different Reynolds numbers. The maximum stream wise velocity fluctuation is found at core edges of the vortices farthest from the centerline. However, maximum transverse velocity fluctuation is observed on the wake centerline. Velocity survey along the wake shows that the wake width increases contrast with velocity deficit. The evolution of the Reynolds number versus vortex strength shows an increase in the vortex strength with Reynolds number.

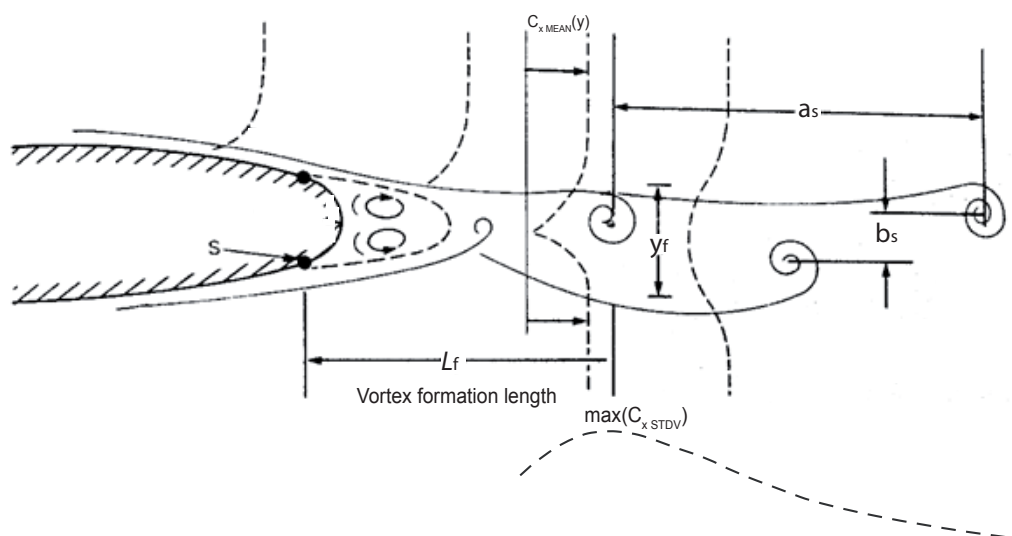


Figure 1.3: Vortex structure in the wake of a hydrofoil, Blake [13]

### 1.1.2 Vortex street stability

The first theory on stability of a vortex street was proposed by von Kàrmàn [76], who stated that two parallel rows of isolated, equal, point vortices in a non-viscous fluid is stable if the vortex arrangement is asymmetrical and the ratio between lateral and longitudinal spacing between vortices,  $\frac{b_s}{a_s}$ , is equal to 0.28. The sketch of a Kàrmàn vortex street is illustrated in Figure 1.4. Lamb [46] has shown that the symmetrical double row is unstable for all values of the ratio  $\frac{b_s}{a_s}$ . Rosenhead [62] studied the stability of a double row of vortices with arbitrary stagger,  $\frac{b_s}{a_s}$ . He stated that the only system of double rows with arbitrary stagger is Karman sreet of vortices that the stability ratio is  $\frac{b_s}{a_s}=0.28$ .

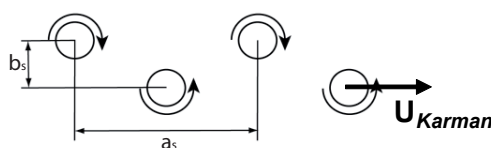


Figure 1.4: Karman vortex street

where the velocity of vortex is given as

$$U_{Karman} = \frac{\Gamma}{2a_s} \cdot \tanh \frac{\pi \cdot b_s}{a_s} \quad (1.1)$$

Different experiments have been carried out to verify von Karman's spacing prediction, [63] and [22]. In all of the experimental work, the spacing ratio,  $\frac{b_s}{a_s}$ , was found larger than Karman's spacing ratio,  $\frac{b_s}{a_s}=0.28$ . Hooker [38] studied the effect of viscosity on increasing the spacing ratio of a vortex street. The distance between consecutive vortices remains constant for any given street and the spacing ratio increases due to an increase in transverse spacing between vortices,  $b_s$ . It is due to the action of viscosity in causing the diffusion and decay of an isolated line vortex.

### 1.1.3 Overview of regimes

The overview of flow regimes in the case of a cylinder are presented by different authors such as Roshko [64], Lienhard [47], and Williamson [80]. The vortex shedding regimes behind a cylinder are defined for different ranges of Reynolds numbers given as

$$Re_d = \frac{C_{ref} D}{\nu} \quad (1.2)$$

where  $C_{ref}$  is the free-stream velocity,  $D$  is the cylinder diameter and  $\nu$  is the kinematic viscosity. The first overview of flow regimes based on measurements of velocity fluctuation, spectra and frequency is reported by Roshko [64]. Three main regimes are defined: 1) stable, periodic, laminar vortex shedding for  $Re_d = 40-150$ , 2) transition regime for  $Re_d = 150-300$  and finally 3) irregular regime for  $Re_d = 300-10000$  and higher. Similar regimes were confirmed by Bloor [14]. The overview of flow regimes across circular cylinder, proposed by Lienhard [47], are presented in Figure 1.5.

Lienhard [47] presented the flow regimes on the basis of the work of Marris [51], Kovaszny [45], Tritton [75], Schaeffer and Eskinazi [66] and Roshko [64]. The description of the regimes is as follows:

$$Re_d < 5$$

The flow is unseparated and no vortices are formed for this regime.

#### **Regime for $5 < Re_d < 40$**

A steady recirculation region of two symmetrically placed vortices on each side of the wake is observed for this flow regime. Their length grows as Reynolds number increases [69], [25].

#### **Regime for $40 < Re_d < 150$**

In this regime, the vortex street is laminar. The instabilities are developed, consequently the stretched and elongated vortices become unstable and the first periodic vortices begin.

#### **Regime for $150 < Re_d < 300$ and $300 < Re_d < 3 \cdot 10^5$**

A laminar to turbulent transition begins in the free vortex layers leaving the cylinder for  $150 < Re_d < 300$  when the Reynolds number increases. The vortex street becomes fully turbulent for  $300 < Re_d < 3 \cdot 10^5$ .



**Regime for  $3 \cdot 10^5 < Re_d < 3.5 \cdot 10^6$**

As the laminar to turbulent transition occurs in the boundary layer on the cylinder, disorganization is observed in the wake.

**Regime for  $3.5 \cdot 10^6 < Re_d < \infty$**

As the Reynolds number increases, the boundary layer laminar to turbulent transition moves upstream and boundary layer and a fully turbulent wake reestablished. In this regime a periodic vortex shedding is observed.

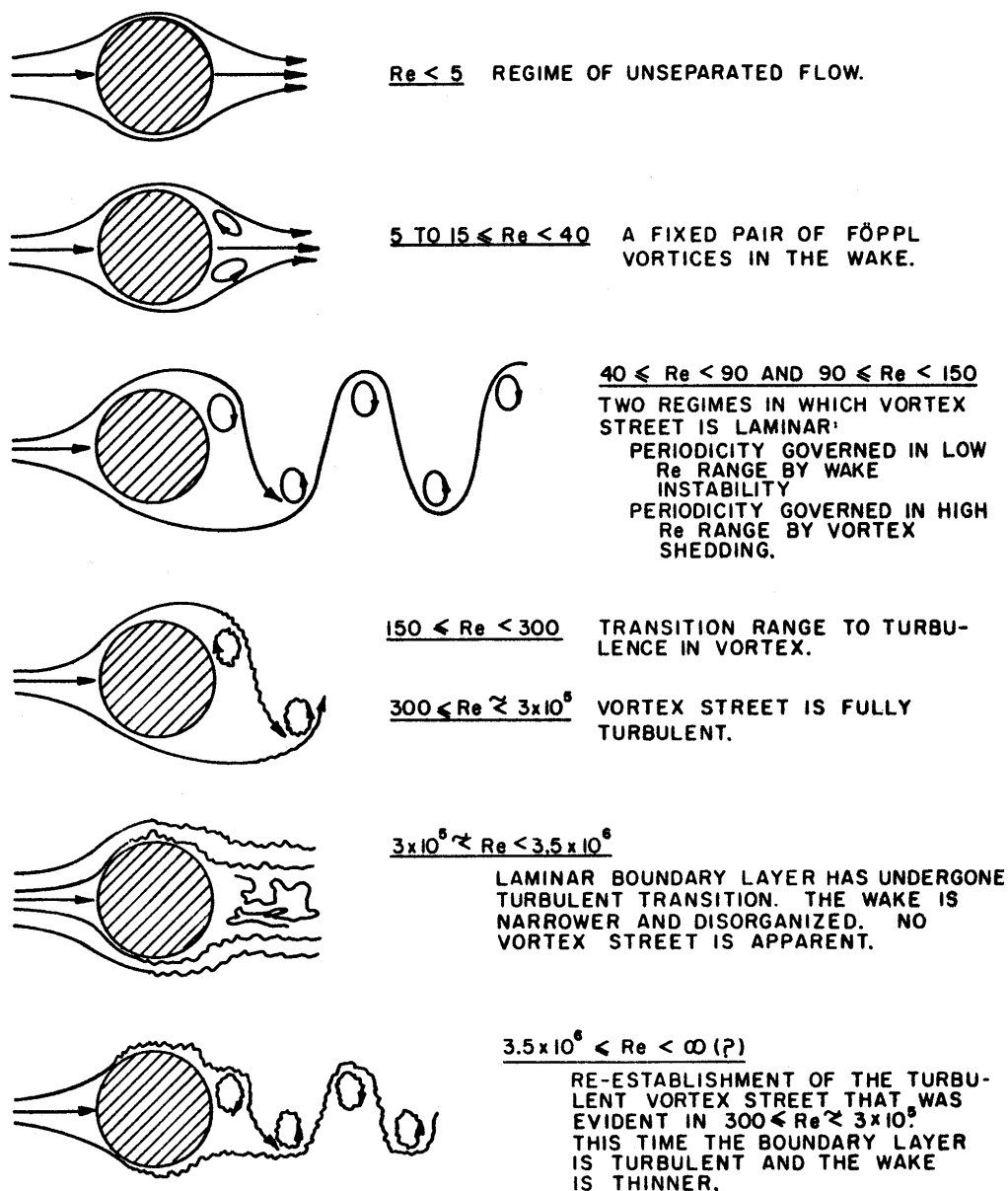


Figure 1.5: Regimes of fluid flow across circular cylinder, Lienhard [47]

## 1.2 Flow-induced vibration

A bluff body placed in a flow experiences a fluctuating force (transverse of the flow) due to the asymmetric formation of the vortices which can be a reason of structure vibration. Studying the vibration of a structure due to the vortex shedding is of interest in different fields. Different discussions of vortex-induced vibration are presented in the reviews of Rockwell [61], Sarpkaya [65], Griffen [31], Bearman [8], Williamson [81] and in a book chapter by Naudasher and Rockwell [54].

### 1.2.1 Lock-in

The coincidence of the vortex shedding frequency with the natural frequency of the structure over a range of velocity is called lock-in and it is one of the fundamental features of the flow-induced vibration. Lock-in leads to more organized wake structures and the curved vorticity lines turn into straight lines parallel to the trailing edge, leading to an increase of the fluctuating lift amplitude, Gilbert [26]. Subsequently, a significant increase of vibration amplitude is revealed under lock-in condition. The vortex formation region length decreases under lock-in condition, Kim [42]. In the resonant condition, the base suction increases in comparison to the stationary cylinder. As a result, drag increases greatly. Bearman [8] noted that the range of velocity versus the vortex-shedding frequency which is locked to the bluff body eigen frequency is dependent on oscillation amplitude. The larger the amplitude, the larger the range of the velocity. Time-averaged velocity profiles under lock-in and lock-off conditions were compared by Ausoni [3]. The maximum stream wise velocity is higher for lock-in in comparison to lock-off condition due to the traverse motion of the trailing edge for lock-in which thickens the wake. A higher vortex strength is found for lock-in as compared to the lock-off condition, in agreement with the work of Davies [16]. It is also known that the range of flow velocity leading to lock-in condition is strongly dependent on the vibration mode shape of the hydrofoil, Ausoni [3].

Certain wake flow patterns can be induced by body motion, such as the  $2S$  mode like Karman street where 2 single vortices are formed per cycle, and the  $2P$  mode where 2 vortex pairs are formed in each cycle of body motion. In addition, the  $P + S$  mode is formed only in the case of a forced vibration. The map of vortex synchronization regions for a cylinder in the wavelength-amplitude plane was presented by Williamson [82], Figure 1.6. The amplitude and wavelength ratio is introduced as the following ratios:

$$Amplituderatio = \frac{A}{D} \tag{1.3}$$

$$Wavelengthratio = \frac{C_{ref} \cdot T_e}{D} = \frac{\lambda}{D} \tag{1.4}$$

where  $C_{ref}$  is reference velocity,  $D$  is the cylinder diameter,  $T_e$  is the period of cylinder oscillation in transverse y-direction,  $A$  is the oscillating amplitude and  $\lambda$  is wavelength of the corresponding sine wave trajectory along which the body travels relative to the fluid.

The lock-in occurs at  $\frac{\lambda}{D} = 5$  where two vortices are formed each cycle and  $2S$  mode is found. In the case of  $\frac{\lambda}{D} < 5$  and  $\frac{\lambda}{D} > 5$ ,  $2S$  and  $2P$  patterns respectively are observed, Figure 1.6.

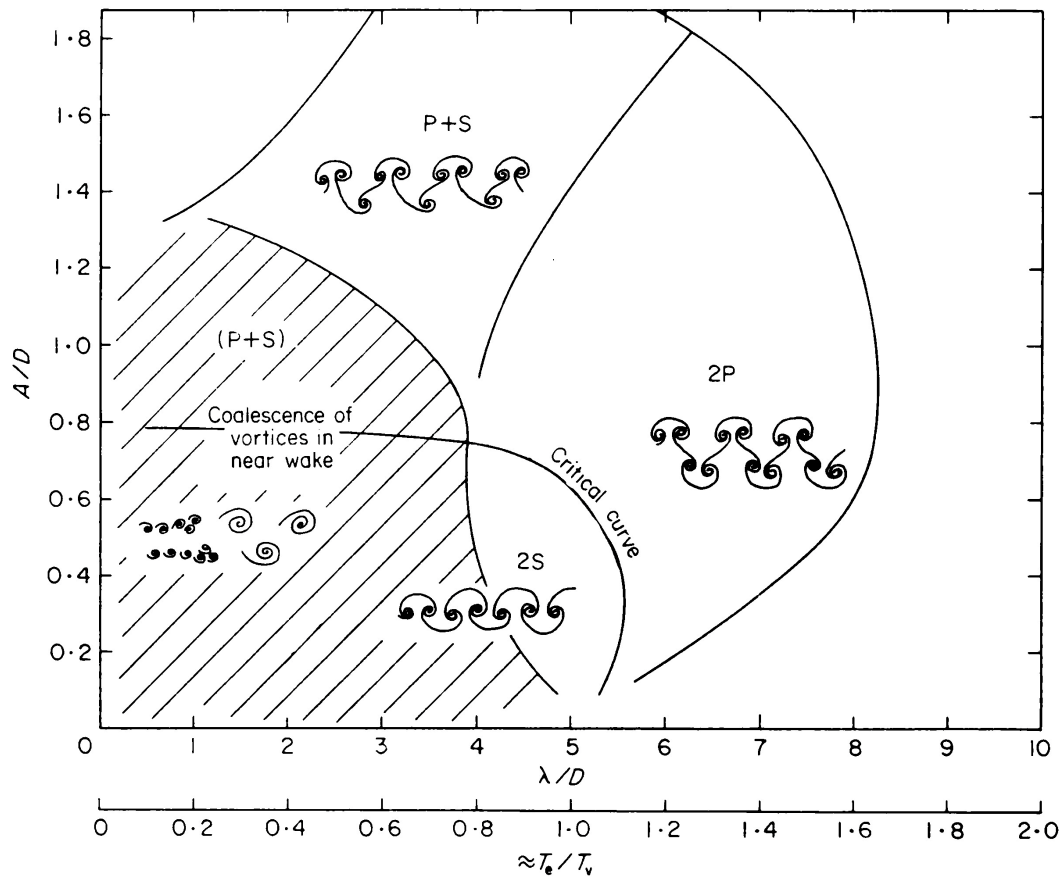


Figure 1.6: Map of vortex synchronization patterns near the fundamental lock-in region, Williamson [82]

### 1.2.2 Strouhal number

The shedding frequency of a cylinder is commonly given in terms of the Strouhal number,  $St$ , Equation (1.6).

$$St = \frac{f_s D}{C_{ref}} \quad (1.5)$$

where  $f_s$  is the vortex shedding frequency,  $D$  is the cylinder diameter, and  $C_{ref}$  is the free stream velocity. Reynolds number has an effect on the Strouhal number. The evolution of the cylinder Strouhal number versus Reynolds number is presented in Figure 1.7.

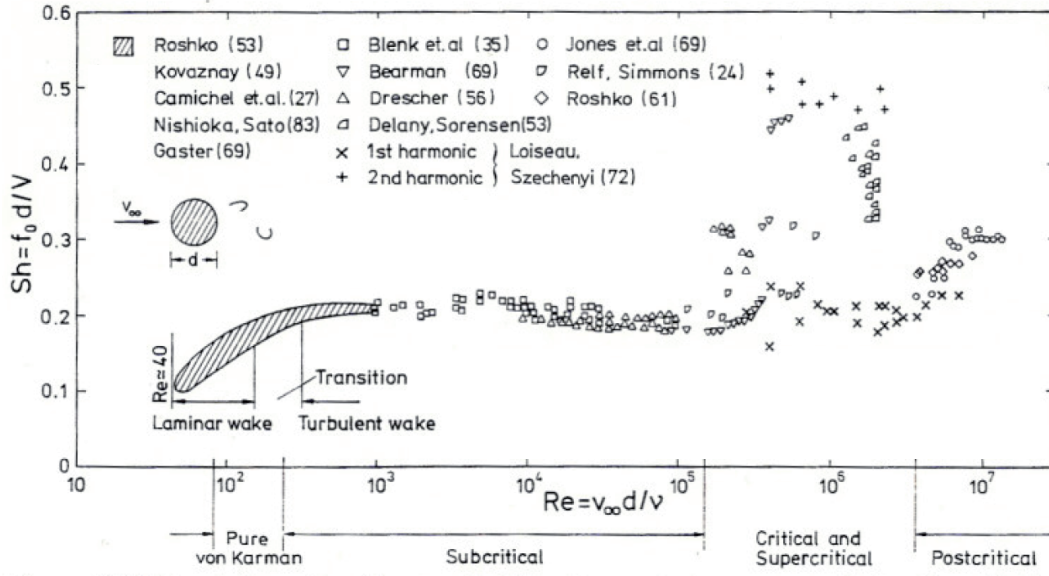


Figure 1.7: Strouhal number of vortex shedding from a smooth cylinder [54]

The frequency of vortex formation behind a cylinder may be described as a function of the Reynolds number. However, in the case of lifting surfaces the effect of viscous boundary layer on the surface and the geometry of the trailing edge should be considered. The definitions of the Strouhal number for various surface edge geometry are presented by Blake [13]. For instance, in the case of blunt trailing edge the Strouhal number can be presented as follows:

$$St = \frac{f_s \cdot (h_t + 2\delta)}{C_{ref}} \quad (1.6)$$

where  $\delta$  is the boundary layer thickness and  $h_t$  is the hydrofoil trailing edge thickness.

## 1.3 Wake flow control

Since the vortex-induced vibration can be the reason for damage in different engineering structures, a number of studies attempted to control the wake behind structures, refer to Gummer [33] for an extended review.

### 1.3.1 Control of flow-induced vibration

#### -Basic design criteria

One way to control the instability-induced excitation is to have a good design strategy. The best one is to avoid excitation altogether by modifying the system's geometry, its dynamic characteristics, or its operating conditions. As a result, neither the structure or structural part nor the fluid oscillator is excited to undergo resonant vibrations.

**-Concepts of fluid-dynamic attenuation/control of vortex shedding**

The control of the vortex shedding to reduce the vibration is presented through the following methods:

**a)Trailing edge geometry modification**

Trailing edge geometry modification in the case of the elongated bodies such as vanes, blades, and plates reduces vortex-induced excitation considerably. The effect of the trailing edge shape on the vortex-induced vibration of plates has been investigated by different authors such as Donaldson [17], Heskestad [37], Toebe [72] and Blake [13]. The summary of these studies is illustrated in the Table 1.1.

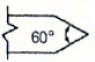
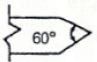
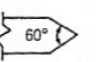
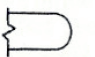

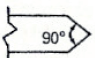
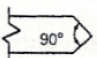
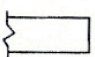
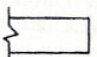
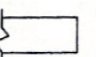
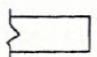
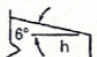
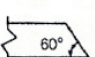
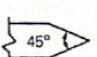
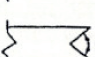
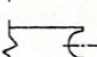
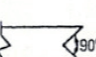

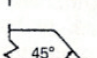

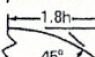
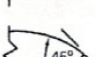

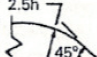
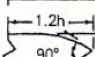
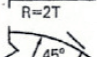
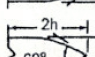
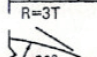

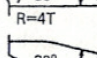
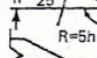
DONALDSON		HESKESTAD & OLBERTS		IPPEN		BLAKE ET AL			
GEOMETRY	REL. AMP.	GEOMETRY	REL. AMP.	GEOMETRY	REL. AMP.	GEOMETRY	REL. AMP.	$v_f/h$	$U_g/U_\infty$
	360%		380%		320%				
	260				230				
	230		190						
	100		100		100		100	0.9	1.25
							100	1.0	1.05
	48		43						
	22		31		80				
	20		38		70				
	> 1		3		60		0.3-1.5	0.5	1.05
	> 1		< 1						
	> 1		< 1				1.0	0.5	1.03
			< 1				0.5-1.7	0.8	1.2

Table 1.1: Trailing edge shapes investigated and their relative amplitude of vibration, Blake [13]

Donaldson [17] performed systematic measurements of flow-induced vibration in Francis-turbine runners having different trailing edge shapes, Figure 1.8.

It was found that none of the trailing edge shape modifications changed the frequency of the exciting forces. The vibration amplitude of different trailing edges versus velocity and also the percentage amplitude in relation to the blunt trailing edge is presented in

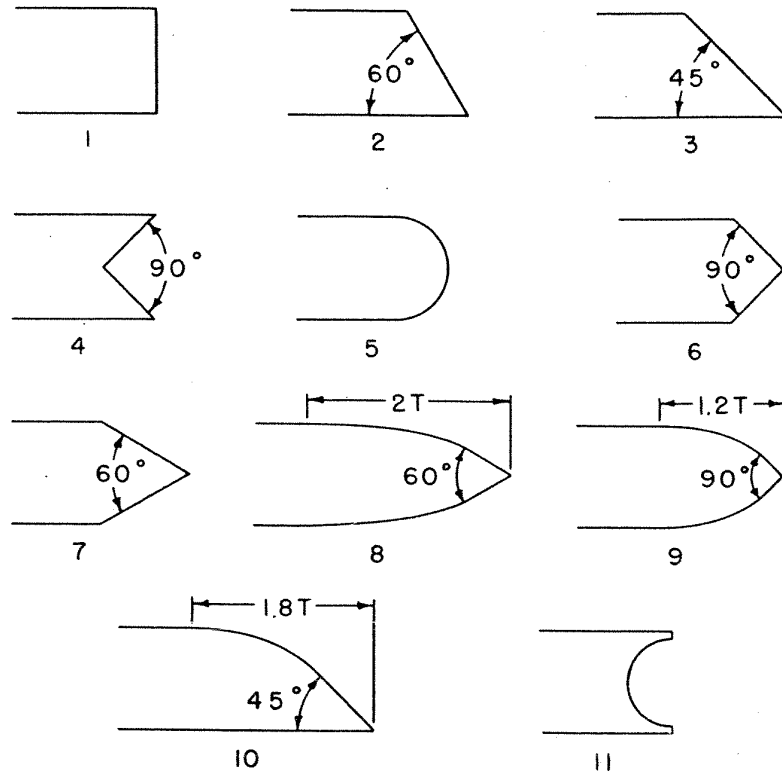


Figure 1.8: Trailing edge shape, Donaldson [17]

Figure 1.9. Minimum vibration in comparison to the blunt trailing edge was found for the trailing edge numbers 8, 9, 10.

The vortex shedding from a cambered hydrofoil with beveled trailing edge with angles of  $44^\circ$  and  $56^\circ$  at high Reynolds number was studied by Dwayne [21]. He noted that the turbulent fluctuations in the near wake depend on the Reynolds number due to the Re-dependence of separating boundary layers on both sides of the hydrofoil, interacting to form the near wake. In addition, the trailing edge geometry has an effect on the relative strength of the vortex shedding. The thicker or blunter trailing edge produces stronger vortex shedding. Moreover, the boundary layer is separated at the beveled side of the trailing edge and asymmetric vortex shedding is found. Mosallem [52] investigated the characteristics of the flow past beveled trailing edges attached to the flat plates with angles of  $27^\circ$  and  $60^\circ$ . The results display an asymmetric wake behind the  $27^\circ$  beveled trailing edge contrary to the  $60^\circ$  case where a symmetric wake is observed. Greenway [29] studied the effect of beveled trailing edge on vortex shedding and vibration using a wind tunnel. It was found that the beveled trailing edge suppressed the vortex excited vibration due to the rapid decay of the vortex resulting from an asymmetric circulation distribution in the vortex formation region. He performed the measurement for different trailing edge angles between  $20^\circ$  and  $90^\circ$ . As the trailing edge angle decreases, the vortex strength becomes smaller. In addition, the vortices shed from the suction side are stronger than those from the pressure side.

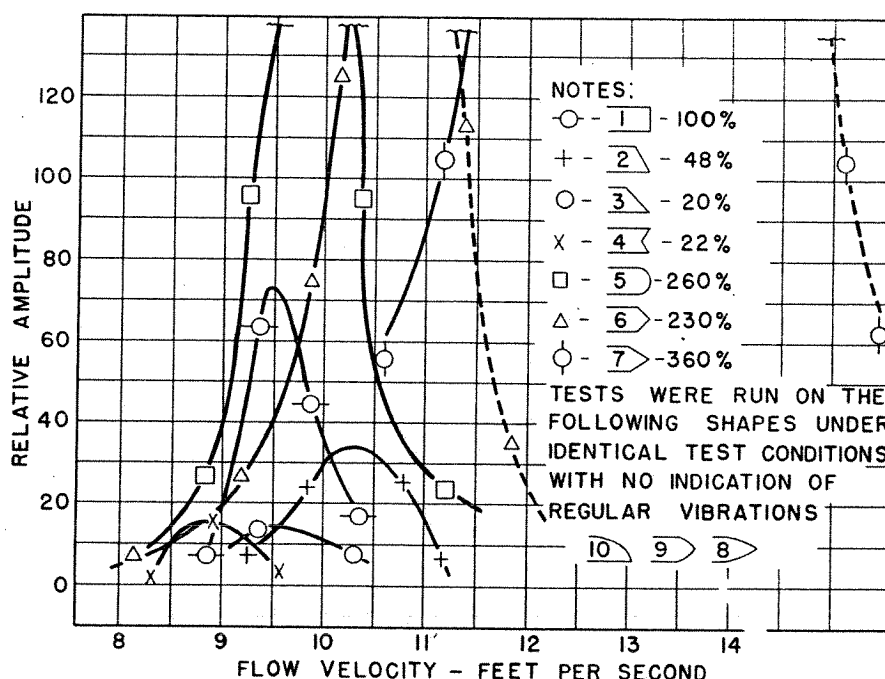


Figure 1.9: Vibration amplitude of various trailing edge shapes, Donaldson [17]

In the domain of hydraulic machine, fatigue cracks in stay vanes have occurred in several hydro power stations over the years, [33], [48], and [27]. Two basic principles are known to solve the problem, Grein [30]. The first is to modify the trailing edge to reduce the vibration excitation and the second is to alter the natural frequency of the stay vanes. A comprehensive review of stay vane cracking in hydraulic turbine has been presented by Gummer [33]. The stay vane failure in the NKula Falls hydro power plant was resolved by modification of trailing edge as reported by Fisher [24]. Locky [49] noted the vortex-induced vibration reduction in Ontario power generation by modifying the original trailing edge of stay vane to a V-shaped trailing edge. The same modification was also reported for Little Long Generation station north of Toronto by Goldwag [27].

#### b) Dephased separation (spanwise) and 3-D disturbance

Spanwise dephasing along a bluff body can enhance the regularity of vortex shedding. Staggered separation wires along a stationary circular cylinder in the critical regime,  $1.3 \cdot 10^5 < Re_d < 3.5 \cdot 10^6$  can be used to provide a spanwise dephasing, Figure 1.10a. The dephased separation from a blunt trailing edge wing (or a plate) is presented in Figure 1.10b. A reduction in base drag is found as a side benefit of this measure, Tanner [71]

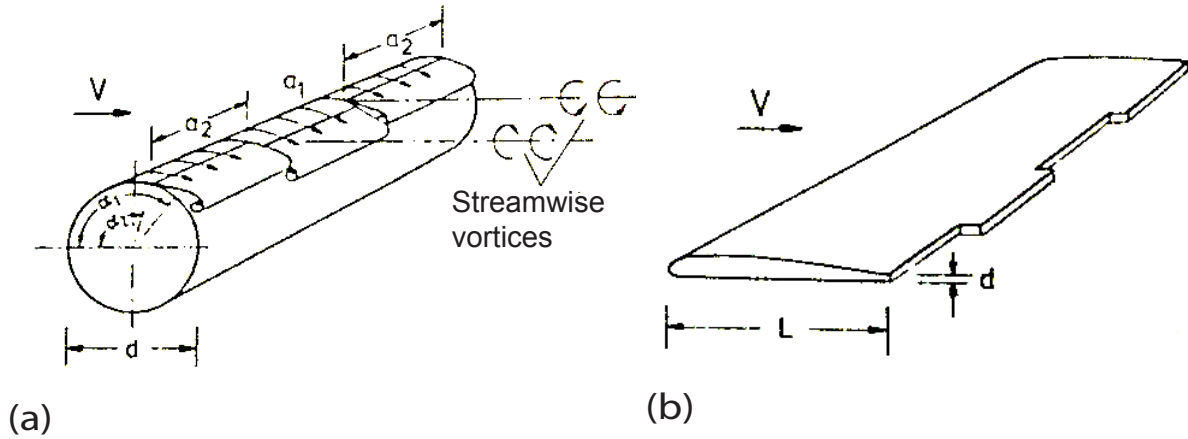


Figure 1.10: (a) Staggered separation wires on a stationary circular cylinder create strong three-dimensional disturbances, (b) Stepped trailing edge of a vane generates dephased separation with stream wise vorticity, [71]

#### c) Instability inhibition via shear-layer reattachment

*Splitter plate* either touching the cylindrical body or placed downstream is one of the earliest techniques for reducing vortex excitation. A splitter plate can significantly affect the drag and Strouhal number of vortex shedding, [25] and [64].

#### d) Instability inhibition via fluid injection

Another means of affecting the near wake region is to bleed fluid from the interior of the body into the wake, [7] and [83], as presented in Figure 1.11 where the  $V$  is the upstream velocity and  $V_i$  is the jet velocity.

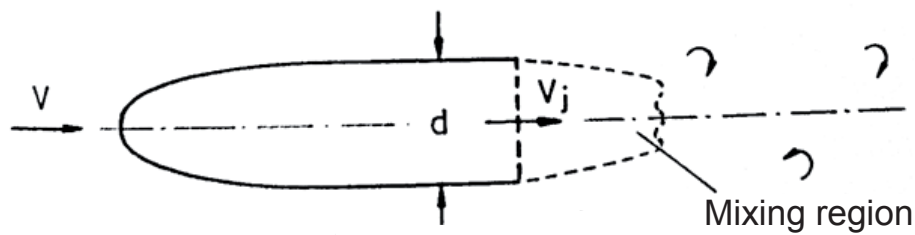


Figure 1.11: Cylindrical body bleeding fluid from the interior , [83]

Different other methods are proposed to control the wake. For instance, Bearman and Owen [9] changed the front stagnation face of a rectangular cylinder with span wise waviness to suppress vortex shedding. They could not achieve any drag reduction by installing the span wise waviness on a the rear surface of the rectangular cylinder because separation occurred at the front edge. Park [57] used small-sized tabs, mounted on part of the upper and lower trailing edges of a bluff body to attenuate vortex shedding and reduce drag. The height, width and span wise spacing between the adjacent tabs were



considered as main parameters for the measurement. Drag was reduced by attaching this simple device to the trailing edge. Moreover, the vortices shed from the upper and lower trailing edges lost their 2D nature due to tabs and vortex dislocation occurred. The Kàrmàn vortex shedding completely disappeared at low Reynolds number right behind the bluff body but to a lesser extent at further downstream locations. Other methods can be identified such as thin splitter plate, Hwang [39], Ozono [56]; rotary oscillations of a bluff body, Konstantinidis [44]; blowing and suction, Cadot [17]; geometry modification in the span-wise direction near the separation point such as a segmented trailing-edge, Rodriguez [18]; and wavy trailing-edge, Tombazis [74].

## 1.4 Boundary layer

It is well known that the vortex street is strongly related directly to the state of boundary layer along the hydrofoil. Consequently, the boundary layer is studied in this section.

### 1.4.1 Boundary layer definition

In viscous flows, a thin boundary layer appears close the surface of a body with a zero relative flow velocity right at the surface. The velocity in the boundary layer slowly increases until it reaches the outer flow velocity, Schlichting [67].

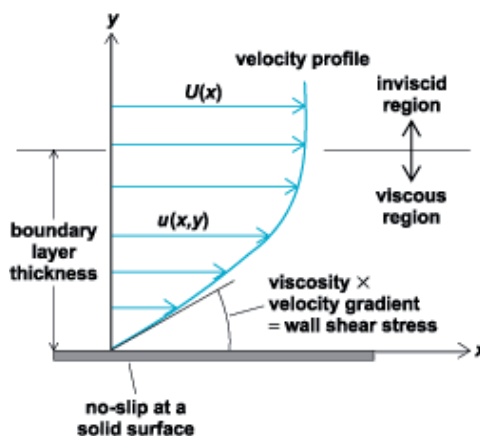


Figure 1.12: Boundary layer velocity profile

The distance required for the flow to nearly reach flow stream velocity is defined as the boundary layer thickness. In the case of a flat plate this distance is estimated to be from the body surface to 99% of free stream velocity. However, other definitions are presented for the boundary layer thickness such as displacement thickness and momentum thickness.

The displacement thickness is defined by considering the total mass flow through the

boundary layer as follow:

$$\delta_1 = \int_0^{\delta} \left(1 - \frac{C_x}{C_{ref}}\right) dy \quad (1.7)$$

The momentum thickness is defined by the following equation:

$$\delta_2 = \int_0^{\delta} \left(1 - \frac{C_x}{C_{ref}}\right) \frac{C_x}{C_{ref}} dy \quad (1.8)$$

The form factor  $H_{12}$ , defined as the ratio of the boundary-layer displacement thickness,  $\delta_1$ , and its momentum thickness,  $\delta_2$ , reveals accordingly to theoretical velocity profiles the type of boundary-layer flow, *i.e.* laminar, transitional or turbulent.

$$H_{12} = \frac{\delta_1}{\delta_2} \quad (1.9)$$

Wall shear stress is defined according to the *Newton's law of friction* [67]

$$\tau(x) = \mu \left( \frac{\partial C_x}{\partial y} \right) \quad (1.10)$$

The boundary layer develops along the surface generally passing through three flow regimes, *laminar flow*, *laminar-to-turbulent transition flow*, and *turbulent flow*, as presented in Figure 1.13.

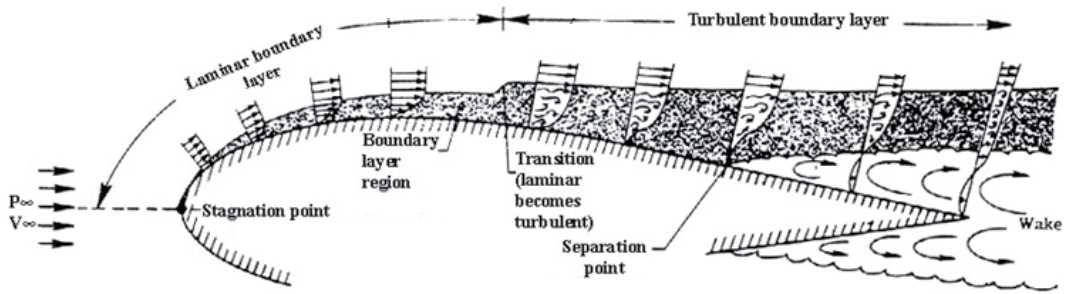


Figure 1.13: Different flow regimes on a airfoil (Courtesy of NASA)

## 1.4.2 Laminar boundary layer

In this flow regime, the flow moves in smooth layers and little mixing is observed. As a result, the velocity gradient is small and shear stress is low. As the distance along the surface increases the boundary layer thickness increases.

### 1.4.3 Laminar-to-turbulent transition boundary layer

Laminar-to-turbulent transition occurs at a critical Reynolds number,  $Re = Re_{crit}$ , which is defined as follow:

$$Re_{crit} = \frac{C_{ref} x_{crit}}{\nu} \quad (1.11)$$

where the  $x = x_{crit}$  is the critical distance from the leading edge.

The surface roughness has a effect on the critical Reynolds number. The schematic of surface roughness is illustrated in Figure 1.14., Kachanov [40]

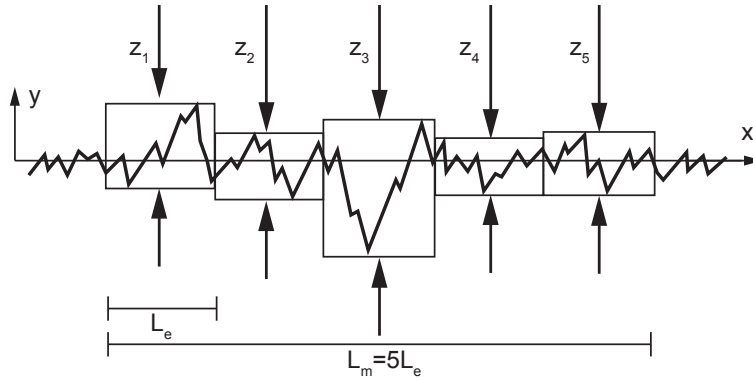


Figure 1.14: Definition of the surface roughness parameters, [3]

The surface roughness is defined as following equation:

$$R_{a_{DIN}} = \frac{1}{L_m} \int_0^{L_m} |y| dx, \quad R_{z_{DIN}} = \frac{1}{5}(z_1 + z_2 + z_3 + z_4 + z_5) \quad (1.12)$$

A surface is considered as a smooth surface if the following criterion is satisfied:

$$\frac{C_{ref} R_{z_{DIN}}}{\nu} < 100 \quad (1.13)$$

Laminar to turbulent transition in a boundary layer comprises three main stages, a)receptivity, b)linear stability and c)nonlinear breakdown as presented in Figure 1.15., Kachanov [40]. In the receptivity stage, instability waves, called Tollmien-Schlichting waves are generated. The problem of generating these waves by perturbations is referred to as the problem of boundary layer receptivity to external disturbances. In the linear stability stage of transition, the propagation of small-amplitude instability waves downstream of the boundary layer is observed. They are either amplified, if the flow is unstable, or attenuated. The flow enters a phase of nonlinear breakdown, randomization and a final transition into the turbulent state. As the amplitudes of instability waves reach considerable values, the flow is transformed from a regular two-dimensional laminar flow into a stochastic and three-dimensional turbulent flow.

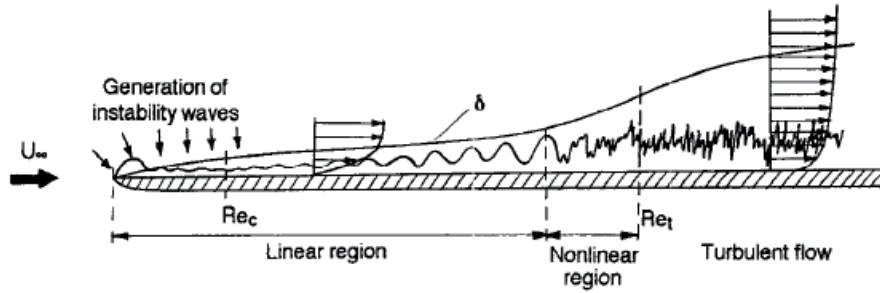


Figure 1.15: Sketch of the process of turbulent onset in a boundary layer, [40]

Different studies on the boundary layer have been performed, Benney [11], Klebanoff [43], Tani [70], and Herbert [35]. The characteristics of finite-amplitude Tollmien-Schlichting, TS, waves have been studied by Itoh [53], Herber [34], Fasel [23] and Tollmien [73]. No remarkable effect of non-linearity on disturbance growth or velocity distribution is observed at low amplitudes of TS. In addition, from a qualitative point of view, the most significant effect of TS waves is the breakup of the uniform flow in the stream wise direction. The studies of Kerho [41] show that the turbulence intensity begins to increase rapidly in the boundary layer as transition occurs. The maximum value for turbulence intensity is observed at transition; however this value decreases after transition. Low value of turbulence intensity is also observed for the laminar boundary layer. However, the turbulence intensity at the leading edge is higher than at other sections of the laminar boundary layer. Moreover, the turbulence intensity level in the transition region decreases with Reynolds number and the transition location moves towards the leading edge. According to the work of Ausoni [3], as the Reynolds number increases, the location of transition on a hydrofoil moves upstream to the leading edge and an increase in the boundary layer thickness is observed. In addition, the boundary layer thickness increases slightly with the distance from the leading edge until a transition region, where a significant increase of the boundary layer thickness is found.

The effect of leading edge roughness on the boundary layer and transition was studied by Kerho [41] and Dryden [18]. The roughness triggered the transition at an airfoil leading edge. Ausoni [3], [4] reports that the tripped transition increases the boundary layer thickness in comparison to the natural transition for a truncated trailing edge hydrofoil. Moreover, as the Reynolds number increases, the boundary layer thickness is reduced contrary to the natural transition. On the other hand, the vortex shedding frequency decreases with tripped transition. However, the vibration level rises significantly due to an increase in vortex span wise organization, and increases in vortex strength or a combination of both. The effects of surface roughness on the wake of a symmetric airfoil have been studied by Zhang [84]. By introducing the roughness on the profile the boundary layer thickness, mixing and turbulent transport increase. As the flow is advected downstream, turbulent diffusion within the wakes becomes higher. In addition, the wake width, mean velocity deficit, and turbulence intensity levels all increase at each location in the wake region. Moreover, the airfoil surface roughness generally decreases the vortex shedding frequency due to thickened boundary layer.

### 1.4.4 Turbulent boundary layer

The flow regime in the boundary layer with unsteady mixing due to eddies of different scales is denoted as turbulent boundary layer. Since in this flow regime more mixing occurs in comparison to the laminar boundary layer, the gradient near the wall is greater. Consequently, an increase in shear stress at the wall, a fuller velocity profile and a greater boundary layer thickness are observed in comparison to the laminar boundary layer. The turbulent boundary layer velocity structure is divided in three main regions, Figure 1.16.

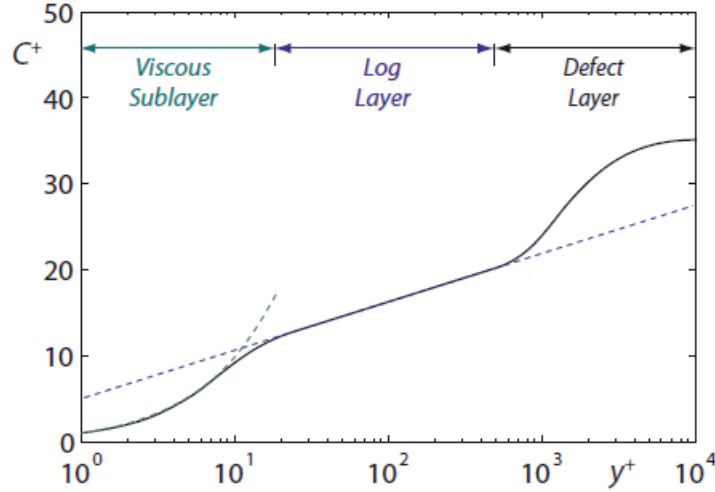


Figure 1.16: Turbulent boundary layer velocity profile structure, [79]

The dimensionless velocity  $C_x^+$  and distance  $y^+$  are defined:

$$C_x^+ = \frac{C_x}{C_{x\tau}}, \quad y^+ = \frac{C_{x\tau} y}{\nu} \quad (1.14)$$

where  $\tau_w$  is wall shear stress and  $C_{x\tau}$  is a friction velocity which is defined as:

$$C_{x\tau} = \sqrt{\frac{\tau_w}{\rho}} \quad (1.15)$$

The viscous sublayer region is a very thin region next to the wall. A linear relationship between the velocity and distance near the wall,  $y^+ < 5$ , is found, Equation 1.16.

$$C_x^+ = y^+ \quad (1.16)$$

The log-law layer is usually defined between  $y^+ > 30$  and  $y = 0.1\delta$ , [59]. The logarithmical relationship between  $C_x^+$  and  $y^+$  is defined as:

$$C_x^+ = \frac{1}{K} \ln y^+ + c \quad (1.17)$$

where  $K$  is the Kármán constant and  $c$  is a constant depending on surface roughness. Their values are  $K = 0.40$  to  $0.42$  and  $c = 5.0$  to  $5.2$  for smooth surface. The value of  $c$  for rough surface is presented as the following equation, [3].

$$c = 8.0 - \frac{1}{K} \ln k_s^+ \quad (1.18)$$

The region between the viscous sublayer,  $y^+ < 5$ , and the log-law region,  $y^+ > 30$ , is called the buffer layer, [59].

### 1.4.5 Boundary layer separation

Flow momentum is low inside the boundary layer due to a strong viscous effect. Consequently, the pressure gradient has an effect on the boundary layer flow. As the pressure gradient becomes positive at the point where the shear layer value reaches zero, the flow separate from the surface. Flow separation can be explained with a geometrical argument about the second derivative of velocity at the wall, [78]. The Prandtl's boundary layer equation is written as:

$$u \frac{\partial u}{\partial x} + v \frac{\partial u}{\partial y} = -\frac{1}{\rho} \frac{dP}{dx} + \nu \frac{\partial^2 u}{\partial y^2} \quad (1.19)$$

As  $u=v=0$  at the wall, it is obtained:

$$\frac{\partial \tau}{\partial y} = \mu \frac{\partial^2 u}{\partial y^2} = \frac{1}{\rho} \frac{dP}{dx} \quad (1.20)$$

or

$$\frac{\partial^2 u}{\partial y^2} = \frac{1}{\mu} \frac{dP}{dx} \quad (1.21)$$

In Figure 1.17, the effect of pressure gradient on boundary layer profile for different cases is illustrated. In a favorable gradient, Figure 1.17a, the profile is very rounded and no inflection point is observed. As a result, no separation is incepted.

In a zero pressure gradient the point of inflection is found at the wall, Figure 1.17b. As an adverse gradient begins, Figure 1.17c to Figure 1.17e, a point of inflection occurs in the boundary layer and its distance from the wall increase with the strength of the adverse gradient. However, the flow dose not separate for a weak gradient, Figure 1.17c. A critical condition is observed at a moderate gradient, Figure 1.17d where the wall shear is exactly zero,  $\tau_w = 0$ . This is defined as the separation point. Any stronger gradient will cause back flow at the wall, Figure 1.17e, with the boundary layer thickness increasing and the main flow separating.

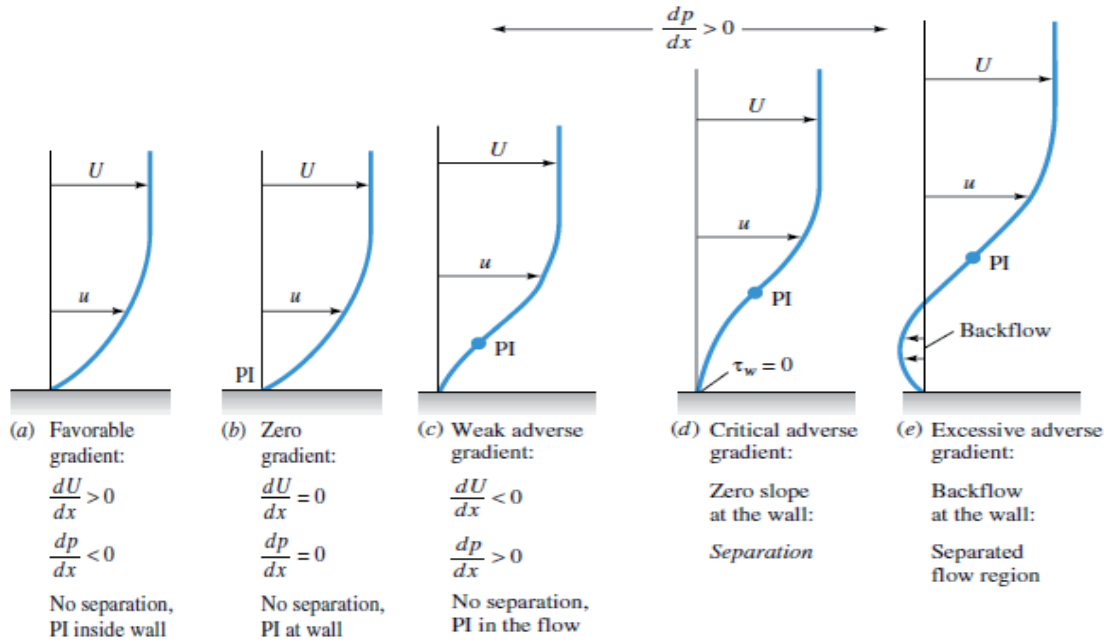


Figure 1.17: Effect of pressure gradient on boundary layer profile; PI= profile point of inflection, [78]

## 1.5 Purpose of the present work

Numerous works have attempted to reduce the vortex-induced vibration using different methods. However, not so many studies have been performed on a hydrofoil at high Reynolds number. According to several previous experiments, it is well known that the hydrofoil trailing edge geometry has a strong influence on the vortex-induced vibration amplitude. On the other hand, there exist a few studies investigating the effects of trailing edge geometry on the vortex shedding frequency, vortex-induced vibration, and wake dynamics. The oblique and Donaldson trailing edges are reported as two of the types that reduce the vortex-induced vibration in comparison to the blunt trailing edge. However the physics behind it is not fully understood. Therefore, the purpose of the present work is to investigate the effect of a hydrofoil trailing edge shape on the wake dynamic and its interaction with the mechanical structure to understand the phenomenon and the reasons for vibration reduction. This phenomenology could help optimize the trailing edge shape and obtain lower levels of vortex-induced vibration. Thus, hydrofoils with oblique and Donaldson trailing edges are tested in a high-speed cavitation tunnel at zero angle of attack and high Reynolds numbers,  $Re_L = 5 \cdot 10^5 - 3 \cdot 10^6$ . The truncated trailing edge hydrofoil is selected as reference. A velocity survey is performed via Laser Doppler Velocimetry, LDV, and Particle Image Velocimetry, PIV. Proper-Orthogonal-Decomposition, POD, is used to extract coherent structures from PIV data. In addition, flow induced vibration measurements and high-speed visualizations are performed. Finally, the effects of a tripped boundary layer transition on the wake are investigated and compared with the natural boundary layer transition.

## 1.6 Structure of the document

The document is organized in five parts: Part I presents the problem overview, fundamental aspects of the phenomenon and literature review. In Part II the case study and experimental setup are described. The results are discussed in Part III and IV, the corresponding final conclusions and perspectives are given in part V.

### **Part I: Introduction**

Chapter 1 deals with the fundamental aspects of vortex shedding, and boundary layer, followed by a corresponding literature review. Moreover, vortex formation mechanism, overview of wake regimes behind the cylinder and vortex-induced vibration are discussed. Different methods to control the wake are described, focusing on the trailing edge geometry modification. Moreover, laminar and turbulent boundary layer definitions and laminar-to-turbulent transition are explained. In addition, the problem overview and purpose of the present work are presented .

### **Part II: Case Study and Experimental Setup**

Chapter 2 explains the test facility and introduces the experimental hydrofoil. Measurement techniques such as Laser Doppler vibrometer, Laser Doppler Velocimetry, LDV, and Particle-Image-Velocimetry, PIV, are presented in chapter 3.

### **Part III and IV: Results**

Boundary layer development along the hydrofoil for two trailing edges and Reynolds effect on the boundary layer thickness is discussed in Chapter 4 and compared with blunt trailing edge. Effect of trailing edge shape on vortex-induced vibration is presented in Chapter 5. Chapter 6 concerns the trailing edge geometry effects on the wake flow. LDV phase-locked average and PIV using POD technique are performed under lock-in condition to survey the wake flow in the case of oblique trailing edge. Time-averaged velocity profiles are presented at different stream wise position along the wake for beveled and oblique trailing edges. Moreover, vortex shedding development along the wake is studied. Finally, effect of trailing edge shape on vortex formation mechanism is presented in Chapter 7. In Chapter 8 and 9 the effect of tripped laminar to turbulent boundary layer transition on vortex shedding process is presented.

### **Part V: Conclusions and Perspectives**

In the closing chapters, final conclusions are presented and recommendations are given for further work.



## Part II

# Case study and experimental setup



# Chapter 2

## Test facility and case study

### 2.1 High speed cavitation tunnel

The measurements are carried out in the EPFL high-speed cavitation tunnel, Avellan *et al.* [5], with a test section of 150 x 150 x 750 mm, maximum inlet velocity,  $C_{ref}$ , of 50 m/s, and maximum static pressure,  $p_{ref}$ , of 16 bar. The different sections of the high-speed cavitation tunnel are illustrated in Figure 2.1. A nozzle with reduction in area 46 to 1 is used to obtain a uniform velocity distribution in the test section. Before the nozzle a honeycomb is installed to avoid macroscopic flow rotation and reduce the turbulence level. A long diffuser, installed downstream of the test section, is used to recover the dynamic pressure by reducing the flow velocity to 3% of its value at the test section inlet. The bubble trap section collects bubbles in the flow. The bubbles tend to rise due to the buoyancy effect until they reach one of the plates and then are convected along the plate. The double suction pump provides a total head of 36.5 m for 1.125 m<sup>3</sup>/s at 885 rpm and it is directly driven by a 500 KW power DC-electric motor. A constant air pressure is kept over the free surface in the pressure vessel to control the pressure. In addition, a vacuum control system is installed to operate at low speed cavitation.

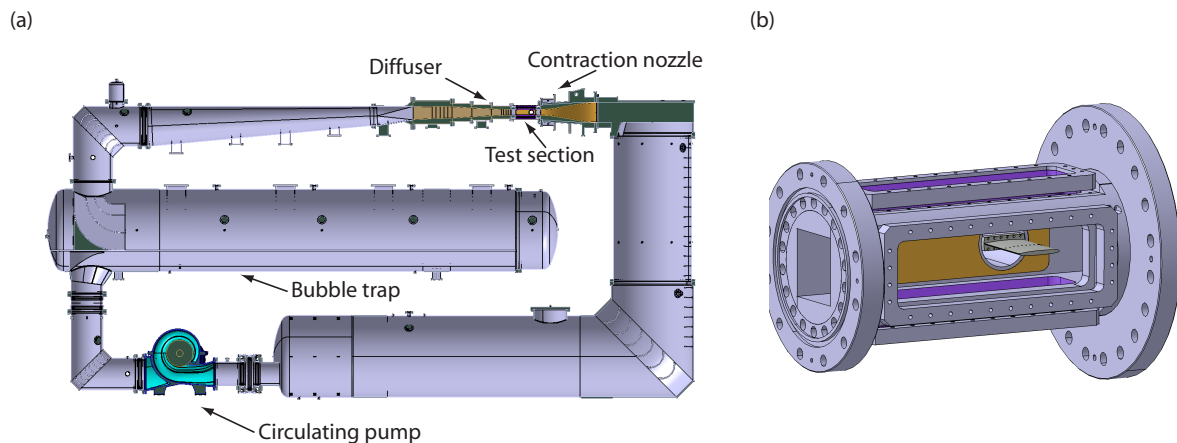


Figure 2.1: EPFL-LMH high speed cavitation tunnel: (a) Hydraulic circuit, (b) Test section

The absolute pressure measurements at both ends of the contraction nozzle and the temperature measurement define the flow condition at the inlet of the test section. The two high precision pressure transducers connected to pressure taps in the walls of each contraction nozzle end measure the absolute pressure.

Ausoni [3] measured the stream wise and transverse variation of mean velocities in span-wise and traverse directions at the inlet of the test section using Laser-Doppler velocimetry,  $Re_L = 2.0 \cdot 10^6$ , where  $L$  is the hydrofoil chord length. The mean normalized stream wise and transverse velocity fluctuation was found to be  $I_x = 0.96\%$  and  $I_y = 1.37\%$  respectively for traverse direction and  $I_x = 0.99\%$  and  $I_y = 1.34\%$  for span-wise direction. The mean normalized stream wise and transverse velocity fluctuation equations are defined as follow:

$$I_x = \frac{1}{N} \sum_{i=1}^N \frac{C_{x \text{ stdv } i}}{C_{ref}}, \quad I_y = \frac{1}{N} \sum_{i=1}^N \frac{C_{y \text{ stdv } i}}{C_{ref}} \quad (2.1)$$

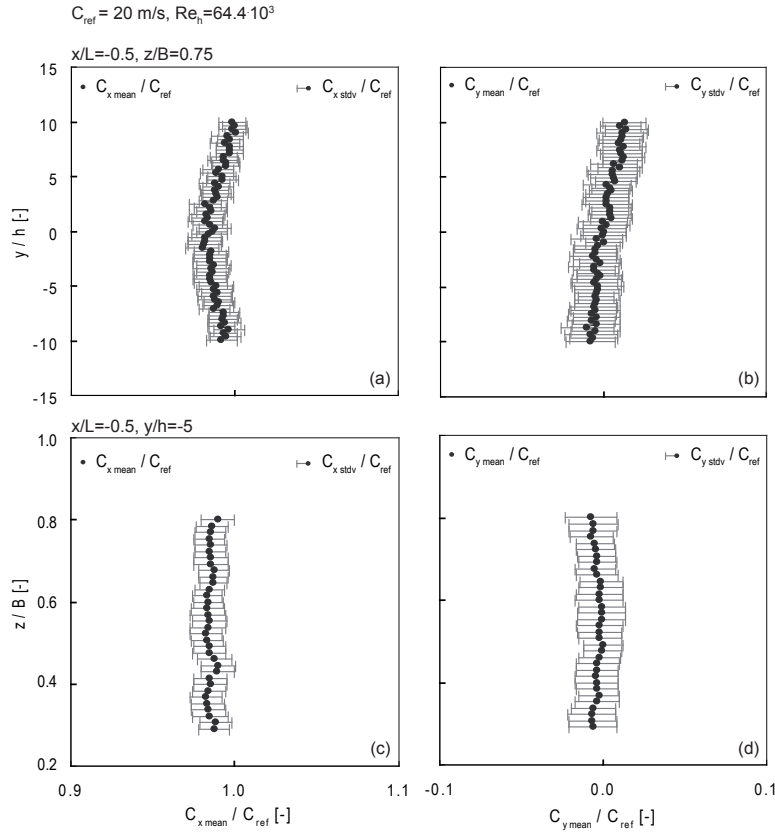


Figure 2.2: (a) Stream wise and (b) transverse mean velocity profiles and fluctuations at  $x/L = -0.5$  and  $z/b = 0.75$ . (c) Stream wise and (d) transverse mean velocity profiles and fluctuations at  $x/L = -0.5$ ,  $y/h = -5$ . Hydrofoil mounted in the test section,  $C_{ref} = 20 \text{ m/s}$ ,  $Re_h = 64.4 \cdot 10^3$ ,  $Re_L = 2.0 \cdot 10^6$ , [3]

## 2.2 Experimental hydrofoil

The tested hydrofoil in the present investigation is based on *NACA 0009 - 7.8 45/1.93* with the maximum thickness equal to 9% of the chord length. The hydrofoil is made of stainless steel with chord and span lengths of 110 mm and 150 mm respectively. *NACA 0009* blunt truncated at  $L = 100$  mm with trailing edge thickness of 3.22 mm is selected as a reference hydrofoil, Figure 2.3. The geometry is defined in a  $x; y; z$  coordinate system that its origin is placed at the hydrofoil leading edge.

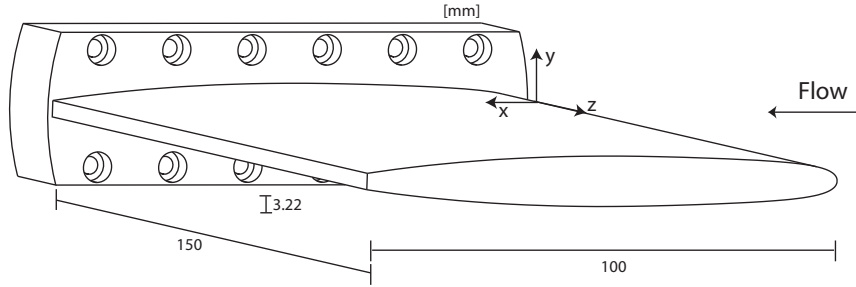


Figure 2.3: Blunt trailing edge *NACA 0009* hydrofoil

The foil thickness distribution is defined by the following equation, [3]:

$$\begin{aligned}
 0 \leq \frac{y}{L_0} \leq 0.5 \quad & \frac{y}{L_0} = a_0 \left( \frac{x}{L_0} \right)^{\frac{1}{2}} + a_1 \left( \frac{x}{L_0} \right) + a_2 \left( \frac{x}{L_0} \right)^2 + a_3 \left( \frac{x}{L_0} \right)^3 \\
 0.5 \leq \frac{y}{L_0} \leq 1 \quad & \frac{y}{L_0} = b_0 + b_1 \left( 1 - \frac{x}{L_0} \right) + b_2 \left( 1 - \frac{x}{L_0} \right)^2 + b_3 \left( 1 - \frac{x}{L_0} \right)^3
 \end{aligned}$$

with  $L_0$  being the original chord length and :

$$\begin{cases} a_0 = +0.1737 \\ a_1 = -0.2422 \\ a_2 = +0.3046 \\ a_3 = -0.2657 \end{cases} \quad \begin{cases} b_0 = +0.0004 \\ b_1 = +0.1737 \\ b_2 = -0.1898 \\ b_3 = +0.0387 \end{cases}$$

The first case study is an oblique trailing edge *NACA 0009* hydrofoil with the same geometry as the blunt hydrofoil except that the trailing edge is cut at about 93% of the chord length at an angle of  $30^\circ$ , Figure 2.4a. Its trailing edge thickness is quarter of blunt trailing edge thickness. The second case study is a Donaldson trailing edge hydrofoil, Figure 2.4b. This hydrofoil is shaped by modifying the blunt trailing edge with a combination of a straight line with an angle of  $45^\circ$  and a  $3^{rd}$  polynomial curve,  $y = a + b.x + c.x^2 + d.x^3$  where:

$$\begin{cases} a = -1.332 \\ b = 51.142 \\ c = -637.51 \\ d = 2595.18 \end{cases}$$

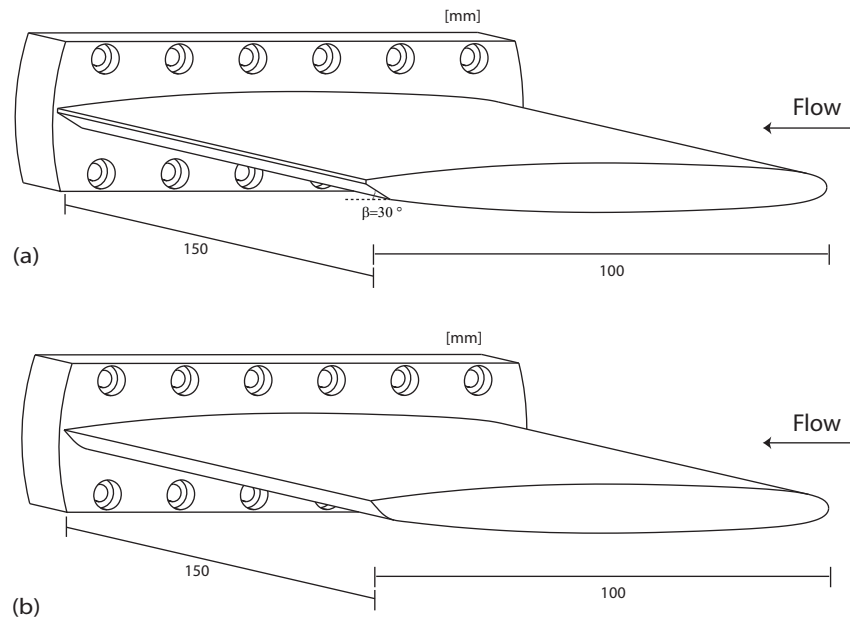


Figure 2.4: (a)Oblique and (b)Donaldson trailing edge *NACA 0009* hydrofoil

The three trailing edges are presented in Figure 2.5. First trailing edge corresponds to the truncated trailing edge, Figure 2.5a, the second one is the oblique trailing edge, Figure 2.5b, and the third one is the Donaldson trailing edge, Figure 2.5c.

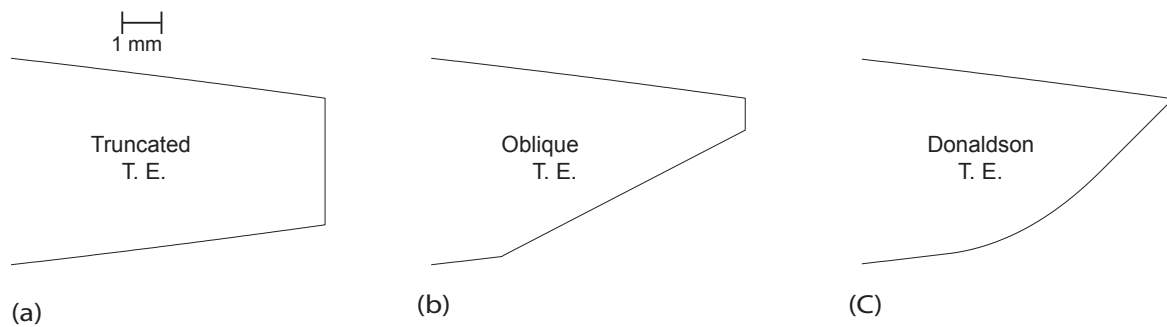


Figure 2.5: (a)Truncated (b)Oblique and (c)Donaldson trailing edge *NACA 0009* hydrofoil

The hydrofoil is mounted in the test section with tightly embedded one side and the other side is left free. Since the boundary layer development over the hydrofoil surface is of prime importance for the wake dynamics, special care is put on the similarity of the surface roughness between the tested hydrofoils to allow for a valid comparison.

The effect of Reynolds number on the drag and lift coefficients are presented in Figure 2.6 for  $\alpha=4^\circ$ . As the Reynolds number increases, the drag coefficient decreases for three trailing edge cases. The maximum drag coefficient is observed for oblique trailing edge. In case of the truncated trailing edge, the lift coefficients,  $C_z$ , rises slightly by increasing the Reynolds number contrary to the oblique and Donaldson trailing edges.

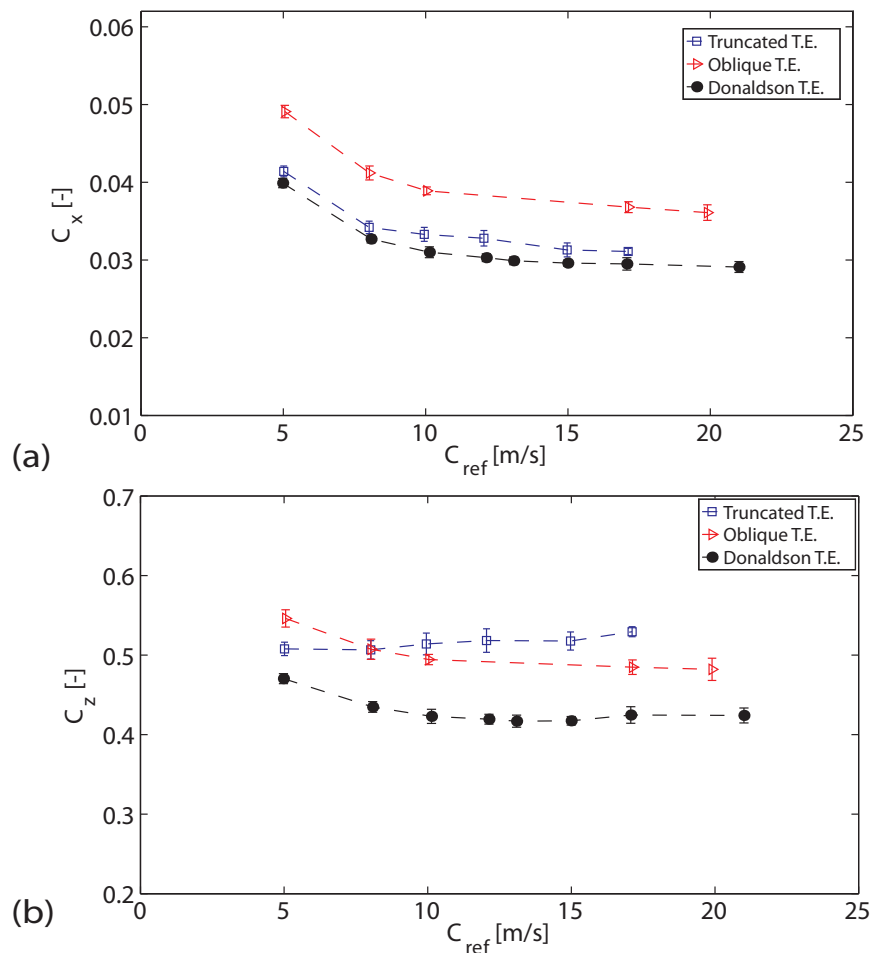


Figure 2.6: Effect of Reynolds number on (a) Drag, and (b) Lift coefficient of truncated, oblique, and Donaldson trailing edges,  $\alpha=4^\circ$ , rough case

The hydrodynamic performances in terms of lift and drag for three hydrofoils are presented in Figure 2.7 for  $Re_L = 1.1 \cdot 10^6$  in the case of fully turbulent boundary layer. As the incidence angle increases, the maximum drag coefficient corresponds to the oblique trailing edge. However, the minimum drag coefficient is found for Donaldson trailing edge. The lift coefficient decreases in the case of Donaldson trailing edge in comparison to two other trailing edges. In the case of negative incidence angle the drag and lift coefficients increase in comparison to the oblique and truncated trailing edges.

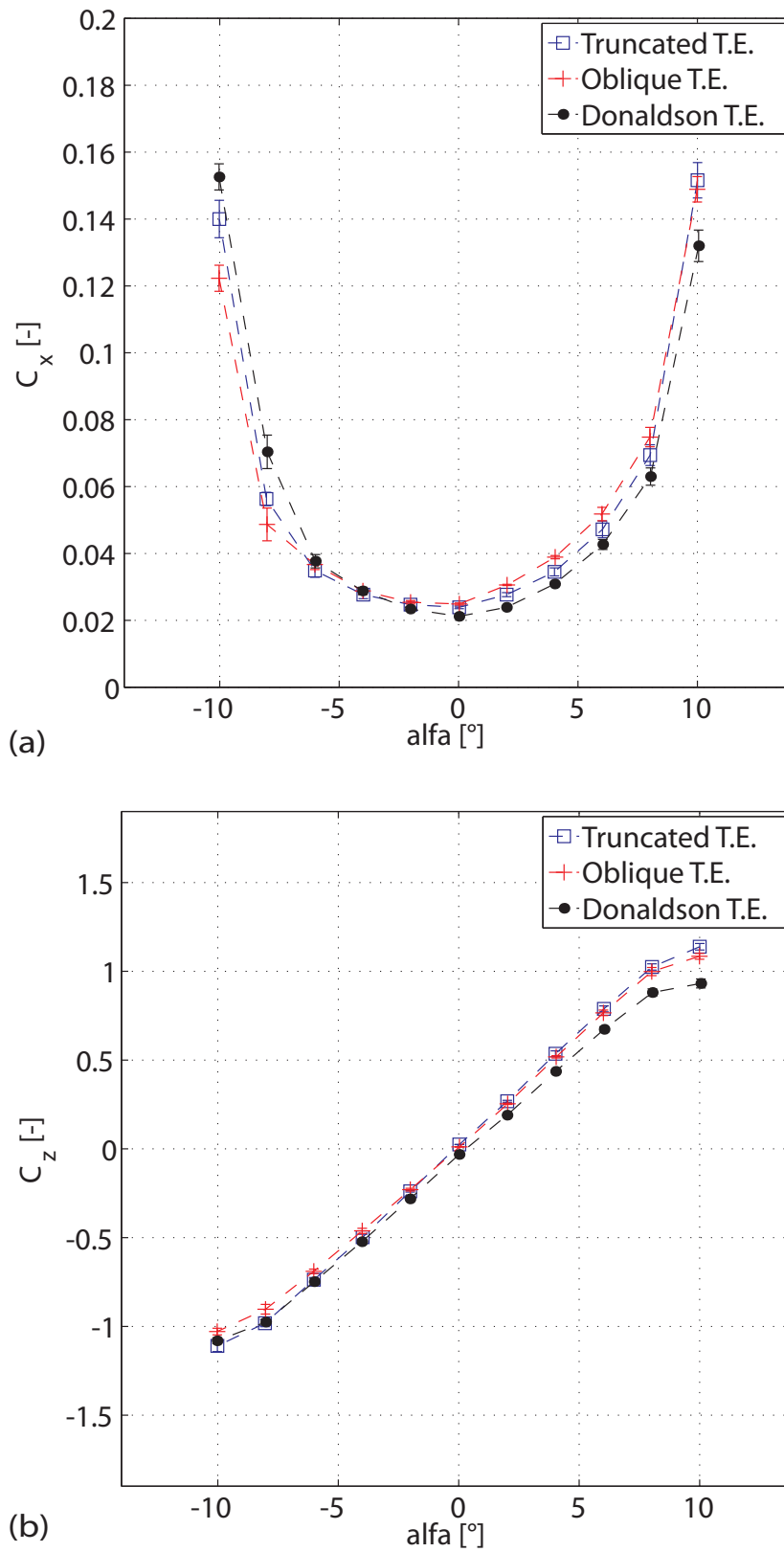


Figure 2.7: (a) Drag and (b) Lift coefficient of truncated, oblique, and Donaldson trailing edges,  $Re_L = 1.1 \cdot 10^6$ , rough case



### 2.2.1 Leading edge roughness

To investigate the wall roughness effects on the boundary layer and wake dynamics, a distributed roughness made of glue and 60  $\mu\text{m}$  diameter sand is placed on both sides of the hydrofoil, 4 mm downstream to the stagnation line and having a width of 4 mm wide. The glue and sand combination makes a two-dimensional flow obstacle of 150  $\mu\text{m}$  height.

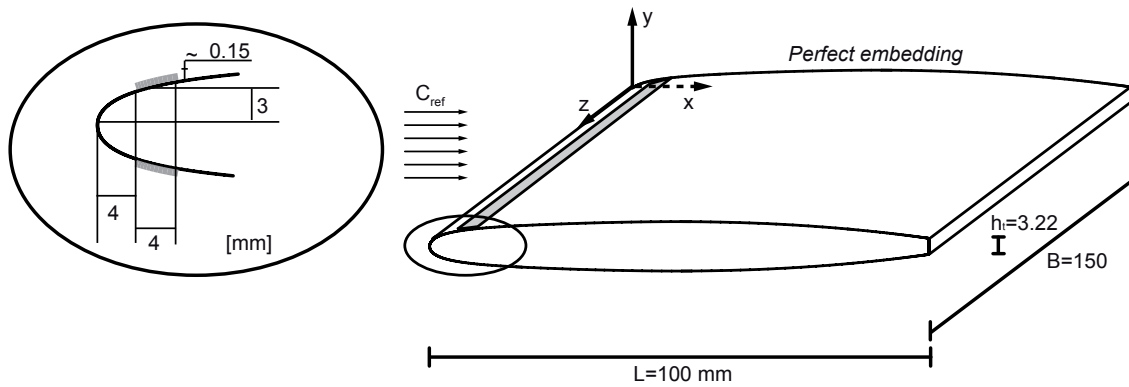


Figure 2.8: Blunt trailing edge *NACA 0009* hydrofoil and distributed roughness at the leading edge, Ausoni [3]



# Chapter 3

## Measurement techniques

### 3.1 Vortex-induced vibration measurement

#### 3.1.1 Accelerometer

*Kistler K-shear 8702B25* accelerometer is install to measure the vortex-induced vibration. The shear element design provides low transverse sensitivity along with insensitivity to base strain and thermal transients. The accelerometer is mounted on the hydrofoil support, Figure 3.1. The conditioning electronic is ensured by an external power supply coupler, *Kistler Power Supply/Coupler 5134A*.

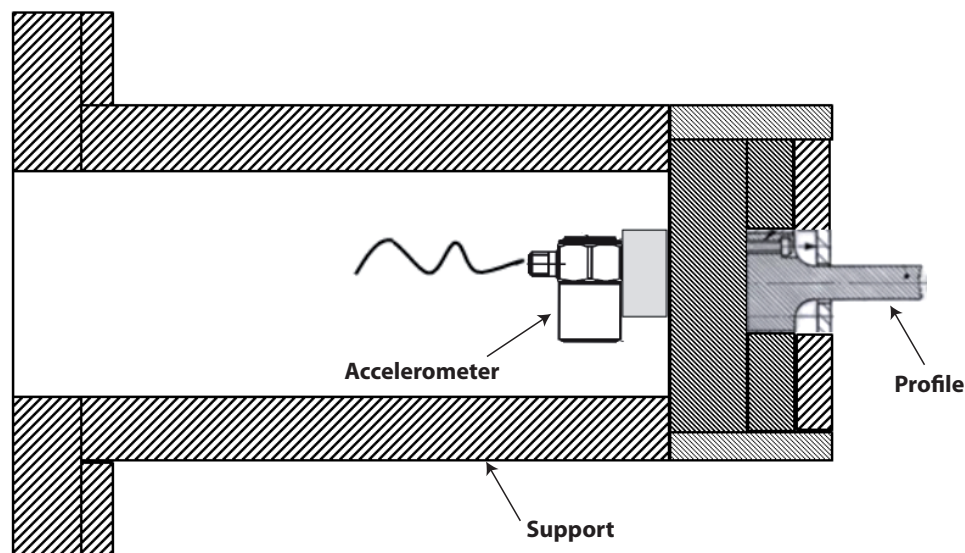


Figure 3.1: Accelerometer installed in the support of hydrofoil

Table 3.1 illustrates the main technical specifications of the accelerometer is illustrated.

Specification	
Acceleration range	$\pm 25$ g
Acceleration limit	$\pm 50$ gpk
Sensitivity	200 mv/g
Resonant frequency	54 kHz
Frequency response	8 kHz
Transverse sensitivity	1.5%

Table 3.1: Main technical data of the *Kistler K-shear 8702B25* accelerometer

### 3.1.2 Laser Doppler vibrometer

Laser Doppler vibrometer is a non-intrusive technique that directly measures the vibration of a test object using the Doppler effect. When laser light is beamed at a moving object, the frequency of the laser light reflected from the object,  $f_0 + f_D$ , differs from the original frequency of the emitted laser light,  $f_0$ , due to the Doppler effect, Figure 3.2.

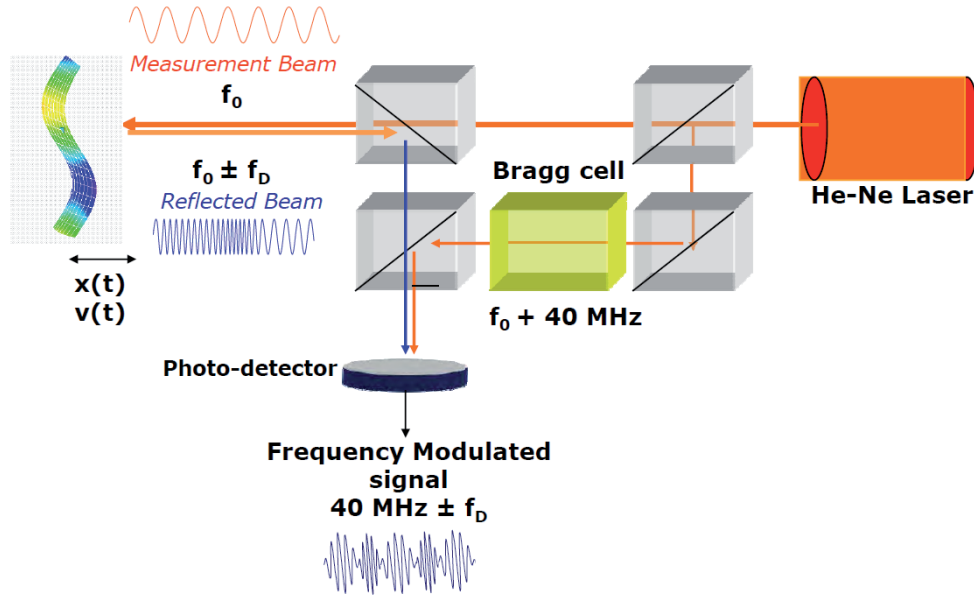


Figure 3.2: Laser interferometer

The relationship between the Doppler frequency  $f_D$ , velocity  $V$  and the laser wavelength,  $\lambda$ , is given as:

$$f_D = \frac{v_p}{\lambda} \quad (3.1)$$

Since the Doppler frequency has no sign and the direction of movement is unknown, a

fixed frequency offset using a Bragg cell in the interferometer allows to distinguish between positive and negative Doppler shifts, Figure 3.2.

In the present investigation, a *Polytec PDV100* laser Doppler vibrometer is used for vortex-induced vibration measurements. The measurement point is located at mid-span and 10 percent of the chord length, upstream from the trailing edge. The main general specifications of this vibrometer are presented in Table 3.2:

Specification	
Laser type and class	<i>HeNe</i> , class II
Velocity range	20, 100, 500 mm/s
Frequency range	0 – 22 kHz
Working distance	0.2 – 3 m
Dimension	300 (L)x63 (W)x129(H) mm

Table 3.2: Main technical data of the *Polytec PDV100* laser doppler vibrometer

### 3.1.3 Data acquisition system

*Hewlett-Packard* based on VXI (VMEbus Extensions for Instrumentation), is used for the data acquisition system. The main specification of this system is presented in Table 3.3. The data acquisition control and storage are performed using *NI-Labview* programming. In the present work the block size and measurement time of  $2^{20}$  Samples per channel and 20.48 second respectively are selected. For spectral computation, Fast Fourier Transform is applied to 16 equal segments of the time signal and averaging is performed.

Specification	
Converter resolution	16 bit
Maximum sampling frequency	51.2 KHz per channel
Memory depth	1 MSamples per channel

Table 3.3: Main specification of the VXI data acquisition system

## 3.2 Hydrodynamic load cell

A five components hydrodynamic load cell is used for Lift and drag static force measurements. A section through the load cell is presented in Figure 3.3, where the positions of the 5 strain gauges as well as the profile are visible. It allows a maximum of 104 N lift force measurement. The lift and drag force precision is 1.5 N and 0.5 N respectively.

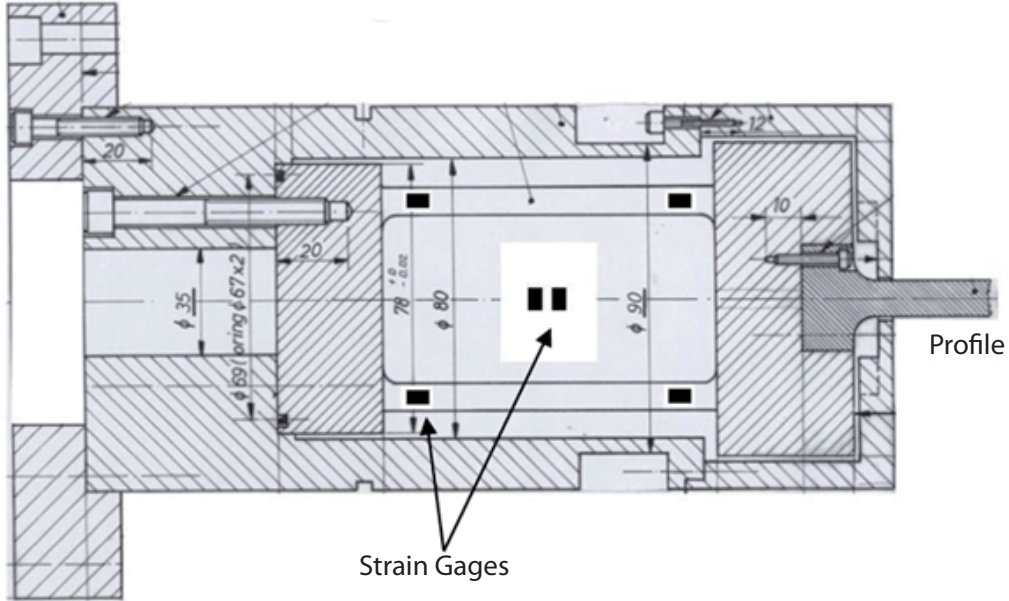


Figure 3.3: Load cell 504-3 (F+W Emmen)

### 3.3 Flow measurement

#### 3.3.1 Laser Doppler velocimetry

Laser Doppler velocimetry, LDV, is a non-intrusive technique for flow velocity survey using laser beams. An overview of laser Doppler techniques is given by Albrech [2]. Some advantages for LDV can be highlighted such as, no disturbance for the flow being measured; measurement possibility for unknown direction; and accurate measurement in a unsteady and turbulent flow. The basic principal of LDV measurement is illustrated in Figure 3.4.

The beams are generated from a 10 W Argon-Ion single laser source, Figure 3.4a, using a beam splitter. The beams are focused using a sending lens, Figure 3.4c. The direction of the beams is changed by the lens causing them to intersect at a certain focal point. A measurement volume, Figure 3.4d, is created where the beams are intersected. A set of equally spaced fringes, light and dark bands, is created by the interference of the light beams in the measurement volume. The distance between the fringes is calculated knowing wavelength of the laser light,  $\lambda$ , and the angle between the beams,  $\alpha$ , equation 3.2

$$\delta_{fringe} = \frac{\lambda}{2 \sin(\alpha/2)} \quad (3.2)$$

As the particles, with a density nearly the same as that of the water, pass through the measurement volume, the measurement is made. As a result, the light received by the particles fluctuates with a fringe. A relationship is found between the frequency of

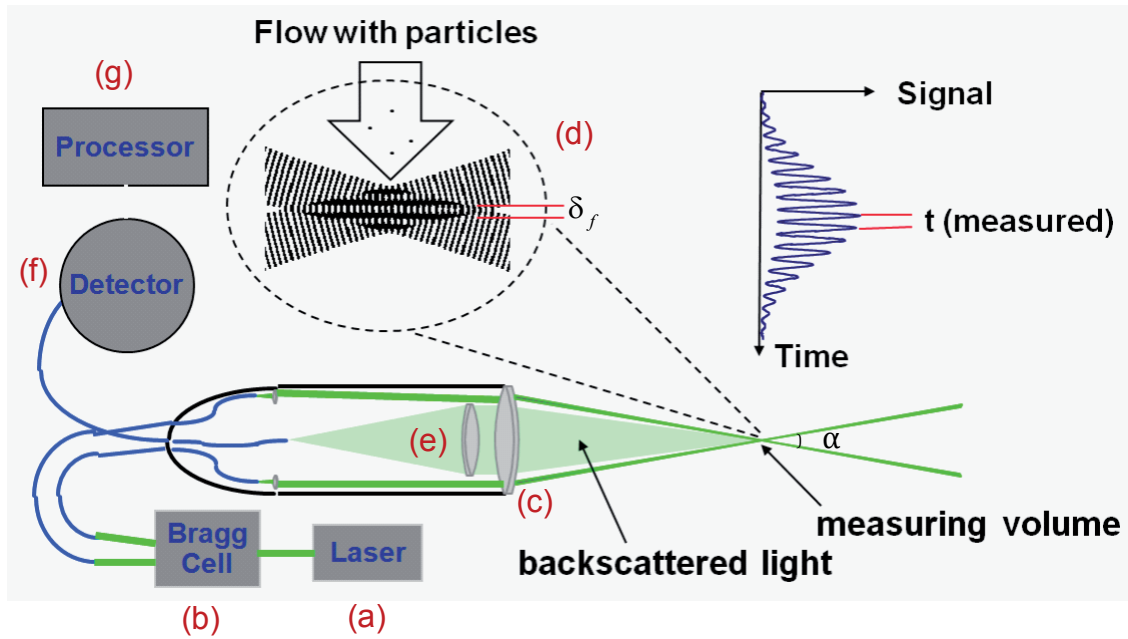


Figure 3.4: Principle measurement of Laser Doppler Velocimetry, (a)Laser source, (b)Bragg cell, (d)Measurement volume, (e)Receiving lens, (f)Photodetector, (g)Signal processing, (Courtesy of Dantec)

this fluctuation,  $f_{Doppler}$ , and the velocity of the particles normal to the fringes,  $C$ , as presented in equation 3.3

$$C = \delta_{fringe} \cdot f_{Doppler} = \frac{\lambda f_{Doppler}}{2 \sin(\alpha/2)} \quad (3.3)$$

The light scattered by the particle is collected by the receiving lens, Figure 3.4e, and focussed onto a photodetector, 3.4 f, which converts the light intensity fluctuations into voltage signal fluctuations. Finally, the frequency,  $f_{Doppler}$ , is detected in signal processing part, 3.4 g.

As it was explained above, LDV measures the frequency of the particle passing through a series of equally spaced fringes in the measurement volume. Two main limitations are known for this technique. A stationary particle produces no signal and two particles with the opposite direction and the same speed will give rise to indistinguishable signals. As a result, Bragg cell, 3.4 b, is used to split the laser beams by shifting the frequency of one of them by 40MHz. The Bragg cell contains a transparent medium, either liquid or solid, through which the laser beam passes. Passing the ultrasonic sound waves through it excites the medium and these sound waves diffract the laser beam with a frequency shift equal to the frequency of the sound wave.

As observed in Figure 3.5, without the Bragg cell the same frequency,  $f_{Doppler}$ , is found for negative velocity,  $C_B$ , and positive velocity,  $C_A$ . However, with the Bragg cell for positive velocity,  $C_A$ , the measured frequency is higher than the shift frequency and for negative velocity,  $C_B$ , the measured frequency lies below the shift frequency. In addition, a stationary particle in the measurement volume generates a signal with exactly the shift

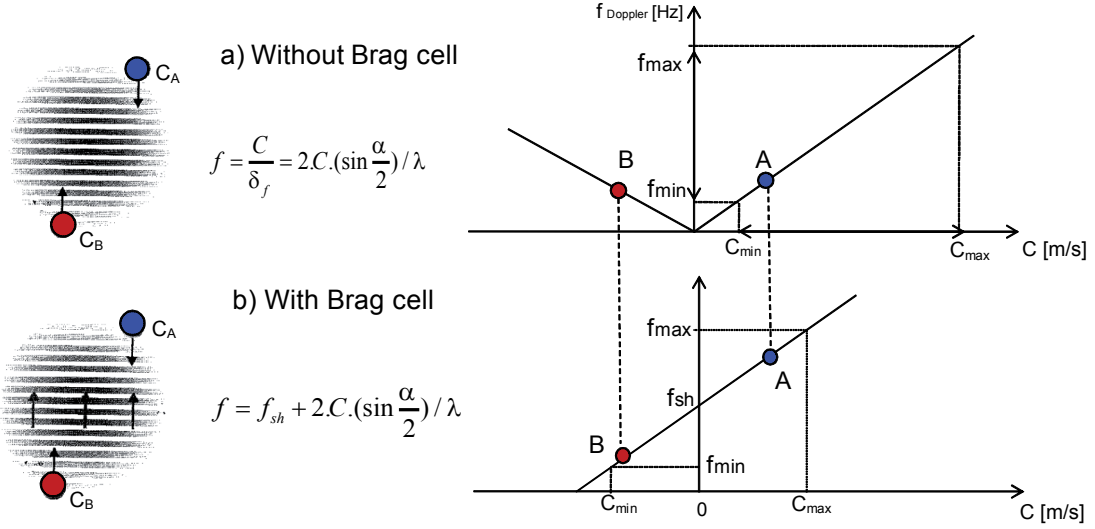


Figure 3.5: Removing directional ambiguity with frequency shifting, (a) Without Bragg cell, (b) With Bragg cell

frequency. Consequently, the negative velocities can be distinguished. Therefore, the directional ambiguity is removed, Durst [20].

The main source of error for the LDV measurements can be noted such as *particle averaging bias*.

### Particle averaging bias

When the flow velocity is high, more particles pass through the measurement volume in a given time as compared to low velocity. As a result, the mean flow velocity obtained from averaging the velocity samples shows a large value. Moreover, the estimated velocity variance will also be affected by an error. This is called particle averaging bias. The problem can be solved using the particle transit time  $t_i$  as a weighting factor, equation (3.6), [15], [36], [58] and [19]. The mean  $C_{x_{mean}}$  and fluctuating  $C_{x_{stdv}}$  stream wise velocities as well as the transit time weighting factor  $\eta_i$  are given as follow:

$$C_{x_{mean}} = \sum_{i=1}^N \eta_{x_i} C_{x_i} \quad (3.4)$$

$$C_{x_{stdv}} = \sqrt{\sum_{i=1}^N \eta_{x_i} (C_{x_i} - C_{x_{mean}})^2} \quad (3.5)$$

$$\eta_{x_i} = \frac{t_{x_i}}{\sum_{j=1}^N t_{x_j}} \quad (3.6)$$

The parameters of the LDV measurement are illustrated in Table 3.4



Parameters	
Laser type/class	Ion-Argon
Laser wave length (blue/green)	488 nm / 514.5 nm
Laser power	10 W
Optical system	2D-Laser probe
Signal transmission	Multi-mode fiber
Probe diameter	60 mm
Probe beam spacing	38.15 mm
Probe beam diameter	2.2 mm
Focal length in air	250 mm
Fringe spacing (green/blue)	3.38 $\mu\text{m}$ / 3.21 $\mu\text{m}$
Control volume size in water (minor axis/major axis), green	0.075 mm / 1.30 mm
Control volume size in water (minor axis/major axis), blue	0.071 mm / 1.24 mm
Bragg cell frequency	40 MHz
Particle type	Hollow glass spheres
Particle density	1100 kg/m <sup>3</sup>
Particle size	10 $\mu\text{m}$
Traverse resolution (linear/angular)	0.01 mm / 0.001°

Table 3.4: Properties of the LDV system

### Phase-locked average

Phase-locked average of the velocity field is performed to extract the deterministic and periodic component of the signal from the turbulent noise with a good signal to noise ratio. To this end, an accelerometer or a laser vibrometer is used as reference signal. Furthermore, a low pass filter was also applied to remove higher frequency components. A signal generator was then used to detect the passage of the vibration signal above a given threshold and generates a single pulse, i.e. reference signal, for LDV measurements. It is connected to the LDV processor synchronization input. The phase-locked average procedure is applied directly by sorting the samples into the corresponding phase based on the arrival time. The phase locked average of the velocity,  $\overline{C}$ , may be defined as follows:

$$\overline{C}(t) = \lim_{N \rightarrow \infty} \left( \frac{1}{N} \sum_{i=1}^N C(t + iT) \right) \quad 0 \leq t < T \quad (3.7)$$

Where  $t$  denotes the time and  $T$  is the period of vortex shedding. In the particular case of discrete and random LDV data, the vortex shedding period is divided into  $N_s$  segments. The data are then re-arranged using a new time variable  $t^*$  defined as  $t^* = t$  modulo  $T$ . The phase locked average of the velocity for a given segment,  $i$ , is computed over the velocity samples contained within the segment as follows:

$$\overline{C} \left( \frac{i}{N_s} T \right) = \frac{1}{\sum_{j=1}^N W_j \Pi_j^i} \sum_{j=1}^N C_j W_j \Pi_j^i \quad i = 0, \dots, N_s - 1 \quad (3.8)$$

Where  $W_j$  denotes the particle transit time (weighting factor) and  $C_j$  is the measured velocity.  $\Pi_j^i$  is a rectangular function equal to 1 inside the segment  $i$  and zero outside:

$$\Pi_j^i = \begin{cases} 1 & \text{if } \frac{i}{N_s}T \leq t_j^* < \frac{i+1}{N_s}T \\ 0 & \text{elsewhere} \end{cases} \quad (3.9)$$

### 3.3.2 Particle Image Velocimetry

Particle Image Velocimetry is a non-intrusive laser optical measurement technique to measure the velocity in the space. An overview of Particle Image Velocimetry is given in Raffel [60], Adrian [1]. The flow is illuminated in the target area with double pulsed light sheets. For each light pulse sheet, a separate image frame is captured by the camera,  $I_1$  and  $I_2$ , Figure 3.6. The images are divided into small subsections, called interrogation areas, IA. The interrogation areas from each image frame are cross-correlated with each other, pixel by pixel. The spatial cross-correlation function of the images interrogation areas  $I_1$  and  $I_2$  is defined by [10], equation 3.10.

$$C_{I_1 I_2}(\xi) = \lim_{S \rightarrow \infty} \frac{1}{S} \int_S I_1(\mathbf{x}) I_2(\mathbf{x} + \xi) dS(\mathbf{x}) \quad (3.10)$$

where  $dS(\mathbf{x}) = dxdy$ . The average particle displacement is identified by detecting the maximum correlation peak height in the calculated cross-correlation. The procedure is carried out for every interrogation area. Since the time between the two successive images is known, velocity in every interrogation area is evaluated. A velocity vector map over the entire target area is obtained after data processing.

The main properties of Particle Image Velocimetry in the present investigation is illustrated in Table 3.5. With the vertical laser sheet illuminating the hydrofoil trailing edge and the wake, the stream wise organization of the vortex street in the wake and the vortex generation mechanism at trailing edge are investigated.

Specification	
Lasers type/class	Q-switched Nd:YAG
Lasers wave length	532 nm
Lasers pulse duration	5 ns
Lasers pulse peak power	50 mJ
Maximum rate of laser pulse	10 Hz
Laser sheet thickness	1 mm
High sensitive camera resolution	12 bit
Picture size	1280x1024 pixels
Interrogation area size	32x32 pixels
Particle type	Hollow glass spheres
Particle density	1100 kg/m <sup>3</sup>
Particle size	10 $\mu$ m

Table 3.5: Properties of the PIV system

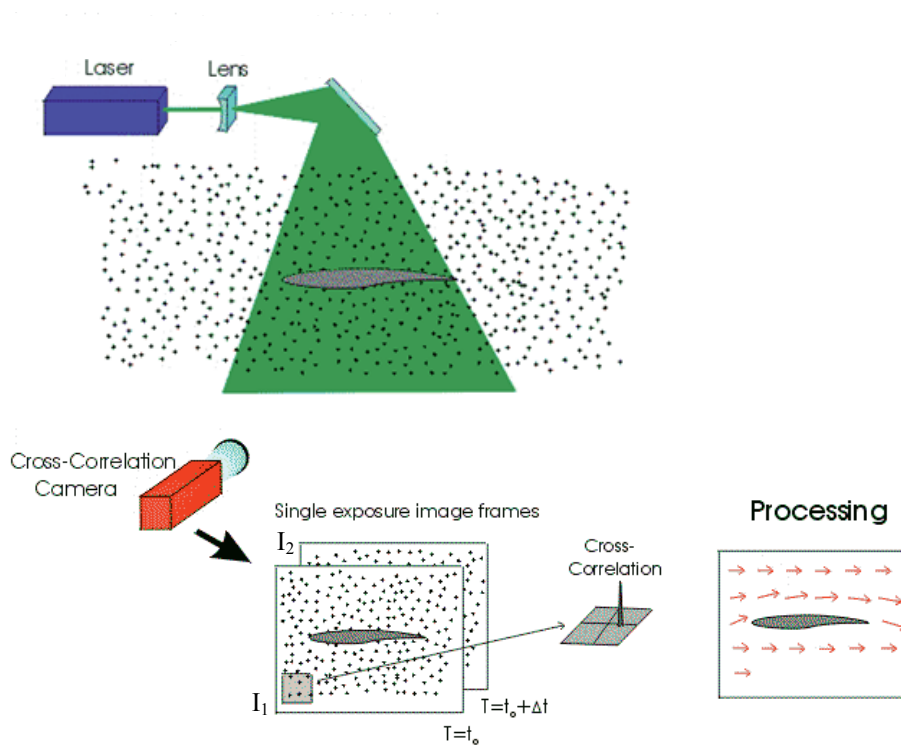


Figure 3.6: Principle measurement of Particle Image Velocimetry (PIV), (Courtesy of Dantec)

### Proper-Orthogonal-Decomposition

The Proper-Orthogonal-Decomposition, POD, is used as a post-processing technique to identify large coherent structures in the wake. For details refer to Sirovich[68] and Berkooz [12]. POD is particularly powerful in extracting the phase of the vortex shedding in an individual velocity field and filtering the low energetic part of the flow. It is based on a linear decomposition of velocity field with respect to orthogonal modes, equation 3.11

$$u^n = \sum_{i=1}^N a_i^n \cdot \phi^i \quad (3.11)$$

where  $u^n$  is a vector representing the velocity components in the entire measurement area and  $n$  is the sample index. Given a set of  $N$  velocity fields, snapshots,  $u^n$ , a correlation matrix  $C$  is defined as

$$C = U^T \cdot U \quad (3.12)$$

where  $U$  is a matrix composed of velocity components of  $N$  snapshots.  $N$  real positive eigen values,  $\lambda^i$ , each associated with an eigenvector,  $q^i$ , are obtained from the eigenvalue

problem, equation 3.13

$$C.q^i = \lambda^i.q^i \quad (3.13)$$

The normalized POD modes,  $\phi^i$ , are obtained from equation 3.14

$$\phi^i = \frac{\sum_{n=1}^N q_i^n \cdot u^n}{\|\sum_{n=1}^N q_i^n \cdot u^n\|} \quad (3.14)$$

The POD coefficient,  $a^n$ , in equation 3.11 presents the projection of the velocity field onto the POD eigenmode.

$$a_i^n = (u^n, \phi^i) \quad (3.15)$$

Exact reconstruction of the velocity field, equation 3.11, is obtained through a linear combination of  $N$  modes. The decomposition of the flow by POD provides a set of modes that represent flow structure containing most of the energy. The first ten modes of the present investigation are presented in Figure 3.7. The first mode, mode zero, represents the mean flow. The phase of an individual flow field is determined from its projection on the first pair of POD modes, allowing phase averaging of the measurement data to be performed. The vortex shedding investigation using POD technique is presented in the works of Oudheusden [55], Ma [50], Graftieaux [28] and Vonlanthen[77].

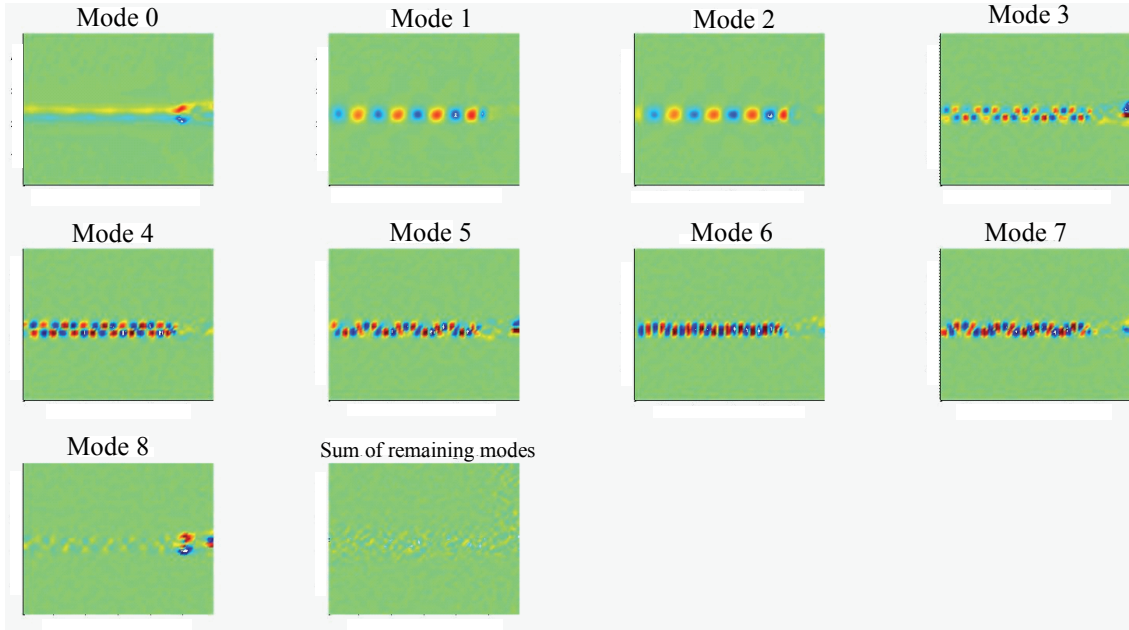


Figure 3.7: Example of Proper-Orthogonal-Decomposition modes, Truncated trailing edge,  $C_{ref} = 12m/s$

In the present specific case study, the POD method offers an interesting way of performing phase averaging of the velocity fluctuation even if the sampling frequency is far below the vortex shedding frequency. It saves the use of an external trigger, which is usually adopted in similar case studies.

### 3.4 Flow visualization

A high-speed camera, *Photron ultima APX*, having an image full resolution of 1024x1024 pixels at up to 120'000 fps is used to analyze the wake structure. Typically, the CCD image resolution is set to 512x256 pixels at 10000 fps. The properties of the high-speed image acquisition and lighting systems are given in Table 3.6

Specification	
High speed camera shutter speed	4 – 1670 $\mu s$
High speed camera frame rate	1 – $12 \cdot 10^3$ fps
High speed camera max CCD resolution	1024x1024 pixels (up to $2 \cdot 10^3$ fps)
High speed camera buffer memory	8 GB
Flash lamps electric energy	1875 J
Flash lamps max pulse duration	11 ms
Lamps power	1000 W

Table 3.6: Properties of the high-speed image acquisition and lighting systems



# Part III

## Results and Analysis





# Chapter 4

## Effect of trailing edge shape on boundary layer

As the vortex street is related directly to the state of boundary layer along the hydrofoil, in this chapter the effects of the trailing edge shape on the boundary layer are investigated. The development of the boundary layer velocity profiles along the Donaldson trailing edge hydrofoil chord is presented under lock-off condition,  $Re_L = 2.10^6$ . The results are compared with the boundary layer measurement of the truncated trailing edge under same condition, Ausoni [3]. Since the Donaldson trailing edge is non-symmetric, the boundary layer velocity profiles measurement is performed on the suction and pressure sides of the hydrofoil. In addition, the effects of the Donaldson trailing edge on laminar-to-turbulent transition on both sides of the hydrofoil are studied.

### 4.1 Development along the hydrofoil chord

Time-averaged boundary layer velocity profiles at 20, 40, 60, 70, 80 and 90% of the chord length are presented in Figure 4.1 on the suction and pressure sides of the Donaldson trailing edge hydrofoil. The streamwise mean velocity,  $C_{xmean}$ , is normalized by the free-stream velocity,  $C_{ref}$ . The comparison between the boundary layer velocity profiles on the suction and pressure sides of Donaldson trailing edge reveals a thicker boundary layer on the pressure side. In addition, a fully turbulent boundary layer velocity profile is observed between 60% and 70% of the chord length for pressure side and between 70% and 80% of the chord length on the suction side. This is an indication that the laminar-to-turbulent transition occurs earlier on the hydrofoil pressure side. Moreover, the velocity outside the boundary layer is higher on the pressure side than the suction side. Comparing the boundary layer velocity profiles between the suction side of truncated and Donaldson trailing edges reveals a thicker boundary layer in the case of the Donaldson trailing edge, Figure 4.2. In addition, the laminar-to-turbulent transition is observed between 70% and 80% of the chord length for Donaldson case and between 80% and 90% of the chord length for truncated case. According to the work of Ausoni [3], the laminar-to-turbulent transition is observed at 85% of the chord length for truncated trailing edge.

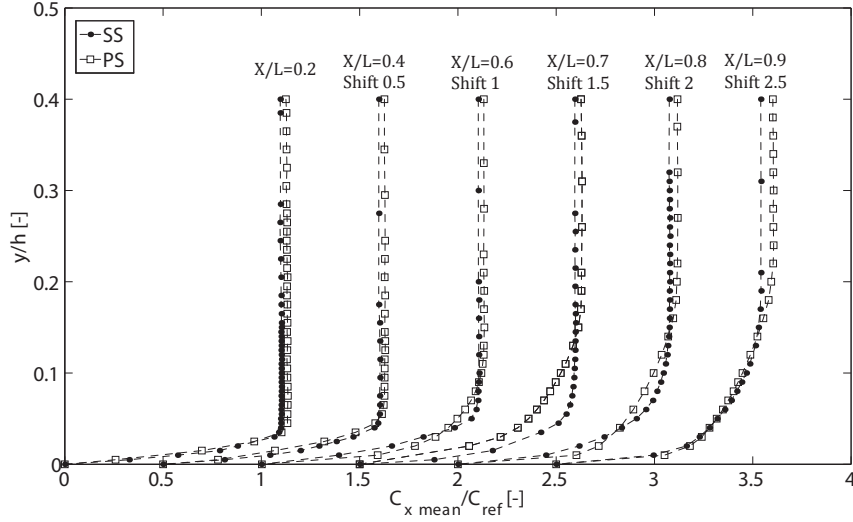


Figure 4.1: Time-averaged boundary layer velocity profiles along the hydrofoil chord on the suction and pressure sides of the Donaldson trailing edge,  $C_{ref} = 20$  m/s,  $i = 0^\circ$ , cavitation free

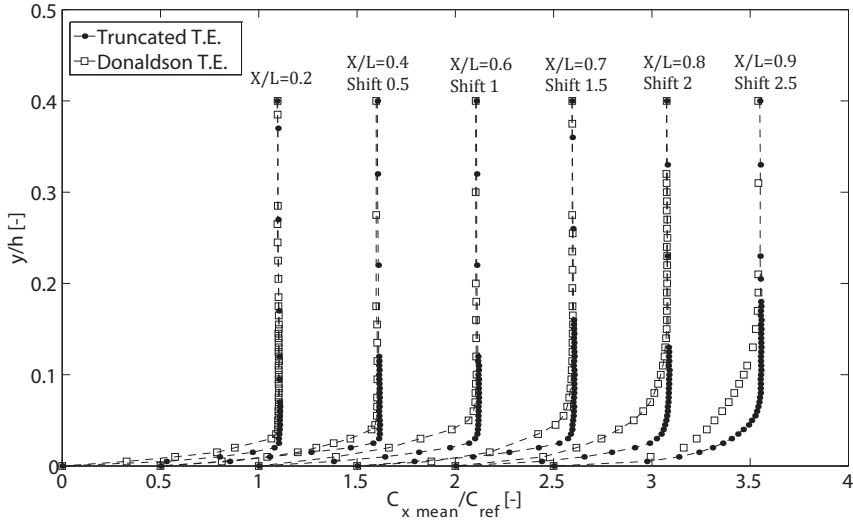


Figure 4.2: Time-averaged boundary layer velocity profiles along the hydrofoil chord on the suction side of the truncated and Donaldson trailing edges,  $C_{ref} = 20$  m/s,  $i = 0^\circ$ , cavitation free

Figure 4.3 shows the normalized velocity fluctuation inside the boundary layer at 60, 70, 80 and 90% of the chord length for the truncated and Donaldson trailing edges,  $Re_L = 2.10^6$ . Higher velocity fluctuation is observed for Donaldson trailing edge in comparison to the truncated trailing edge.

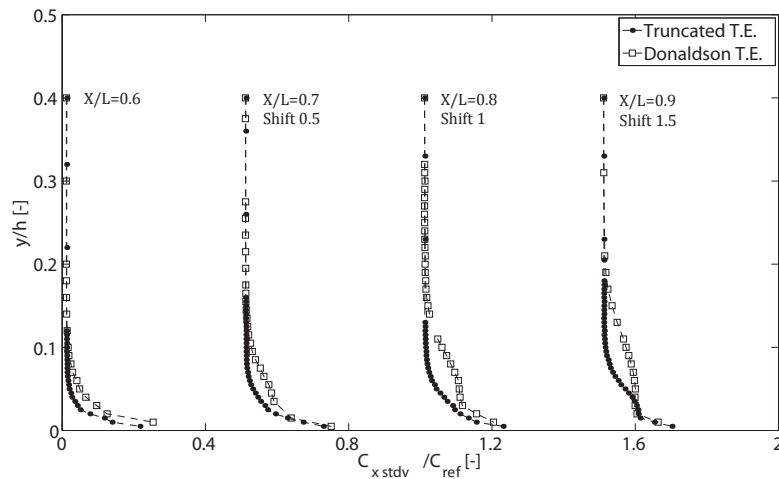


Figure 4.3: Normalized velocity fluctuation profiles along the hydrofoil chord on the suction side of the truncated and Donaldson trailing edges,  $C_{ref} = 20$  m/s,  $i = 0^\circ$ , cavitation free

#### 4.1.1 Boundary layer thickness

Normalized boundary layer thickness along the hydrofoil chord is presented in Figure 4.4 for the suction side of the truncated trailing edge and the suction and pressure sides of Donaldson trailing edge. The significant increase in boundary layer thickness along the hydrofoil chord corresponds to the laminar-to-turbulent transition location. In addition, in the case of the Donaldson trailing edge, the laminar-to-turbulent transition location moves towards the hydrofoil leading edge.

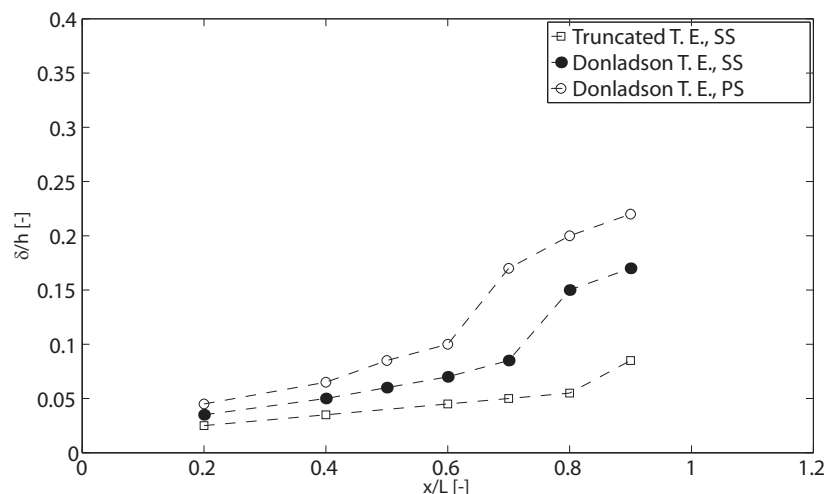


Figure 4.4: Boundary layer thickness evolution along the hydrofoil chord on suction side of truncated trailing edge and suction and pressure sides of Donaldson trailing edge,  $C_{ref} = 20$  m/s

### 4.1.2 Boundary layer structure

The boundary layer structure are characterized using  $y^+$  and  $C_{xmean}^+$ , defined in section 1.4.1. The viscous sublayer can not be correctly measured due to the size of the LDV measurement volume with respect to the boundary layer thickness. For the estimation of the wall shear stress and the friction velocity, the skin friction coefficient  $c_f$  of the laminar and turbulent flat plate boundary layers is used, [3]. The boundary layer structure at different positions along the chord length under lock-off condition,  $Re_L = 2 \cdot 10^6$ , is illustrated in Figure 4.5 and Figure 4.6 for the suction and pressure sides of the Donaldson trailing edge respectively. The velocity profiles are shifted on the vertical axis according to their position on the hydrofoil chord, for clarity. The theoretical log law slope is plotted as well for comparison. The log region is observed between  $x/L = 0.8$  and  $x/L = 0.9$  for the suction side, Figure 4.5 and between  $x/L = 0.7$  and  $x/L = 0.9$  for the pressure side, Figure 4.6. A significant change in boundary layer structure is revealed at the laminar-to-turbulent transition locations.

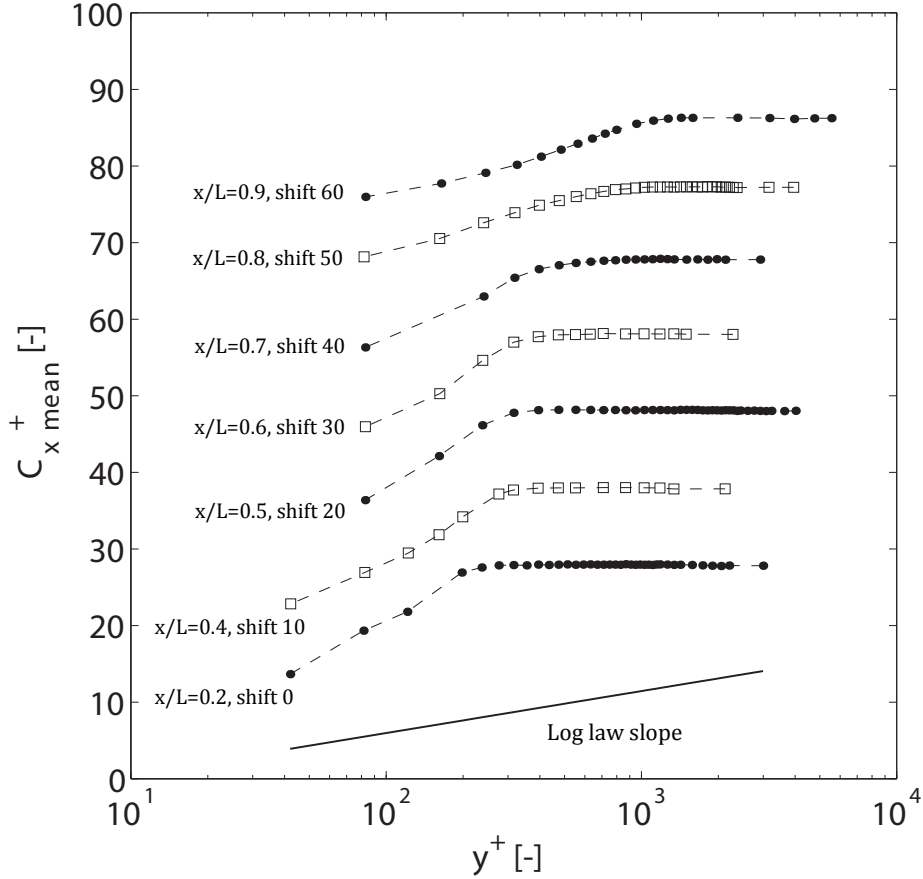


Figure 4.5: Time-average boundary layer structure along the hydrofoil chord on suction side of the Donaldson trailing edge,  $C_{ref} = 20$  m/s

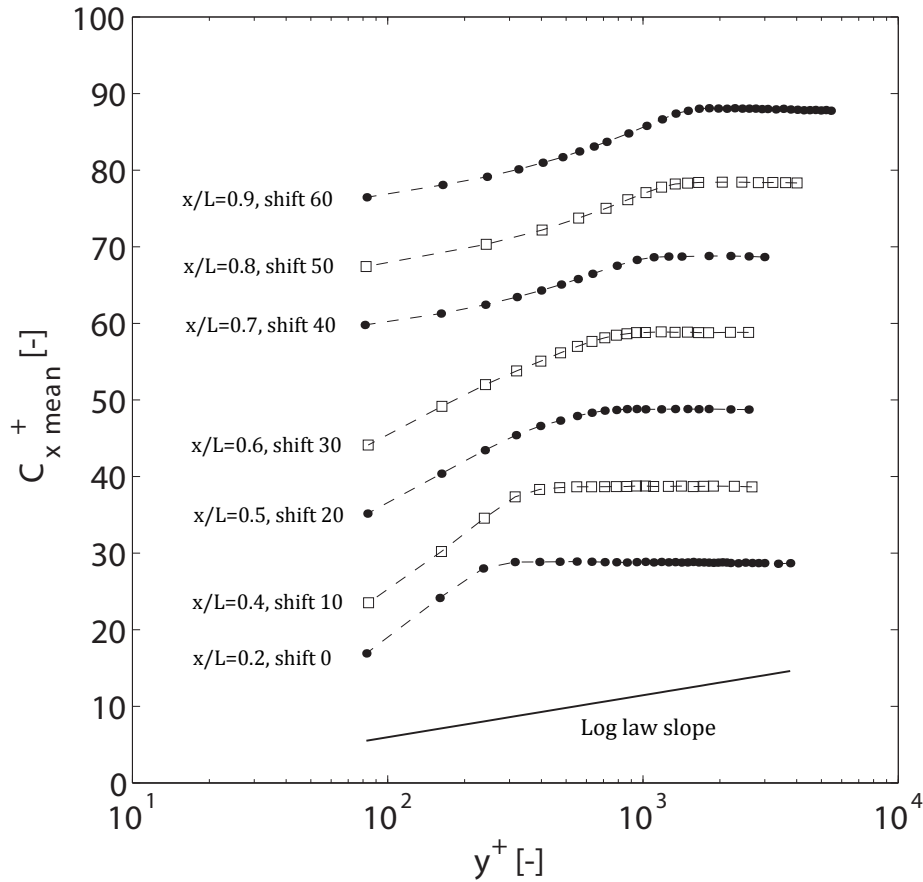


Figure 4.6: Time-average boundary layer structure comparison along the hydrofoil chord on pressure side of Donaldson trailing edge,  $C_{ref} = 20$  m/s

## 4.2 Development at trailing edge

### 4.2.1 Reynolds effects on the velocity profile thickness at trailing edge

The Reynolds number effects on the velocity profile are investigated on the pressure side of the Donaldson trailing edge,  $x/L = 0.99$ . A reverse flow, negative mean velocity, is observed close to the wall for the entire range of Reynolds number as observed in Figure 4.7a for  $Re_L = 1.5 \cdot 10^6$  and  $Re_L = 2.6 \cdot 10^6$ . This shows that the boundary layer has already separated from the hydrofoil and a vortex has been formed on the pressure side of Donaldson trailing edge. This goes in contrast with the truncated trailing edge where the separation point is fixed at the truncated part of the trailing edge for the suction and pressure sides. The velocity profile thickness at trailing edge,  $x/L = 0.99$ , for different Reynolds number is presented in Figure 4.7b. It passes through a minimum at  $Re_L = 1.5 \cdot 10^6$ . A linear relationship between the velocity profile thickness at trailing edge and Reynolds number is not observed for the pressure side of Donaldson trailing edge. This is due to the boundary layer separation and laminar-to-turbulent transition

locations being free to shift on the pressure side of the Donaldson trailing edge. As the Reynolds number increases the transition point moves towards the leading edge and the separation point shifts towards the trailing edge. The former increases and the latter decreases the velocity profile thickness at the trailing edge. As result, the non-linear relationship between the velocity profile thickness at the trailing edge and the velocity is due to the effect of Reynolds number on separation and transition point. However, in the case of truncated trailing edge when the Reynolds number increases the separation point is fixed at the trailing edge and the transition moves towards the leading edge. As a result, a linear relationship is found between the boundary layer thickness at trailing edge and the velocity, Ausoni [3].

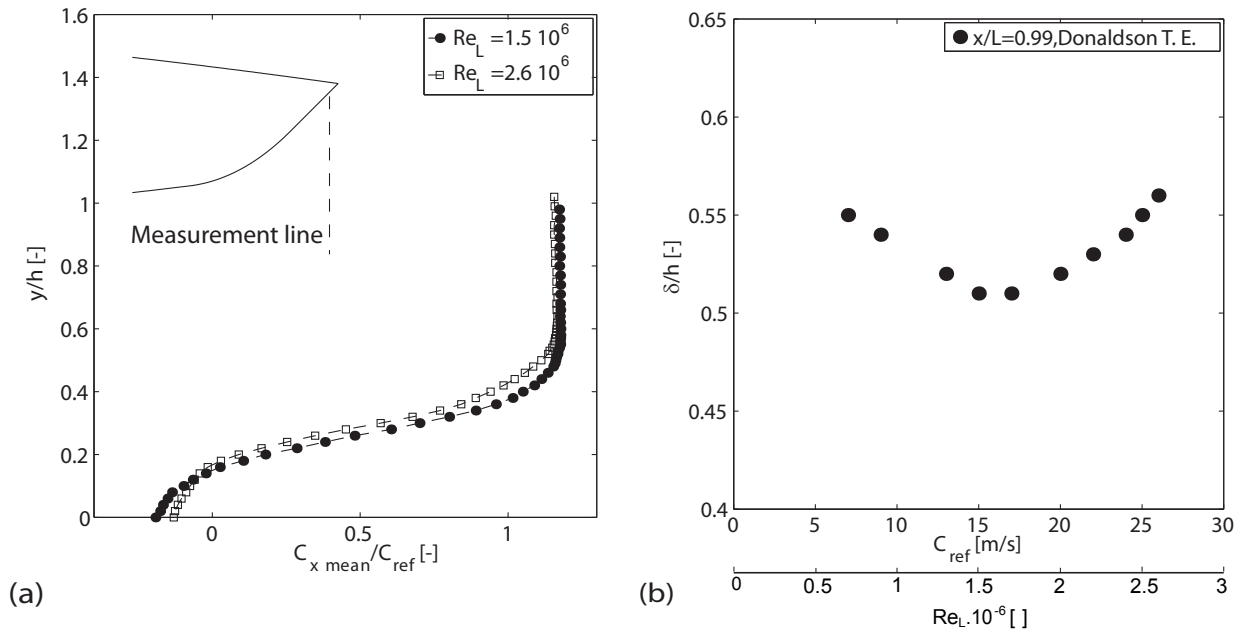


Figure 4.7: (a) Normalized time-averaged velocity profiles at  $x/L = 0.99$  for  $C_{ref} = 15$  m/s and  $C_{ref} = 26$  m/s, (b) Velocity profile thickness versus Reynolds number at  $x/L = 0.99$  on the pressure side of Donaldson trailing edge

According to the presented results, it is concluded that the trailing edge shape has a direct influence on the entire boundary layer structure along the hydrofoil chord and laminar-to-turbulent transition position.

# Chapter 5

## Effect of trailing edge shape on vortex-induced vibration

In this chapter, the effects of the hydrofoil trailing edge geometry on the vortex-induced vibration are studied. The results are described in terms of vibration amplitude, vortex shedding frequency, and Strouhal number in the case of truncated, oblique and Donaldson trailing edges. In addition, the role of boundary layer thickness at hydrofoil trailing edge to obtain a constant Strouhal number is studied.

### 5.1 Vibration amplitude

Vortex-induced vibration is monitored on the hydrofoil surface with a Laser vibrometer. The measurement point is located at mid-span and 10 percent of chord length, upstream from the trailing edge. The selection criteria for the vibration measurement point is noted to avoid vibration nodes for first and second mode shapes, bending and torsion, and have large enough vibration level to be measured correctly. Obviously, the measurement point is kept the same for both hydrofoils to allow for fair comparison. Waterfall spectra and amplitude of the vibration signal for different velocity of flow in the case of truncated, oblique, and Donaldson trailing edges is illustrate in Figure 5.1 and Figure 5.2. Fast Fourier Transform is applied to 16 segments of the time signal and the averaging is performed. The sampling frequency is 51.2 kHz and the block size is around 1M Samples. A significant increase in vibration amplitude versus flow velocity is found under lock-in condition where the vortex shedding frequency approaches the hydrofoil's natural frequencies,  $f = 890$  Hz, corresponding to the torsional mode. Lock-in is observed for Reynolds number ranging from,  $1.2 \cdot 10^6$  to  $1.4 \cdot 10^6$  and  $1.3 \cdot 10^6$  to  $1.5 \cdot 10^6$  for truncated and oblique trailing edges respectively. However, lock-in condition is not found in the case of Donaldson trailing edge. An increase of vibration is observed only for  $Re_L = 1.1 \cdot 10^6$  for Donaldson trailing edge. Comparing three trailing edges, maximum vibration amplitude under lock-in and lock-off conditions,  $Re_L = 1.2 \cdot 10^6$  to  $Re_L = 2.7 \cdot 10^6$ , corresponds to the truncated trailing edge and the minimum vibration amplitude is found for Donaldson trailing edge. These results are in agreement with the former studies which report that the oblique and Donaldson trailing edges decrease the vibration amplitude in comparison to the truncated trailing edge, [17], [37] and [13].

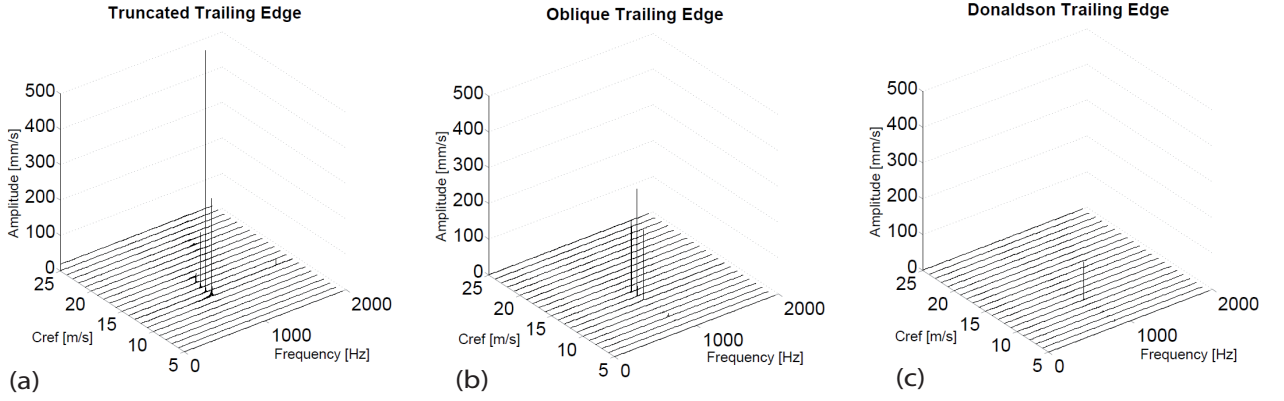


Figure 5.1: Waterfall spectra of the vortex-induced vibration for different flow velocities,  $x/L=0.9, z/B=0.75$ , (a)Truncated, (b)Oblique, and (c)Donaldson trailing edge

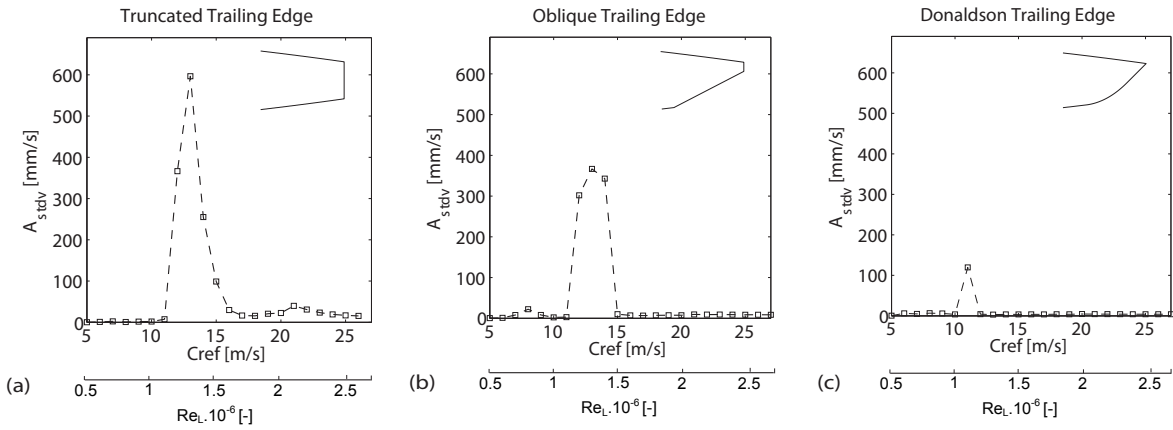


Figure 5.2: Standard deviation of the vibration signal versus Reynolds number, (a)Truncated, (b)Oblique, and (c)Donaldson trailing edge

An increase in vibration amplitude is observed at velocity around  $7 \sim 8$  m/s where the vortex shedding frequency approaches half of the hydrofoil's natural frequencies,  $f = 445$  Hz, Figure 5.2. The spectral analysis is performed on the LDV raw data samples measured in the wake of truncated and oblique trailing edge hydrofoil at  $x/L = 1.02$  and  $y/L = 0.04$ , Figure 5.3. The power spectral density is estimated from the raw data samples using FFT-techniques which require samples that are equally spaced in time. As result, the resampling of the raw data is performed before the FFT-analysis. The Data are divided in consecutive segments and Fast Fourier Transform is applied to segments and averaging is performed. In fact, when the flow velocity is around  $7 \sim 8$  m/s, the shedding frequency corresponds to half of the structural eigen frequency. In this case, the oblique trailing edge hydrofoil exhibits more vibration than the truncated one. We believe that this peculiar result is due to the non-symmetric trailing edge, which produces stronger harmonics and thereby more excitation at resonance frequency.



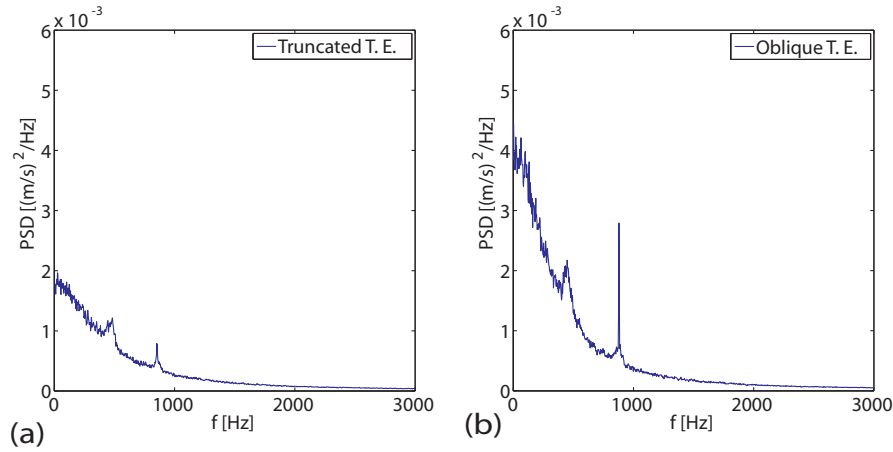


Figure 5.3: Power spectrum density of transverse velocity component, (a) truncated,  $C_{ref} = 7$  m/s, and (b) Oblique  $C_{ref} = 8$  m/s, trailing edge at  $x/L=1.02$ ,  $y/L=0.04$

## 5.2 Vortex shedding frequency and Strouhal number

LDV measurement is performed on a point in the wake to find the vortex shedding frequency using the spectral analysis on the LDV data. Two examples of the power spectrum density is presented in Figure 5.4 under lock-in,  $C_{ref} = 13$  m/s, and lock-off,  $C_{ref} = 23$  m/s, conditions in the case of oblique trailing edge.

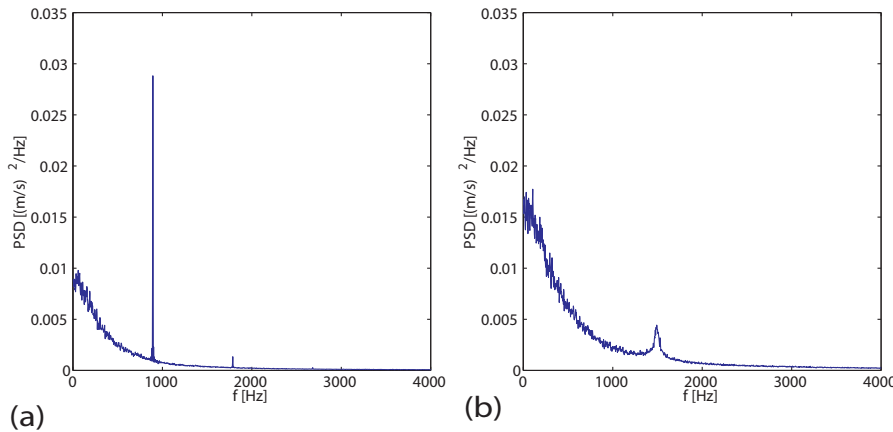


Figure 5.4: Power spectrum density, (a) lock-in,  $C_{ref} = 13$  m/s, and (b) lock-off,  $C_{ref} = 23$  m/s, oblique trailing edge,  $x/L=1.05$ ,  $y/L=0.15$

Vortex shedding frequency is plotted for truncated, oblique and Donaldson trailing edges as a function of flow velocity, Figure 5.5. A quasi-linear relationship is observed between the shedding frequency and flow velocity in the case of truncated and oblique trailing edges, except under lock-in condition. However, this linear relationship is not found for the Donaldson trailing edge. Under lock-in condition, the vibration amplitude of the hydrofoil trailing edge is high in comparison to the lock-off condition, so that

its motion takes control of the instability mechanism that leads to vortex shedding and synchronizes the shedding frequency with the body motion frequency. The survey of hydrofoil surface vibration under lock-in condition leads to the identification of the first torsional eigen mode, Ausoni [3]. Increase of the vibration takes place in the case of the Donaldson trailing edge for a very short range of Reynolds number,  $Re_L = 1.1 \cdot 10^6$ . This is due to the low vibration amplitude in comparison to the truncated and oblique trailing edges. Bearman [8] noted that the range of Reynolds number versus the vortex-shedding frequency which is locked to the bluff body eigen frequency is dependent on oscillation amplitude. The larger the amplitude, the larger the range of Reynolds number. In the present study, as the lower vibration amplitude is found for the Donaldson trailing edge in comparison to the truncated and oblique trailing edges, the shorter Reynolds number range under lock-in condition is observed. Moreover, largely higher shedding frequency is found for the Donaldson trailing edge in comparison to the truncated and oblique trailing edges, which both follow the same trend. As the Reynolds number increases, the separation point on the pressure side of Donaldson trailing edge moves towards the trailing edge. The distance between two separated shear layers on the upper and lower side of Donaldson trailing edge become smaller in comparison to the truncated trailing edge. As a result, the vortex rolling up time decreases and the shedding frequency increases.

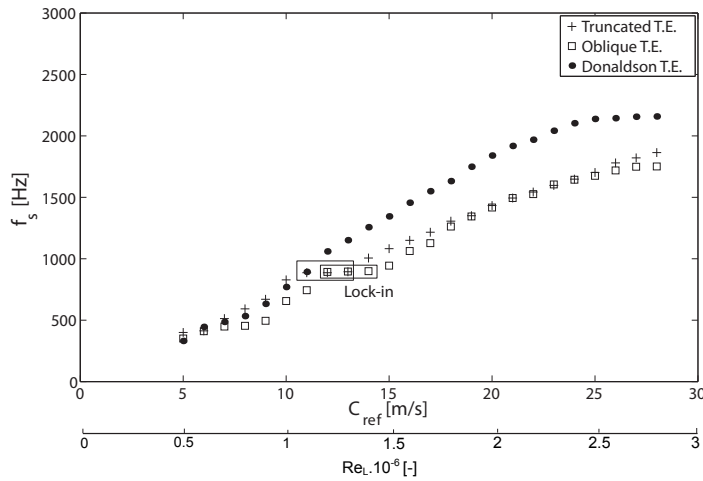


Figure 5.5: Shedding frequency versus Reynolds number, LDV measurement

The normalized frequency or Strouhal number,  $fh/C_{ref}$ , for the three trailing edges is illustrated in Figure 5.6 under lock-off condition, where  $h$  is the maximum thickness of the hydrofoil. A higher Strouhal number is found for the Donaldson trailing edge as compared to the truncated and oblique cases. The Strouhal number is not constant over the entire flow velocity range, particularly for the oblique and Donaldson trailing edges. As the flow velocity increases, a slight decrease in Strouhal number is observed in the case of the truncated trailing edge. This is due to increasing of boundary layer thickness at the trailing edge when flow velocity increases, [3]. However, in the case of the Donaldson and oblique trailing edges, the Strouhal number passes through a maximum. This is due to the difference in boundary layer evolution versus flow velocity at the Donaldson hydrofoil trailing edge in comparison to the truncated case as observed in Figure 4.7b. As flow

velocity increases, the boundary layer thickness passes through a minimum in the case of the Donaldson trailing edge.

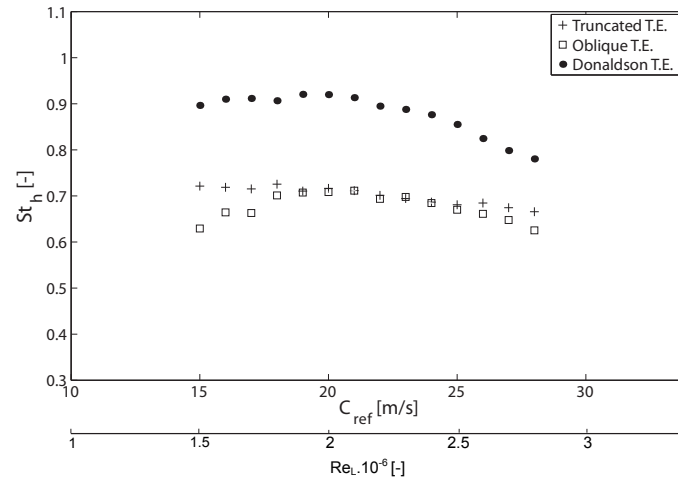


Figure 5.6: Strouhal number versus versus Reynolds number

According to Ausoni [3], a constant Strouhal number versus velocity can be obtained using the boundary layer thickness at the truncated trailing edge. As the boundary layer thickness for different velocity at the separation point is not available on the pressure side of Donaldson trailing edge, the velocity profile thickness at  $x/L = 0.99$ , Figure 4.7b, is used to observe the effect of velocity profile thickness on the Strouhal number,  $St_\delta$ , Figure 5.7. The result shows that nearly a constant Strouhal number for different velocities is also observed in the case of Donaldson trailing edge using the velocity profile thickness.

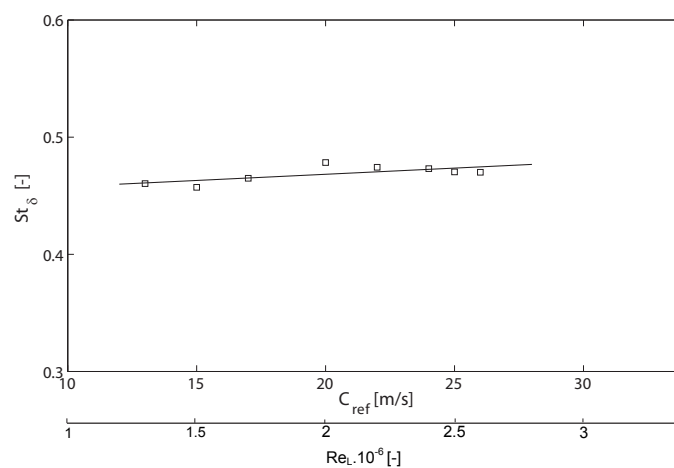


Figure 5.7: Strouhal number using boundary layer thickness at trailing edge,  $St_\delta$ , in the case of Donaldson trailing edge



# Chapter 6

## Effect of trailing edge shape on vortex formation mechanism

The effects of oblique and Donaldson trailing edge geometries on the vortex formation mechanism at trailing edge are studied using flow visualization as well as PIV-POD techniques. The former is performed using cavitating vortices as means of visualizing and the latter under cavitation-free condition. The cavitation in the vortices formed in the wake occurs when the pressure falls below the vapor pressure. Moreover, no cavitation is observed on the hydrofoil surface in our case study before the vortex cavitation in the wake. Consequently, the flow visualization using the vortex cavitation is possible. Cavitation is considered as a passive agent of flow visualization in terms of vortex span-wise organization. However, it has the influence on the vortex shedding frequency, [3].

Top view visualization of cavitating vortex street under lock-in and lock-off condition in the case truncated trailing edge is observed in Figure 6.1. Under lock-in condition, the trailing edge vibrations leads to more organized wake structure and the vorticity lines are parallel to the hydrofoil trailing edge, which makes it easier to observe, Figure 6.1b. However, under lock-off condition, the vortices are no more parallel to the trailing edge and strongly a 3D vortex structure is observed, Figure 6.1a.

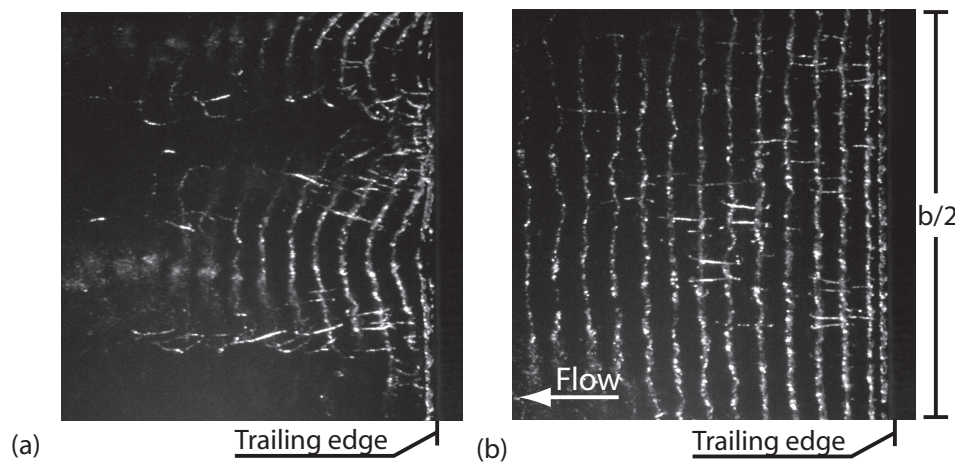


Figure 6.1: Top view visualization of cavitating vortex street, (a)lock-off, and (b)lock-in condition, Ausoni [3]

## 6.1 Lock-in

The flow visualization in the case of truncated and oblique trailing edges under lock-in condition is presented in Figure 6.2 using cavitation vortices. In the case of the truncated trailing edge, the flow separation position is fixed at the truncated part of the trailing edge, Figure 6.2a. With the oblique truncation, the location of the lower vortex detachment is obviously shifted upstream with respect to the upper one, forming a vortex along the inclined surface of the cut, Figure 6.2b. As a result, when the upper vortex rolls up, it coincides with the passage of the lower vortex, leading to their collision. This strong interaction leads to a redistribution of the vorticity, which does not concentrate within the core of Karman vortices any more. A significant part of the vorticity is carried by tiny vortices in random directions. Moreover, vortex collision also leads to a sudden suppression of cavitation in the lower vortex while it persists in the upper one. This is a clear indication of the pressure increase in the core of the lower vortex, which results from the reduction of coherent vorticity. The flow visualization in the case of oblique and Donaldson trailing edges is presented in Figure 6.3. As previously mentioned the lock-in condition is not reached in the case of the Donaldson trailing edge. As a result, the visualization is not as clear as in the case of oblique trailing edge. However, the vortex collision in the case of Donaldson trailing edge is observed clearly for the fully turbulent boundary layer in section 8.3.

The vortex generation mechanism from the truncated and oblique trailing edges under cavitation free condition is analyzed via PIV-POD phase-locked average by considering 1000 snapshots and the first ten most energetic POD modes. The Proper-Orthogonal-Decomposition, POD, is used as a post processing technique to identify large coherent structures in the wake. POD is a powerful energy-based filter, which allows for an extraction of the most energetic modes associated with vortex shedding. It also offers the possibility to compute the phase of randomly acquired velocity fields. In our specific case study, POD method offers an interesting way to perform phase locked averaging of the velocity fluctuation without the need of external trigger. The PIV-POD results shows the collision of upper and lower vortices in the case of oblique trailing edge, Figure 6.4, similar to the flow visualization using the cavitating vortex. Consequently, it is concluded that cavitation has no effect on the collision of upper and lower vortices.

Finally, the vortex-induced vibration reduction in the oblique trailing edges is addressed and thought to be a result of collision between the upper and the lower vortices.

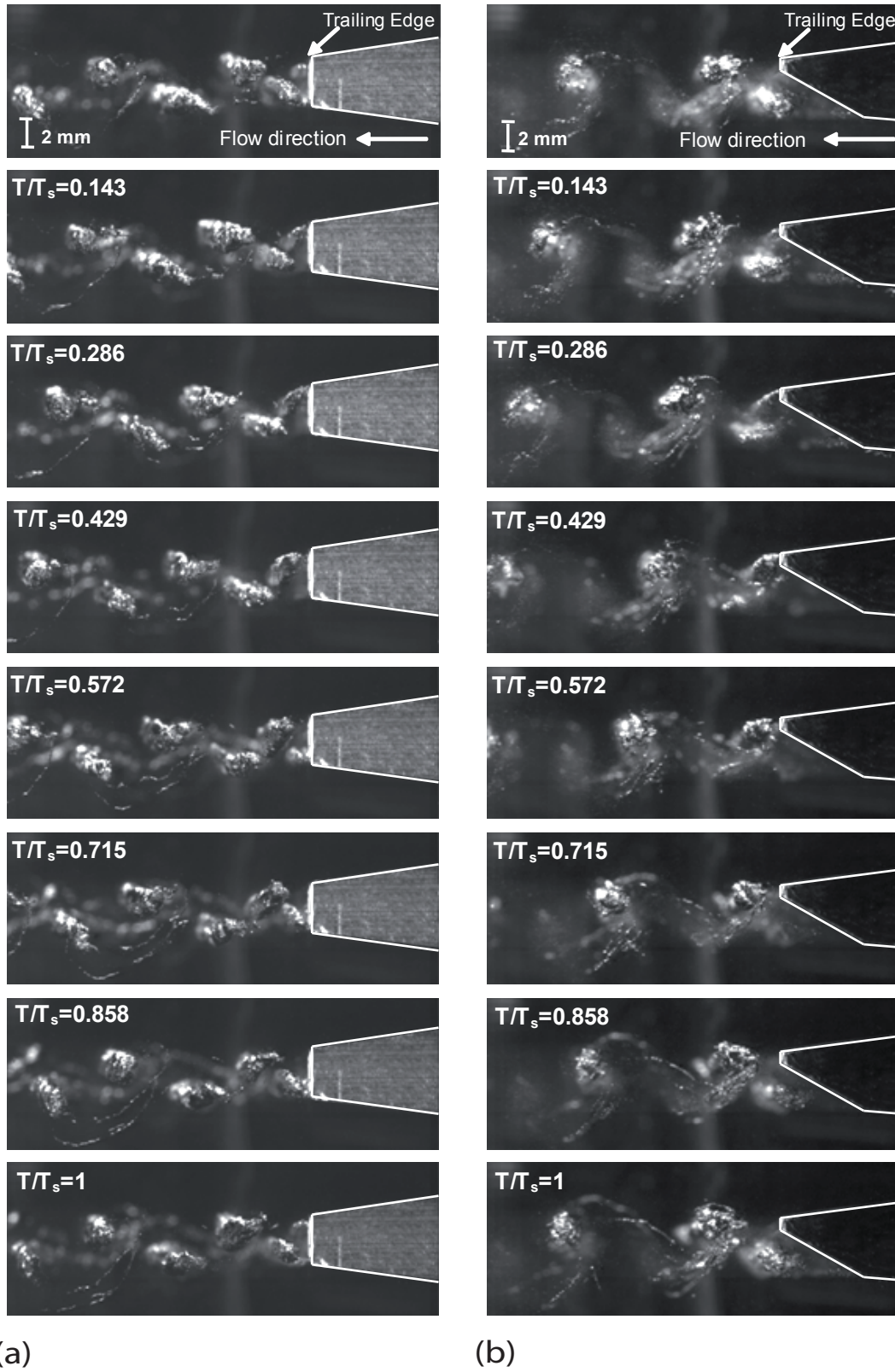


Figure 6.2: High-speed visualization of the wake dynamics, (a) Truncated T. E.,  $Re_L = 1.2 \cdot 10^6$ ,  $\sigma = 0.8$ , (b) Oblique T. E.,  $Re_L = 1.3 \cdot 10^6$ ,  $\sigma = 0.6$ ,  $12000 fps$



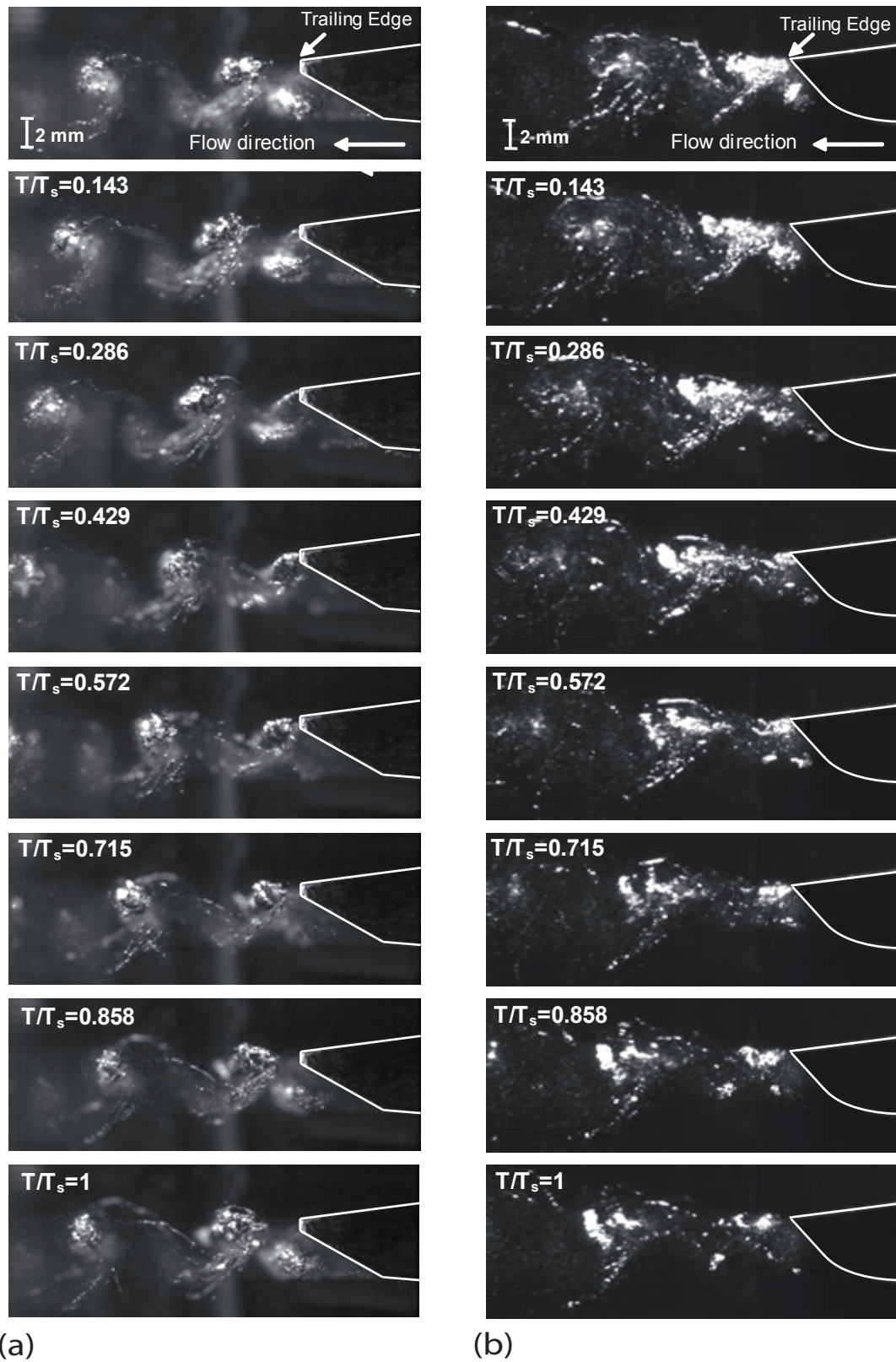


Figure 6.3: High-speed visualization of the wake dynamics, (a)Oblique T. E.,  $Re_L = 1.3 \cdot 10^6$ ,  $\sigma = 0.6$ , (b)Donaldson T. E.,  $Re_L = 1.1 \cdot 10^6$ ,  $\sigma = 0.5$ , 12000fps



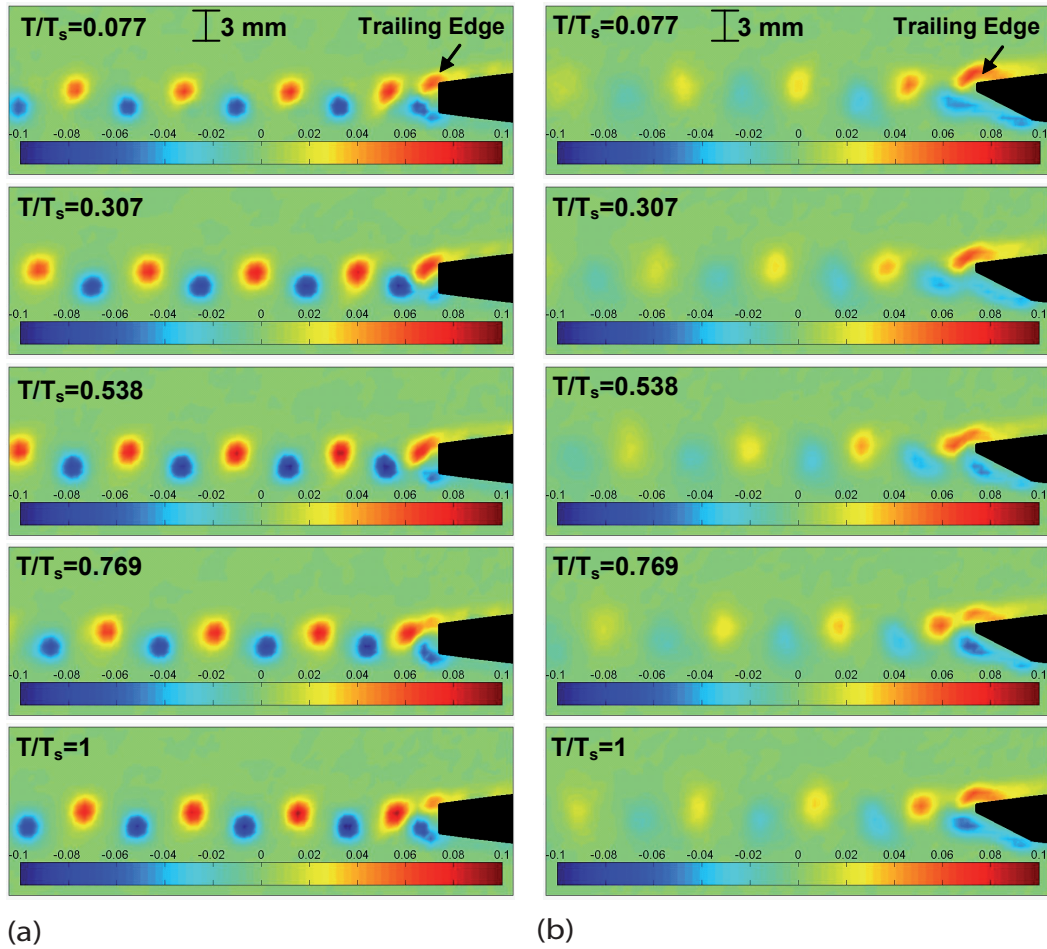


Figure 6.4: Wake visualization (one shedding period), normalized vorticity, (a) Truncated T.E.,  $Re_L = 1.2 \cdot 10^6$ , (b) Oblique T.E.,  $Re_L = 1.3 \cdot 10^6$

## 6.2 Lock-off

As it was noted under lock-off condition the wake flow is not organized similar to the lock-in condition and a 3D vortex structure in span-wise direction is observed. As a result, the flow visualization using cavitation and PIV-POD technique under free cavitation can not show the vortex collision as observed under lock-in condition. The example of the wake flow visualization under lock-off condition in the case of the oblique trailing edge is illustrated in Figure 6.5,  $Re_L = 1.7 \cdot 10^6$ . However, the LDV measurement results presented in the next chapter confirm that the collision of upper and lower vortices is also occurred under lock-off condition.

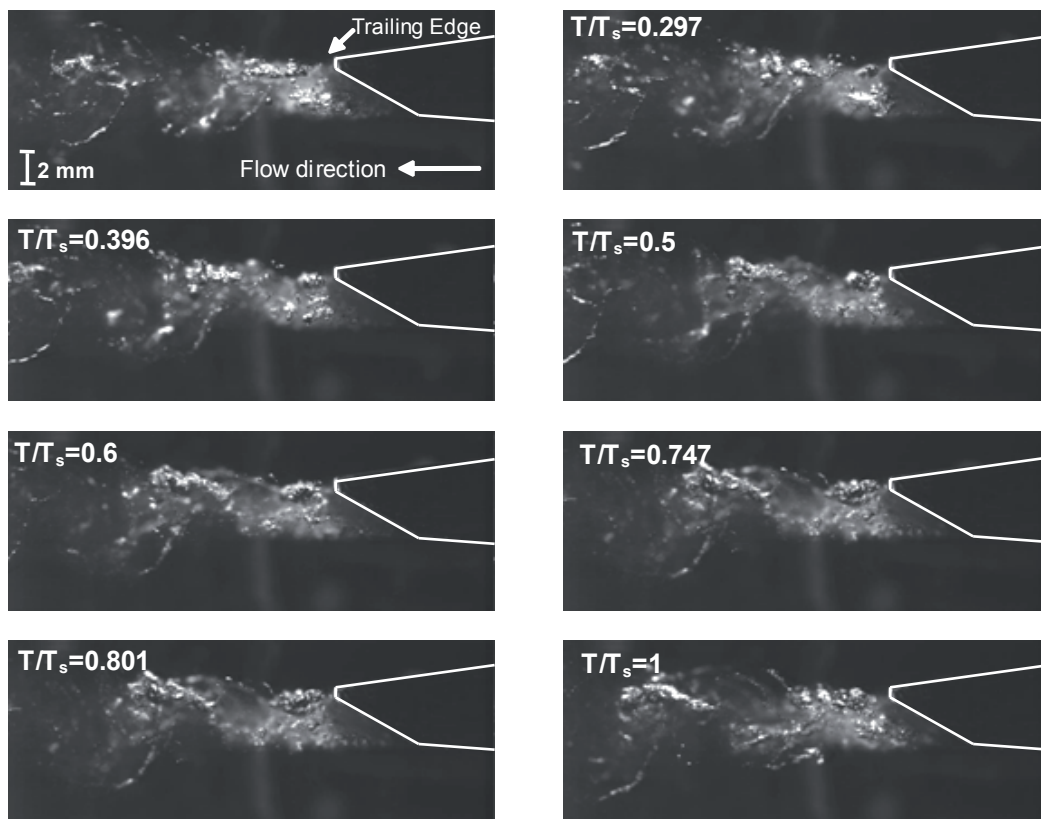


Figure 6.5: High-speed visualization of the wake dynamics in the case of oblique trailing edge under lock-off condition,  $Re_L = 1.7 \cdot 10^6$ ,  $\sigma = 0.65$ ,  $12000 fps$

# Chapter 7

## Effect of trailing edge shape on wake flow

The effects of oblique and Donaldson trailing edges on the wake flow under lock-in and lock-off conditions are investigated in this chapter. The time-averaged velocity profiles are studied for oblique and Donaldson trailing edges. Velocity profiles at the passage time of the vortex are presented using LDV phase-locked average in the case of the oblique trailing edge. In addition, the vortex characteristics properties along the wake are revealed. In all cases, the results are compared with the truncated trailing edge as a reference case study.

### 7.1 Wake flow under lock-in condition

Wake flow velocity under lock-in condition is presented in two sections. In first section the time-averaged velocity is illustrated at different positions along the wake in the case of truncated, oblique, and Donaldson trailing edges. In the second section LDV phase-locked average measurements are presented, thus allowing to further analyzing the wake dynamics. Phase-locked average of the velocity field is performed to extract the deterministic and periodic component of the signal from the turbulent noise. To this end, a high frequency accelerometer fitted to the hydrofoil support is used as reference signal, providing a single pulse at every period of vortex generation. Phase-locked average is only possible under lock-in condition, otherwise the vibration signal is not appropriate.

#### 7.1.1 Time-averaged velocity profiles

Normalized by the free-stream velocity, the mean value and standard deviation of the stream wise velocity are illustrated in Figures 7.1 and 7.2 for the truncated and oblique trailing edges under lock-in condition. Since lock-in condition was not detected clearly for the Donaldson trailing edge, the measurement is performed under condition corresponding to the maximum vibration amplitude, Figure 7.3. In all cases, as the flow progresses downstream of the trailing edge, the velocity deficit is reduced. However, in the case of the oblique and Donaldson trailing edges, a slight asymmetric thickening of the wake downward is observed in velocity profile. This asymmetric wake velocity profile could be related to the asymmetric boundary layer on the Donaldson trailing edge surface where the boundary layer on the pressure side of hydrofoil is thicker than the suction side.





### 7.1.2 Velocity profiles at the passage time of the vortex

LDV phase-locked average measurements are performed to further analyzing the wake dynamics in the case of truncated and oblique trailing edges. LDV phase-locked average procedure is applied directly by sorting the samples into the corresponding phase based on the arrival time. After phase sorting of the samples, the vortex shedding period is divided into  $N_s$  segments. The mean value is calculated within each segment. The same procedure is performed for all points on the vertical measurement line. As a result, the mean velocity of the measurement points at the same phase, time, is obtained and the mean velocity profile corresponding to each phase can be plotted. Stream wise velocity profiles at the passage time of the upper and lower vortices through the measurement line are illustrated for the case of truncated and oblique trailing edges, Figure 7.4. The Oseen velocity profile was applied to fit on the LDV measurement Data to find the vortex core size. However, the acceptable results were not obtained due to the complexity of the wake flow. Consequently, the maximum,  $C_{x_{max}}$ , and minimum,  $C_{x_{min}}$ , stream wise velocities are recorded at the vortex core edges furthest and nearest to the wake centerline respectively to estimate the vortex core diameter. In the case of the truncated trailing edge, the upper and lower vortices have the same core diameter, contrary to the oblique trailing edge, where a larger vortex core diameter is found for the lower vortex. The diameter of upper and lower vortices in the near wake of the oblique trailing edge is found to be almost two and three times larger than the upper and lower vortices in the wake of the truncated one. Greater minimum,  $C_{x_{min}}$ , and maximum,  $C_{x_{max}}$ , stream wise velocities are found for the truncated trailing edge in comparison to the oblique trailing edge, as observed in Figures 7.4a and 7.4b. Stream wise velocity profiles of the upper and lower vortices in the wake of truncated trailing edge show equal minimum and maximum stream wise velocity values. This is contrary to the oblique trailing edge, where a greater minimum stream wise velocity value is found for the upper vortex in comparison to the lower one, Figures 7.4c and 7.4d.

As it was noted in the case of Donaldson trailing edge, the vibration amplitude is low in comparison to the truncated and oblique trailing edges and lock-in condition is not found. Therefore LDV phase-locked average is not performed and the velocity profiles at the passage time of the vortex are not presented in the case of Donaldson trailing edge.

### 7.1.3 Vortex properties

The normalized vortex core radius evolution along the wake of the oblique trailing edge is presented in Figure 7.5 and compared with the vortex core radius of the truncated trailing edge, Ausoni [3]. The radius of the vortices becomes larger along the wake in both cases. However, the radius of the vortices in the case of the oblique trailing edge increases at a higher rate along the wake than for the truncated trailing edge. Moreover, a larger vortex core size is observed for the lower vortex along the wake of the oblique trailing edge than the upper vortex. However, an equal vortex core radius is found for upper and lower vortices along the wake in the case of truncated trailing edge.

According to Ausoni [3], for a given vortex, the relationship between the advection velocity of the vortices,  $C_{adv}$ , which is assumed to be constant on the vortex core diameter, maximum and minimum stream wise velocities,  $C_{x_{max}}$  and  $C_{x_{min}}$  respectively, and the

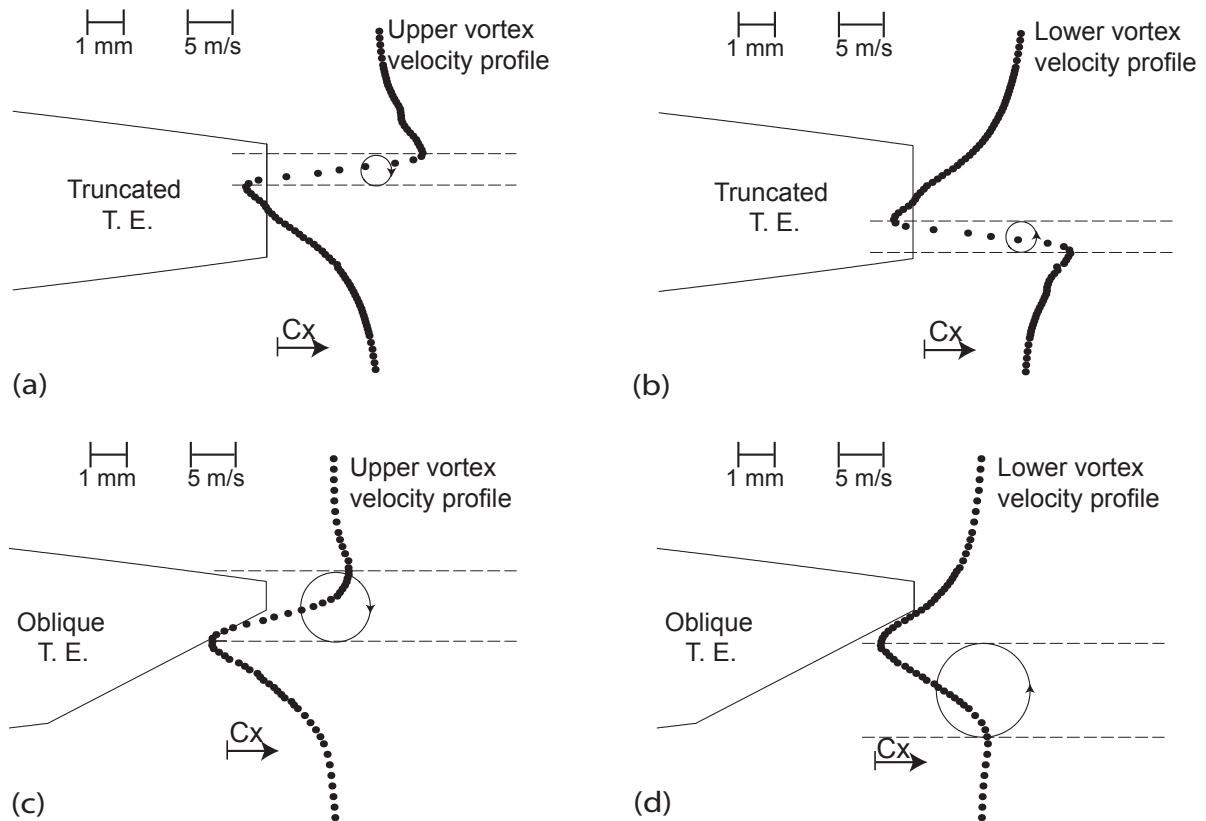


Figure 7.4: Instantaneous velocity profiles at the passage time of the vortex through the measurement line and vortex core size for truncated and oblique trailing edges

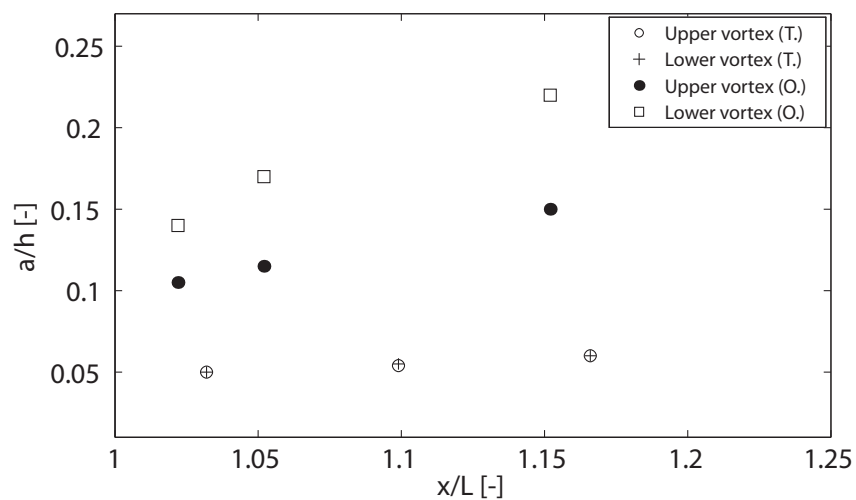


Figure 7.5: Normalized vortex core radius at different stations downstream from the trailing edge for truncated,  $Re_L = 1.2 \cdot 10^6$ , and oblique trailing edges,  $Re_L = 1.3 \cdot 10^6$

stream wise velocity at the edge of the vortex viscous core,  $C_v$ , is given by the:

$$\begin{aligned} C_{x_{max}} &= C_v + C_{adv} \\ C_{x_{min}} &= -C_v + C_{adv} \end{aligned} \quad (7.1)$$

$C_{x_{max}}$  and  $C_{x_{min}}$  are obtained from the LDV phase-locked average.  $C_{adv}$  and  $C_v$  are estimated and illustrated in the Figures 7.6 and 7.7. In addition, the results are compared with the truncated trailing edge, Ausoni [3]. In the case of the oblique trailing edge, the lower vortex street has a higher advection velocity than the upper vortex street. The difference between the advection velocity of upper and lower vortices becomes similar far the wake. Moreover, a higher advection velocity is found for the oblique trailing edge along the wake in comparison to the truncated one.

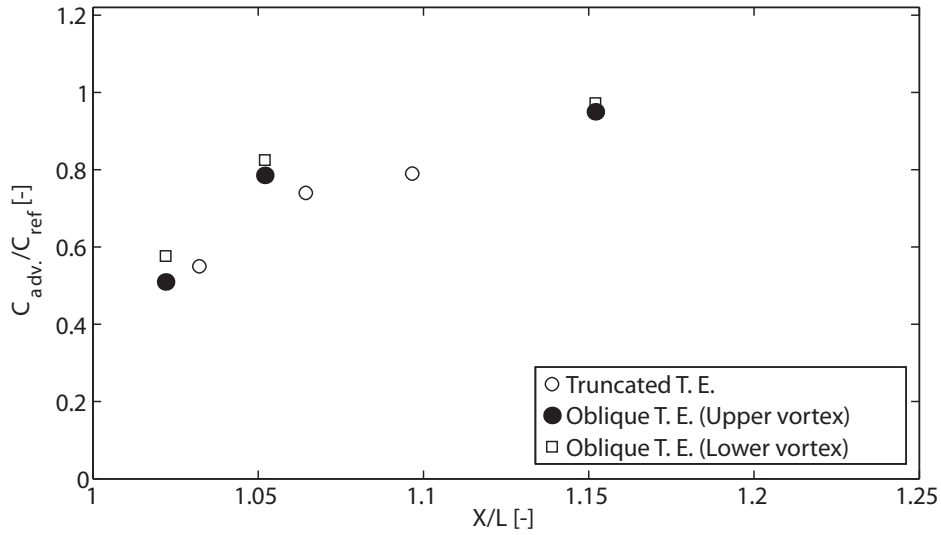


Figure 7.6: Normalized vortex advection velocity at different stations downstream of the truncated,  $Re_L = 1.2 \cdot 10^6$ , and oblique trailing edges,  $Re_L = 1.3 \cdot 10^6$

The stream wise vortex velocity,  $C_v$ , evolution along the wake is illustrated in Figure 7.7. A higher vortex velocity is found in the case of the truncated trailing edge. Moreover, a difference between the vortex velocity of the upper and lower vortices is observed in the case of the oblique trailing edge, where a higher vortex velocity value corresponding to the upper vortex street.

The strength of the vortex is defined according to the following equation:

$$\Gamma = 2\pi a C_v \quad (7.2)$$

where  $a$  is the viscous core radius and  $C_v$  is the stream wise vortex velocity at its edge. The evolution of the normalized vortex strength along the wake in the case of the oblique trailing edge is illustrated in Figure 7.8. Different Tangential velocities and vortex core radius are found for the upper and lower vortex streets. However, nearly the same vortex strength is observed for both vortex streets.



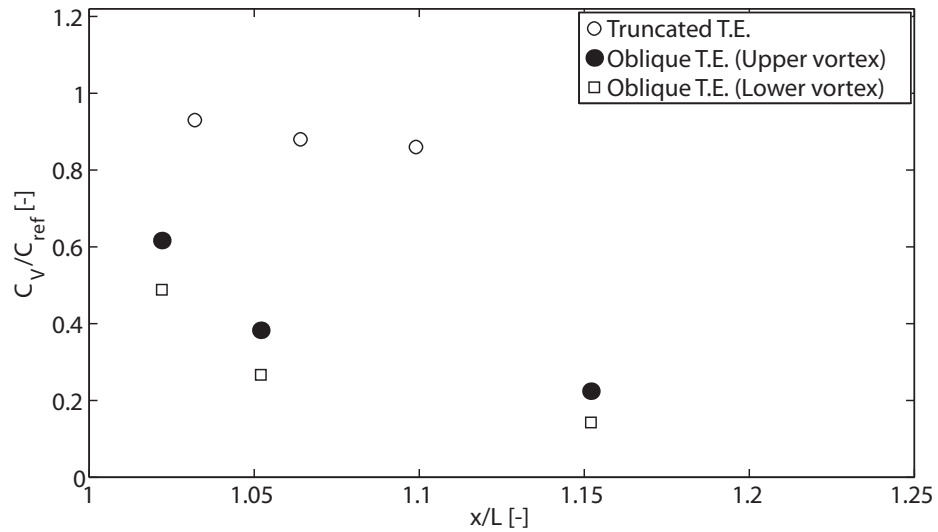


Figure 7.7: Normalized vortex tangential velocity at different stations downstream of the truncated,  $Re_L = 1.2 \cdot 10^6$ , and oblique trailing edges,  $Re_L = 1.3 \cdot 10^6$

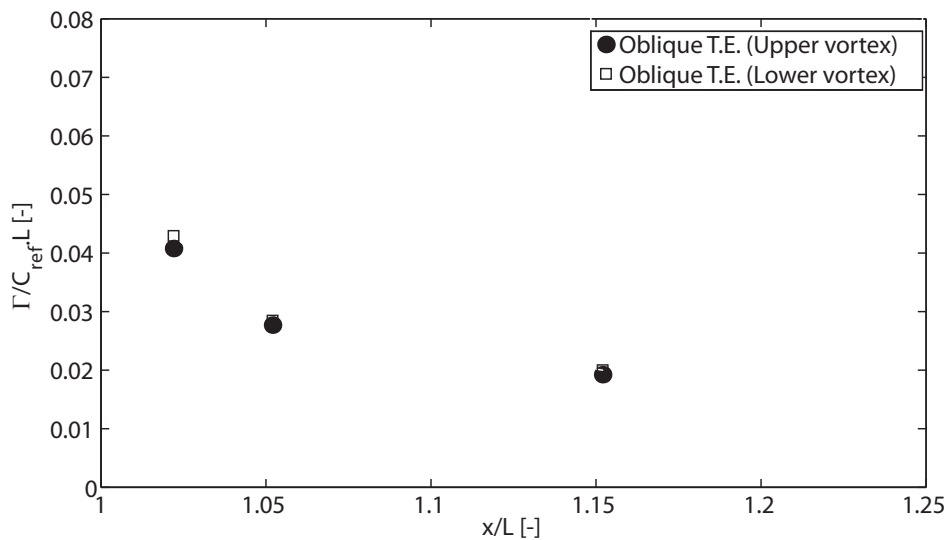


Figure 7.8: Normalized vortex core strength at different stations downstream of the trailing edge

The vortex shedding development along the wake of the truncated and oblique trailing edges under cavitation-free condition is analyzed via PIV-POD phase average. A snapshot of the magnitude of the instantaneous velocity, normalized with the reference velocity, along the wake of the truncated and oblique trailing edges is given in Figure 7.9. The magnitude of the velocity decreases along the wake in both cases. However, a lower velocity magnitude is observed in the far wake of the truncated trailing edge due to the collision of upper and lower vortices.

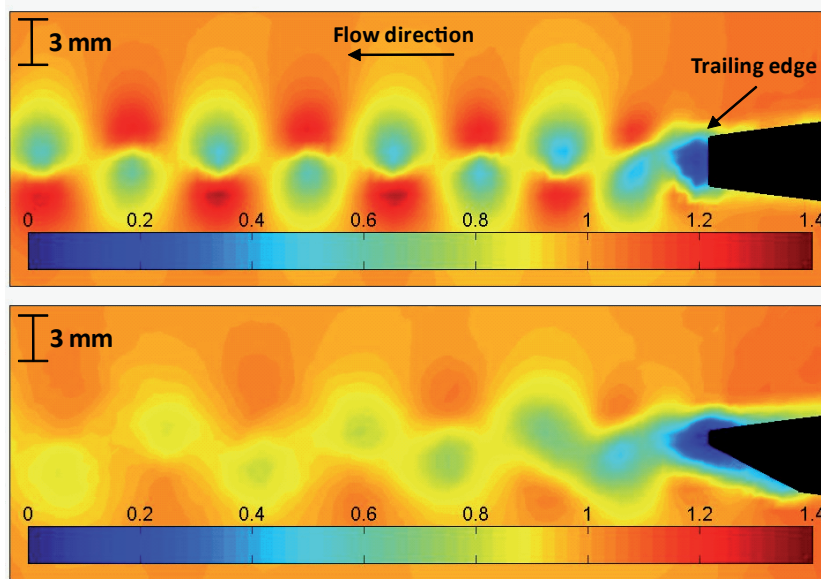


Figure 7.9: A snapshot of normalized magnitude of the instantaneous velocity field, lock-in

#### 7.1.4 Inter-vortex spacings

The vortex street arrangement along the wake is investigated using PIV-POD, Figure 7.10.  $S_r$  and  $S_l$  are defined as the distance between the lower vortex and two neighboring upper vortices at the right and left side respectively. According to the work of von Karman [76] and Rosenhead [62] the stable vortex street shows a perfect alternate shedding,  $S_l = S_r$ . This is well observed for truncated trailing edge. However, this is not observed in the near wake of the oblique trailing edge due to the unequal distance,  $S_l > S_r$ , between the lower vortex and the two neighboring upper vortices, Figure 7.10b. The unequal distance between the lower vortex and two neighboring upper vortices in the near wake, introduced by the oblique truncation of the trailing edge, is found to vanish in the far wake, where more organized and ideal alternate shedding is recovered, as observed for the blunt trailing edge.

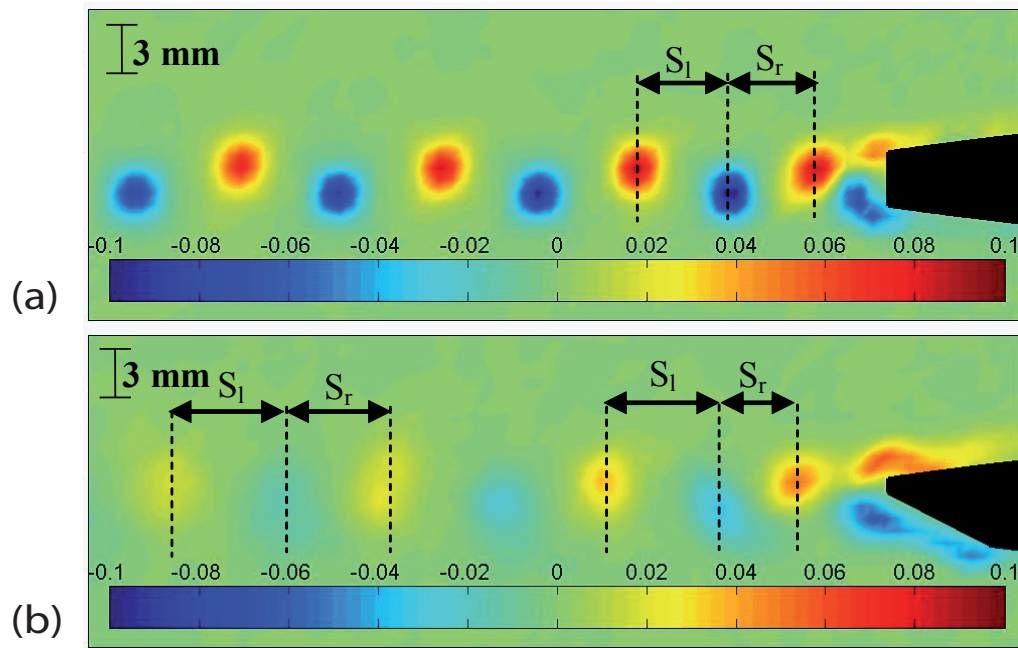


Figure 7.10: Vortex arrangement along the wake using PIV-POD, normalized vorticity, lock-in, (a)Truncated trailing edge, (b)Oblique trailing edge

The passage of vortices through the measurement line and their arrangement along the wake in one vortex shedding period using LDV phase-locked average is presented in Figure 7.11. Moreover, the phase shift between upper and lower vortices is observed in the case of the oblique trailing edge in contrast to the truncated one.

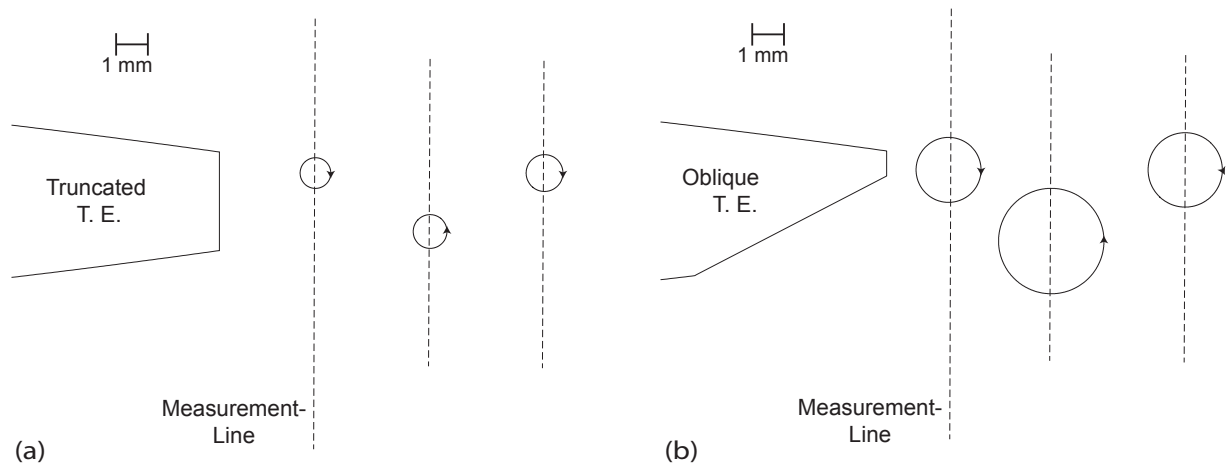


Figure 7.11: Vortex arrangement along the wake using LDV phase-locked average, lock-in, (a)Truncated trailing edge, (b)Oblique trailing edge

The vortex spacing ratio of the double row of vortices in the wake,  $b_s/a_s$ , is defined, where  $b_s$  and  $a_s$  denote the lateral and longitudinal vortex spacing respectively. A symmetric double row vortex street is revealed in the wake of the truncated trailing edge. Therefore, the vortex spacing ratio of the truncated trailing edge is considered as the reference value for stable vortex street in the wake of a NACA 0009 hydrofoil, Figure 7.12. when calculating the spacing ratio at different stations downstream from the oblique trailing edge a high value is observed for the spacing ratio near the oblique trailing edge. This ratio decreases along the wake in such a way that its value approaches the spacing ratio value of the truncated trailing edge. It is concluded that the vortex street near the oblique trailing edge is unstable. However, it becomes stable far from the trailing edge.

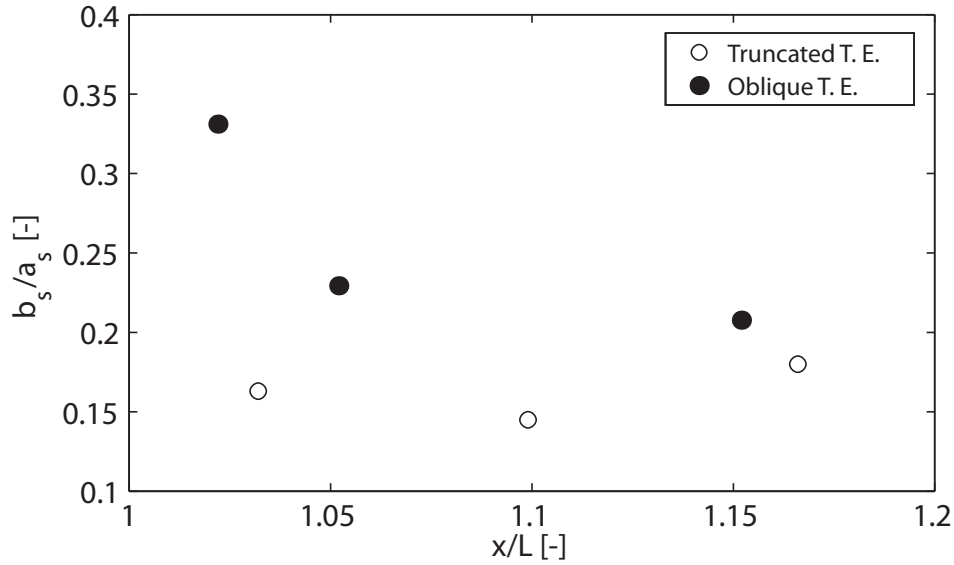


Figure 7.12: Vortex spacing ratio in the case of truncated and oblique trailing edges

## 7.2 Wake flow under lock-off condition

As it was noted previously, in most cases, the lock-in condition is selected intentionally to illustrate the fundamental difference between truncated, oblique trailing edge hydrofoils. When the vortex shedding frequency is locked on hydrofoil resonance frequency, the vorticity lines are parallel to the hydrofoil trailing edge, which makes it easier to observe the wake dynamic and perform measurements of phase locked average of the wake velocity. However, the wake flow measurement is also performed under lock-off condition,  $Re_L = 2 \cdot 10^6$ , to verify the similarity between the wake flow under lock-in and lock-off conditions.

### 7.2.1 Time-averaged velocity profiles

The mean and standard deviation stream wise velocity profiles under lock-off condition are presented in Figures 7.13, 7.14, and 7.15 in the case of truncated, oblique, and Donaldson trailing edges.

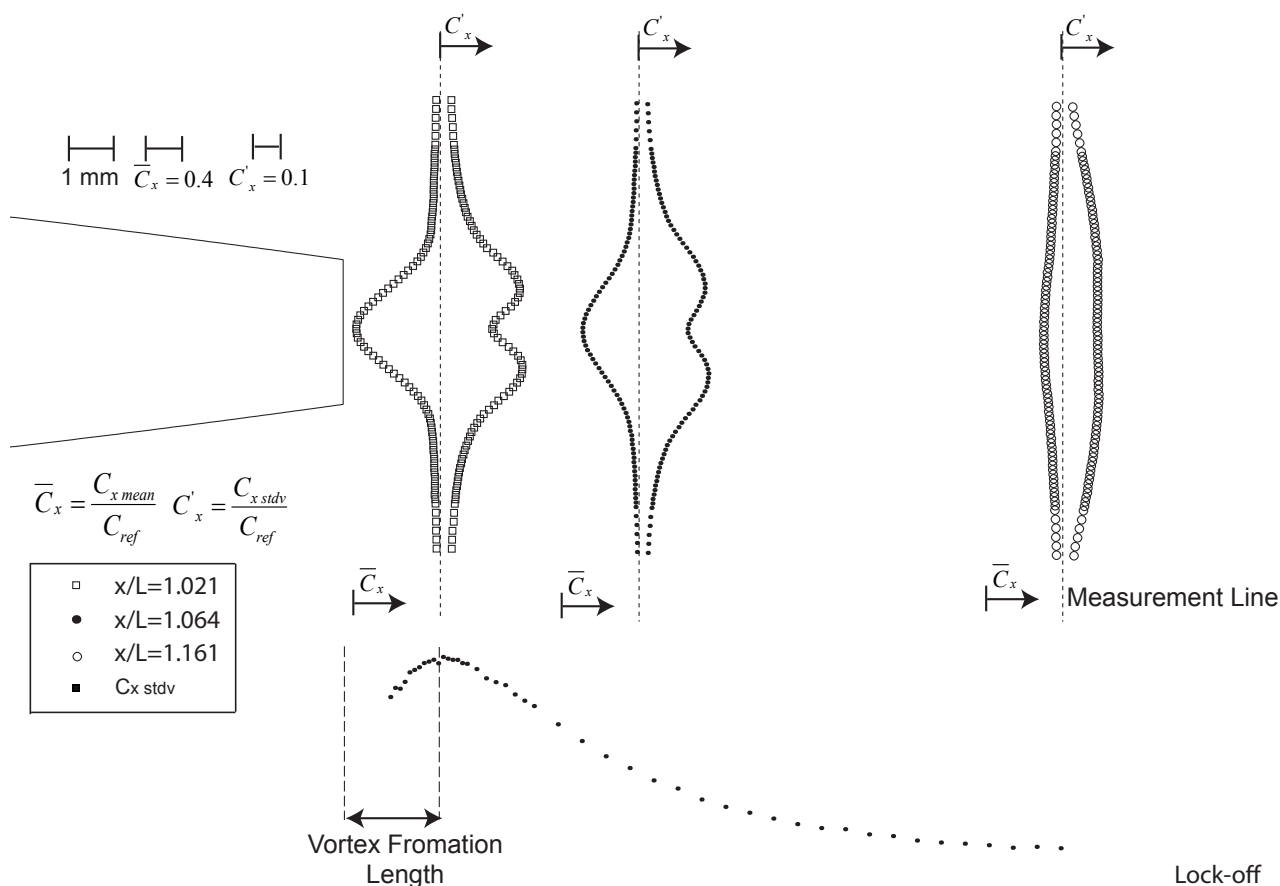


Figure 7.13: Traverse measurements along the wake at different stations under lock-off condition,  $Re_L = 2 \cdot 10^6$ , normalized mean stream wise velocity and stream wise velocity fluctuations for truncated trailing edge

The evolution of velocity deficit and velocity fluctuation peaks shows the same results for lock-in condition such as a asymmetric wake velocity profile in the case of oblique and Donaldson trailing edges, reduce of deficit velocity along the wake. Moreover, a higher velocity fluctuation is found for the lower peak in comparison with the upper peak for the oblique and Donaldson trailing edges. In addition, it is difficult to recognize the velocity fluctuation profile in the far wake under lock-off condition. The three-dimensional aspect of the vortex street under lock-off condition can be noted as the main reason for the characteristic shape being no longer recognizable at a large distance from the trailing edge.

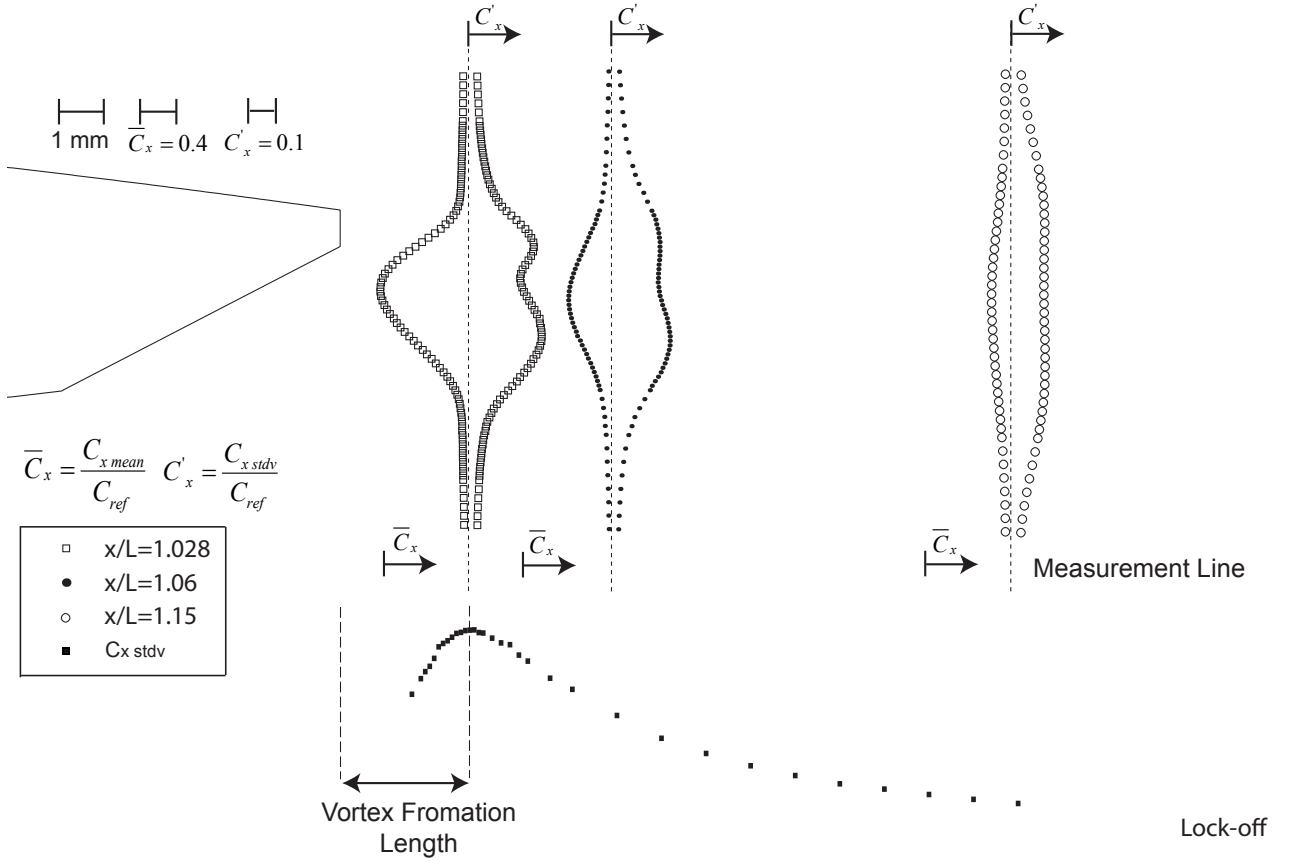


Figure 7.14: Traverse measurements along the wake at different stations under lock-off condition,  $Re_L = 2 \cdot 10^6$ , Normalized mean stream wise velocity and stream wise velocity fluctuations for oblique trailing edge

Position of the maximum stream wise velocity fluctuations along the wake is determined as the end of the vortex formation region, Figures 7.13, 7.14, and 7.15. The comparison of vortex formation length between three trailing edges shows that the vortex formation length for the oblique trailing edge is greater than for the truncated trailing edge while the vortex formation length for the Donaldson trailing edge is greater than for the two other trailing edges. The mean stream wise and transverse velocity as well as stream wise and transverse velocity fluctuation profiles at the end of the vortex formation region are compared for the truncated, oblique, and Donaldson trailing edges, Figure 7.16. We define the wake width as the lateral distance between two points having the maximum stream wise velocity fluctuation at the formation length. The maximum wake thickness corresponds to the Donaldson trailing edge. However, the minimum wake thickness is found for Truncated trailing edge. Moreover, a slight asymmetric thickening of the wake downward is observed in the case of oblique and Donaldson trailing edges. In addition, the minimum stream wise and transverse velocity fluctuation profile between three trailing edges corresponds to the Donaldson trailing edge. In addition, an asymmetric transverse velocity fluctuation is observed in the case of oblique and Donaldson trailing edges. The decrease of fluctuation intensity originates from collision of upper and

lower vortices, which was observed on the high-speed video. The collision between two vortices decreases the transverse fluctuating forces, originating from the shedded vortices. As a result, velocity fluctuations are decreased in the wake.

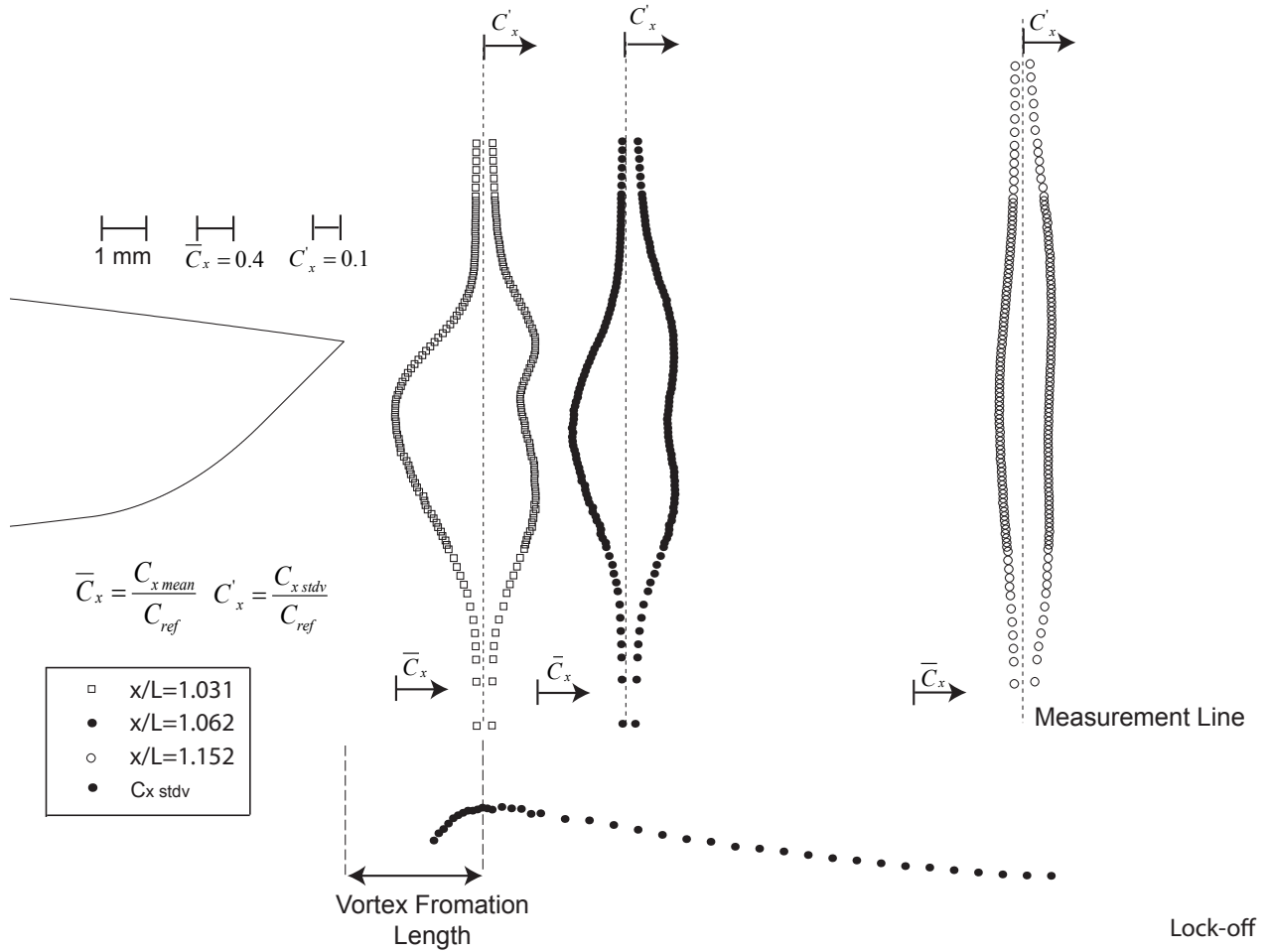


Figure 7.15: Traverse measurements along the wake at different stations under lock-off condition,  $Re_L = 2 \cdot 10^6$ , Normalized mean stream wise velocity and stream wise velocity fluctuations for Donaldson trailing edge

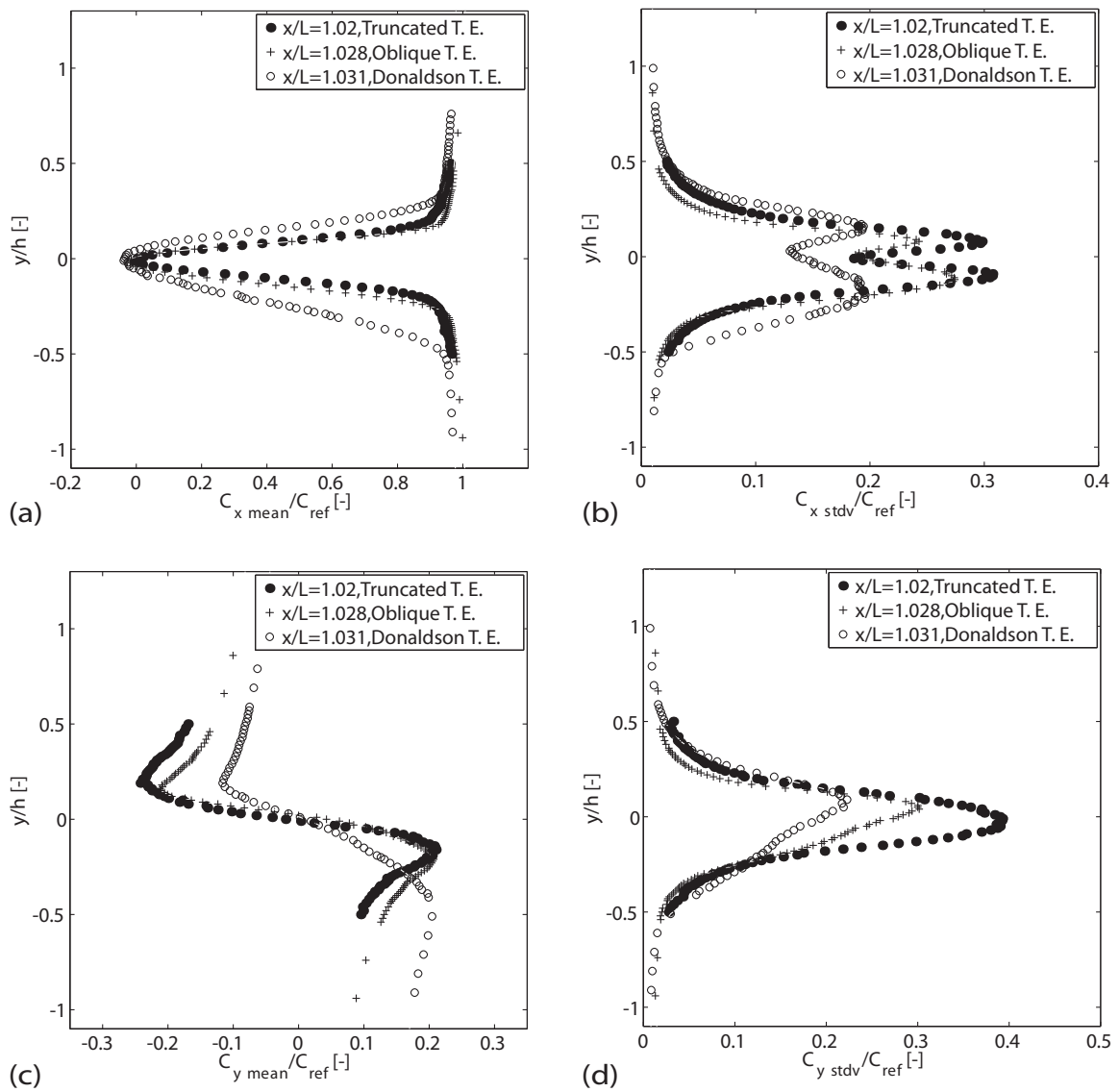


Figure 7.16: Traverse measurement across the wake at the vortex formation position,  $Re_L = 2 \cdot 10^6$ , (a) Normalized mean stream wise velocity, (b) Normalized stream wise velocity fluctuations, (c) Normalized mean transverse velocity, (d) Normalized transverse velocity fluctuations



## Part IV

# Effect of boundary layer state on the wake dynamics



# Chapter 8

## Effect of trailing edge shape on vortex-induced vibration

A distributed roughness is placed on both faces of the hydrofoil leading edge to trigger the laminar-to-turbulent transition and establish a fully turbulent boundary layer. In this chapter the effects of boundary layer state on vortex-induced vibration and vortex formation at the trailing edge are investigated. The vortex-induced vibration results are described in terms of vibration amplitude, vortex shedding frequency, and normalized vortex shedding frequency for truncated, oblique and Donaldson trailing edges. The vortex formation mechanism at the trailing edge is visualized using a high-speed camera.

### 8.1 Vibration amplitude

Vortex-induced vibration is measured with a laser vibrometer at mid-span of the hydrofoil and 10 percent of its chord length, upstream from the trailing edge. Amplitude of the vibration signals is presented for different Reynolds number in the case of truncated, oblique and Donaldson trailing edges, Figure 8.1. An increase in vibration amplitude is found in the case of a tripped transition in comparison to the natural transition. For three trailing edges, a significant increase in vibration amplitude versus Reynolds number is found under lock-in condition. However, the Reynolds number range for Donaldson trailing edge is small under resonance condition. Moreover, maximum and minimum vibration amplitudes are observed in the case of truncated and Donaldson trailing edges respectively, similar to the natural transition case.

### 8.2 Vortex shedding frequency and Strouhal number

Shedding frequency versus Reynolds number in the case of tripped and natural transitions is illustrated in Figure 8.2 for truncated, oblique, and Donaldson trailing edges. A decrease in shedding frequency versus Reynolds number is found in the context of the tripped transition in comparison to the natural transition. It originates from an increase in boundary layer thickness at the trailing edge in the case of the tripped transition. The distance between two upper and lower separated shear layers from the hydrofoil increases. As a result, the vortex formation time increases and the frequency decreases.

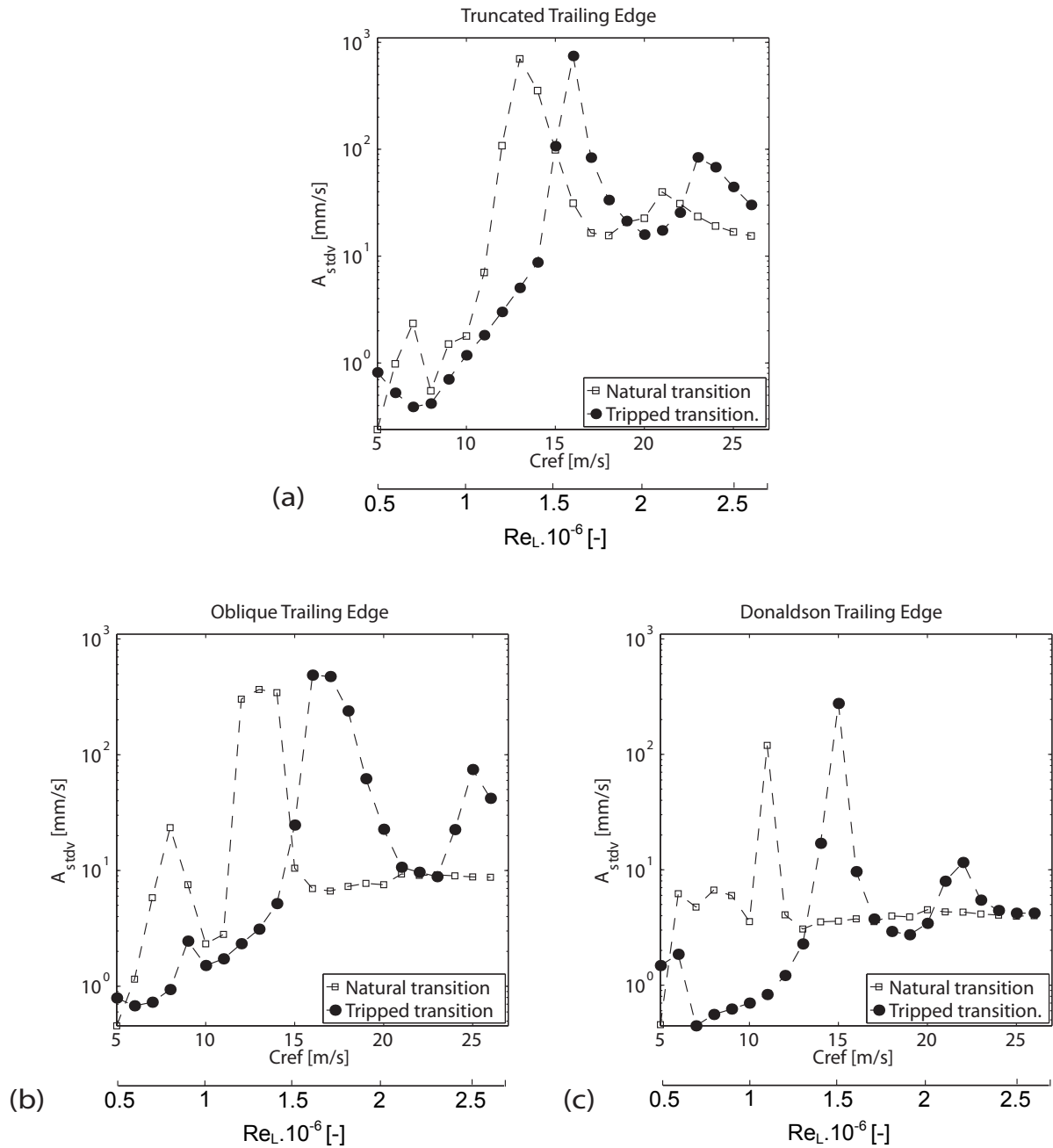


Figure 8.1: Standard deviation of the vibration signal versus Reynolds number, (a)Truncated, (b)Oblique, and (c)Donaldson trailing edge

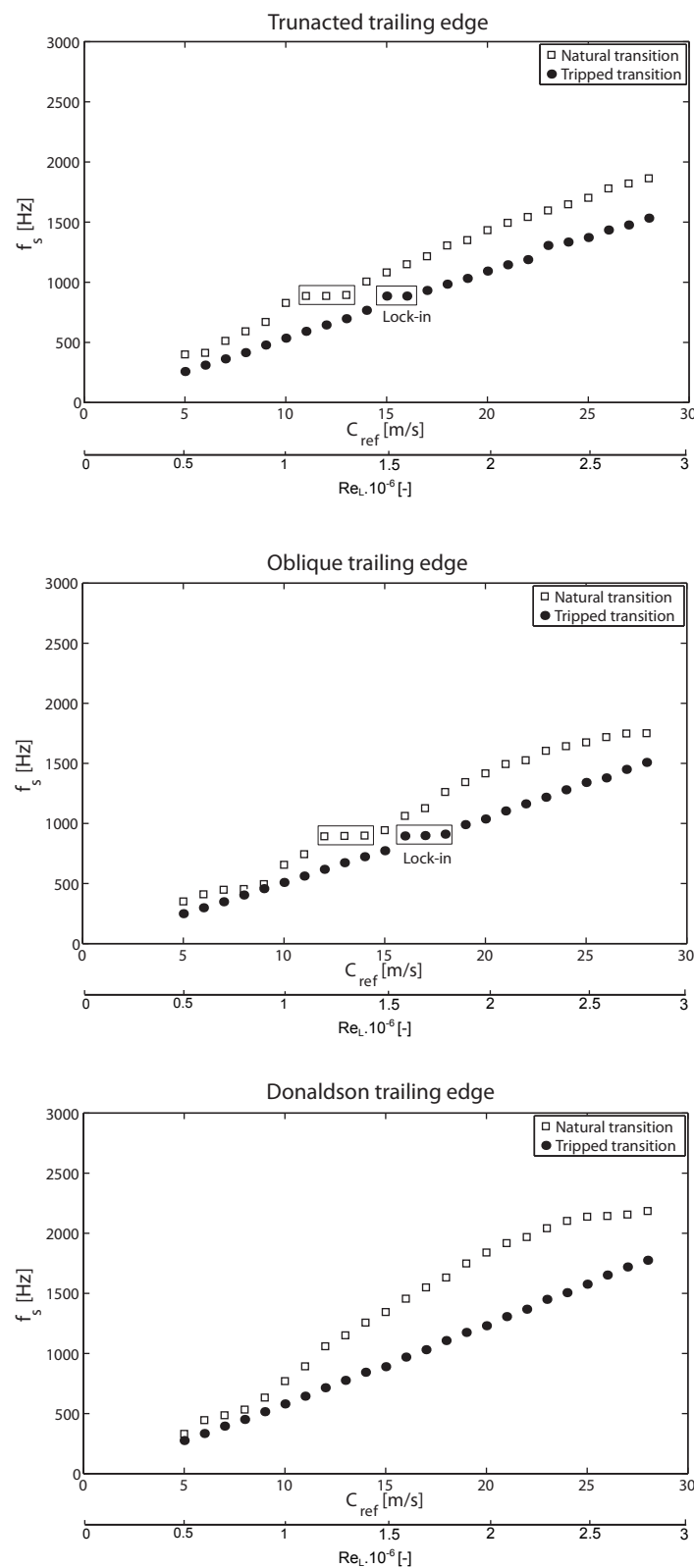


Figure 8.2: Shedding frequency versus Reynolds number

A linear relationship between the shedding frequency and Reynolds number is observed for three trailing edges in the case of tripped transition. However, in the case of natural transition the linear relationship is not found for the Donaldson trailing edge. As the laminar-to-turbulent transition is triggered at the leading edge, the boundary layer thickness decreases linearly with Reynolds number, Ausoni [3]. Consequently, a linear relationship between the shedding frequency and Reynolds number is observed to have a constant Strouhal number. However, in the case of natural transition for the Donaldson trailing edge the relationship between the boundary layer thickness and Reynolds number is not linear, section 4.1. As a result, the shedding frequency increases non-linearly versus Reynolds number reaching a constant Strouhal number. In addition, at high Reynolds numbers the vortex shedding frequencies for natural and tripped transition cases converge together. This could be due to the shift of the laminar-to-turbulent transition towards the leading edge in the case of natural transition as Reynolds number increases. Consequently, the boundary layer becomes fully turbulent similar to the tripped transition boundary layer state and nearly the same frequency is found for both cases. In the case of three trailing edges, the lock-in condition is revealed for a higher range of Reynolds number.

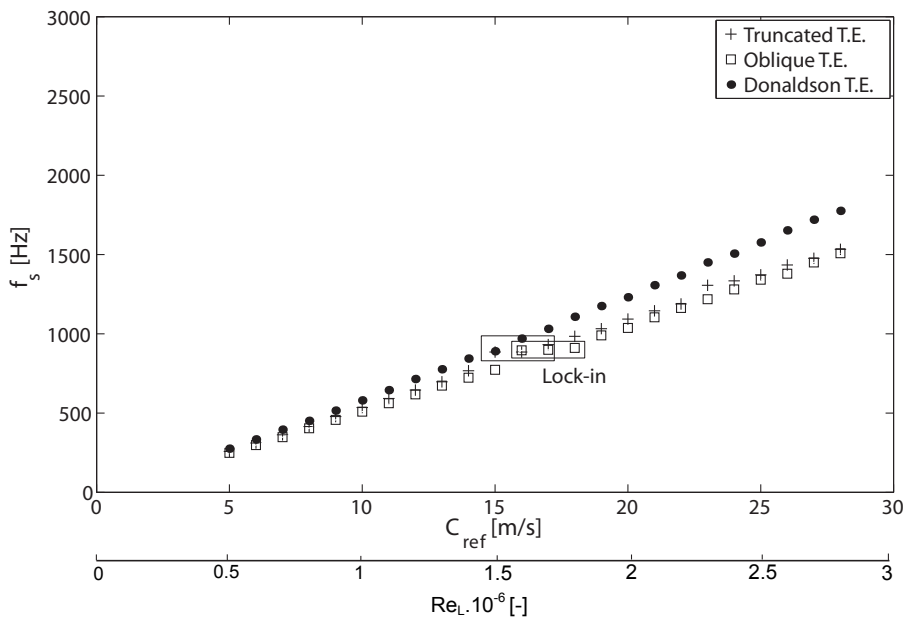


Figure 8.3: Shedding frequency versus free-stream velocity, tripped transition

The shedding frequency versus Reynolds number for tripped transition is plotted in Figure 8.3 in the case of truncated, oblique, and Donaldson trailing edges. Higher shedding frequency is observed for Donaldson trailing edge particularly at high Reynolds numbers. However, nearly the same shedding frequency is found for truncated and oblique trailing edges. Lock-in condition is found for Reynolds numbers ranging from  $Re_L = 1.5 \cdot 10^6$  to  $Re_L = 1.7 \cdot 10^6$  for the truncated,  $Re_L = 1.6 \cdot 10^6$  to  $Re_L = 1.8 \cdot 10^6$  for oblique, and  $Re_L = 1.5 \cdot 10^6$  for Donaldson trailing edges.

The normalized frequency,  $fh/C_{ref}$ , in the context of tripped transition and for three trailing edges is illustrated in Figure 8.4 under lock-off condition, where  $h$  is introduced as the maximum thickness of the hydrofoil. Strouhal number is greater for Donaldson trailing edge compared to the truncated and oblique cases. In addition, Strouhal number does not pass through a maximum with increasing Reynolds number in the case of tripped transition contrary to the natural transition. Moreover, nearly the same Strouhal number is found for truncated and oblique trailing edges. The average Strouhal number is equal to  $St_{hT} = 0.55$ ,  $St_{hO} = 0.53$ , and  $St_{hD} = 0.62$  for truncated, oblique, and Donaldson trailing edges respectively.

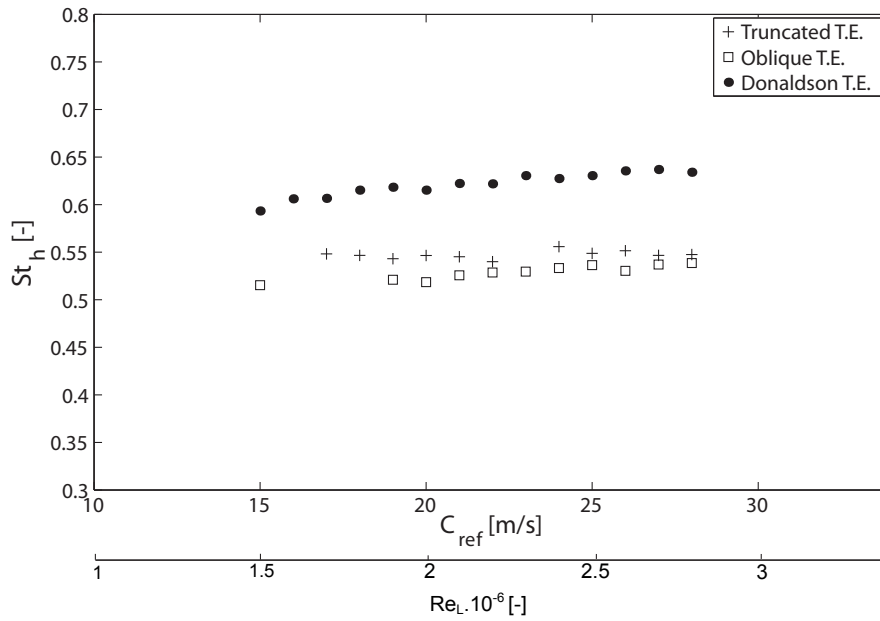


Figure 8.4: Normalized shedding frequency, Strouhal number, versus free-stream velocity, tripped transition

### 8.3 Flow visualization

The wake flow visualization for the oblique trailing edge under lock-in condition and in the context of tripped transition,  $Re_L = 1.5 \cdot 10^6$  is illustrated in Figure 8.5. In the case of tripped transition similar to the natural transition, the sequence clearly shows disorganization of the Karman vortex street in the near wake. The flow on the pressure side of hydrofoil begins to separate at the lower part of the trailing edge, forming a vortex along the inclined surface of the cut. As a result, when the upper vortex rolls up, it coincides with the passage of the lower vortex, leading to their collision. This strong interaction leads to a redistribution of the vorticity, which does not concentrate within the core of Karman vortices any more. A significant part of the vorticity is carried by tiny vortices in random directions. The two vortices are shed with different vortex core diameter.

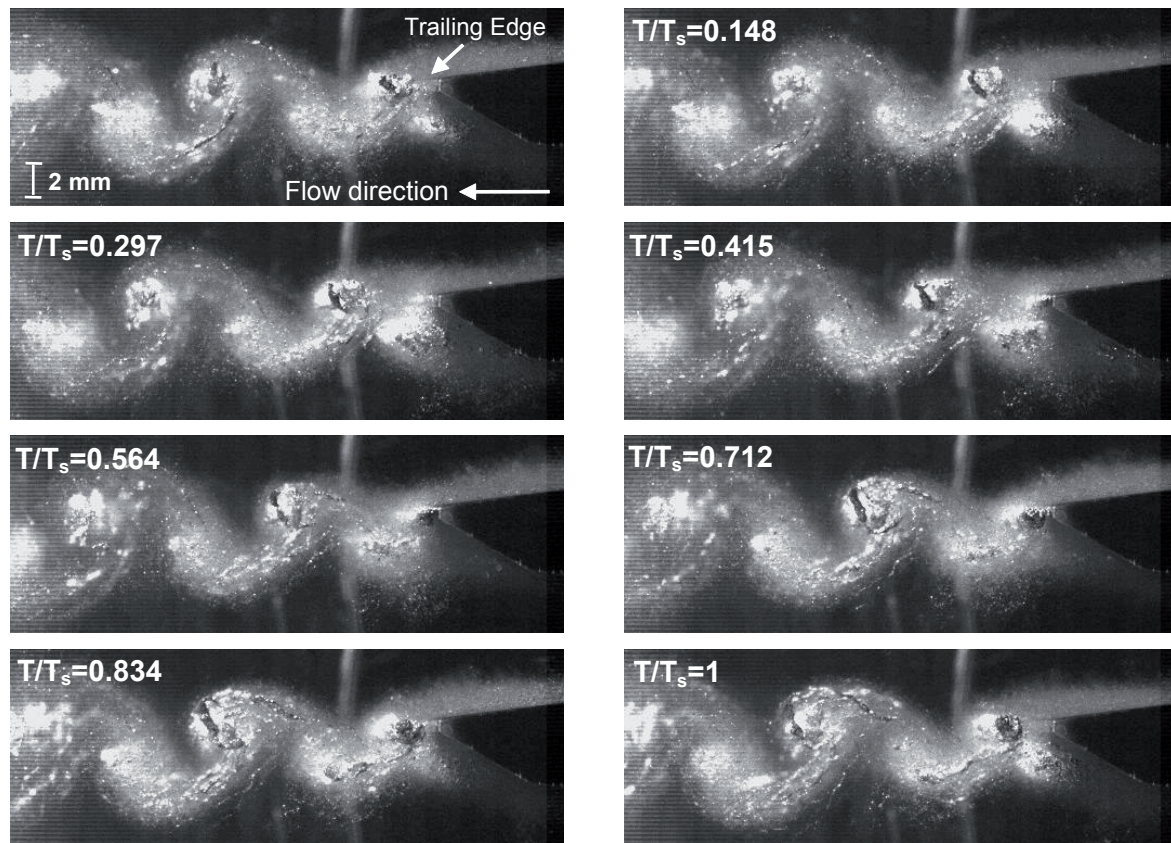


Figure 8.5: Visualization of the wake dynamics, Oblique T. E.,  $Re_L = 1.7 \cdot 10^6$ ,  $\sigma = 0.46$

In the case of Donaldson trailing edge, the visualization is performed using small bubbles which are generated due to the presence of the roughness at the leading edge, as observed in figure 8.6. The images show that the flow is separated on curve side of trailing edge. The separation point position is free contrary to the oblique trailing edge. The collision between the upper and lower vortices also is observed. However, the spatial phase shift between the upper and lower vortex at their generation point can be different due to the being free the separation point at suction side of trailing edge contrary to the oblique trailing edge



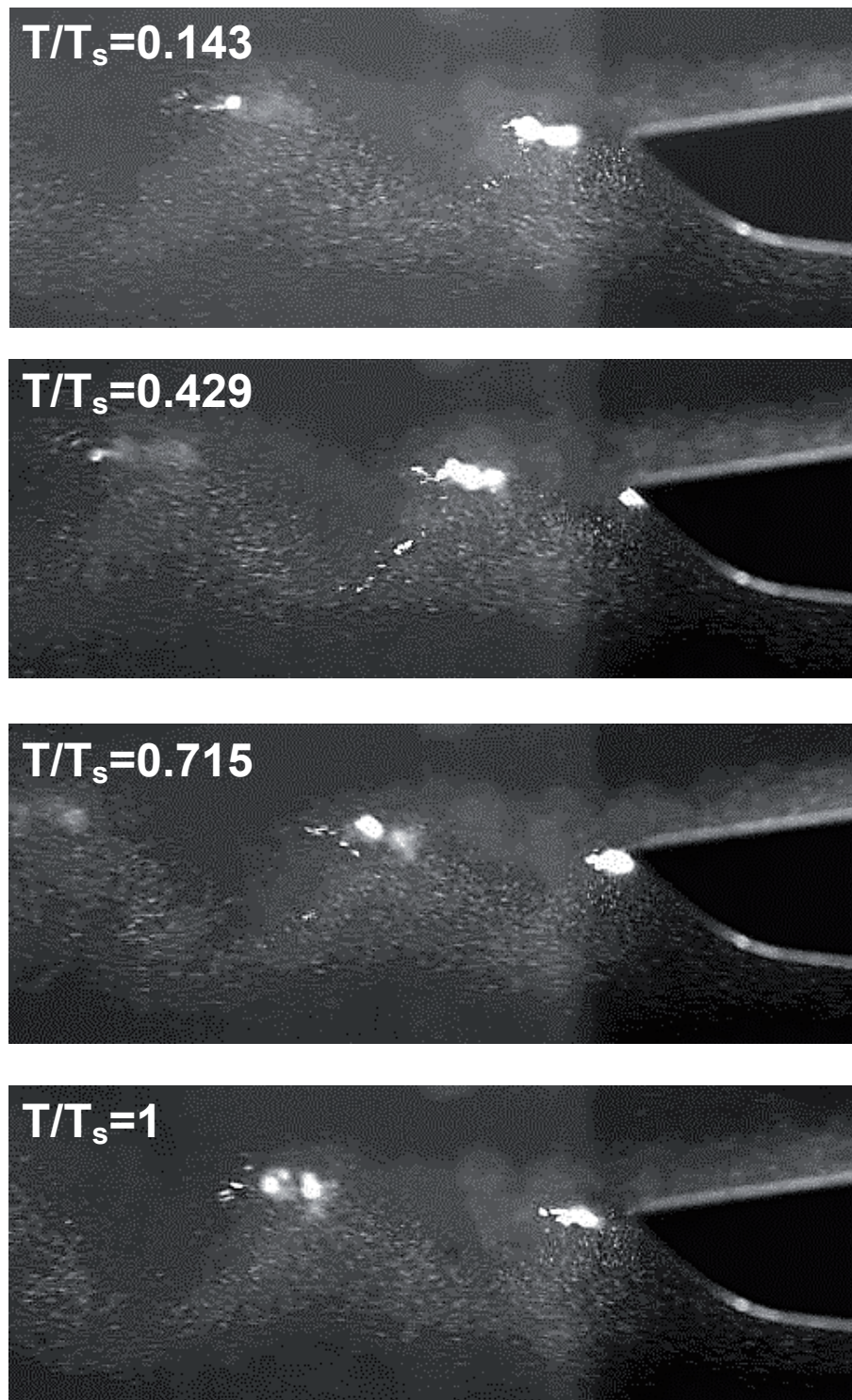


Figure 8.6: Visualization of the wake dynamics, Donaldson T. E.,  $Re_L = 1.5 \cdot 10^6$ ,  $\sigma = 0.8$



# Chapter 9

## Effect of trailing edge shape on wake flow

In this chapter, the effects of boundary layer state on the wake flow under lock-in condition are investigated for oblique and Donaldson trailing edges. Instantaneous velocity profiles at the passage time of the vortex are presented using LDV phase-locked average in the case of the oblique trailing edge. In addition, vortex characteristics along the wake are revealed. Moreover, the time-averaged velocity profiles under lock-in condition are revealed for oblique and Donaldson trailing edges.

### 9.1 LDV phase-locked average: Lock-in

Wake flow velocity under lock-in condition in the case of tripped transition is surveyed using LDV phase-locked average at different positions along the wake of oblique and Donaldson trailing edges.

#### 9.1.1 Instantaneous velocity profiles at the passage time of the vortex

Instantaneous stream wise velocity profiles at the passage time of the upper and lower vortices through the measurement line are illustrated in the case of natural,  $Re_L = 1.5 \cdot 10^6$ , and tripped transition,  $Re_L = 1.7 \cdot 10^6$ , for the oblique trailing edge in Figure 9.1. Similar to natural transition, the distance between the low and high stream wise velocities is determined as the vortex core diameter. In the case of the tripped transition, the size of upper and lower vortices increases. Similar to the natural transition, a larger vortex core diameter is found for the lower vortex.

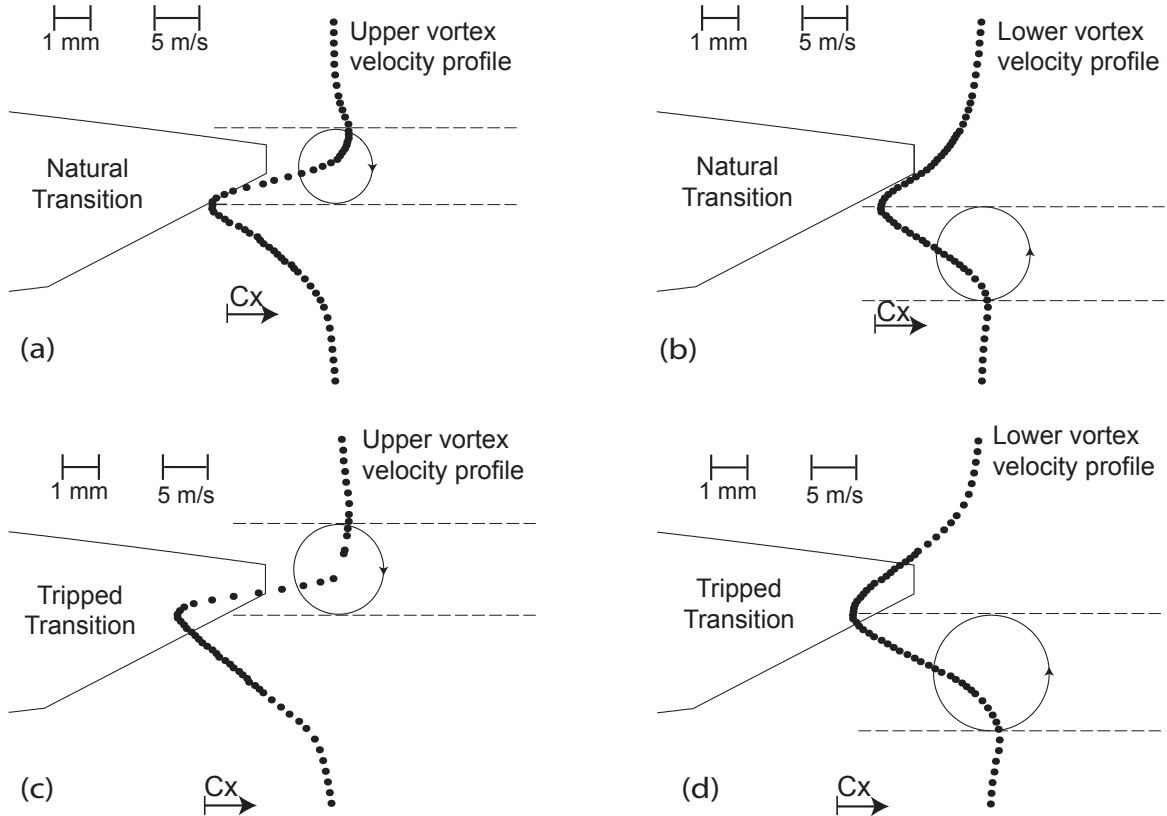


Figure 9.1: Instantaneous velocity profiles at the passage time of the vortex through the measurement line and vortex core size for the oblique trailing in the case of natural and tripped transition

Stream wise LDV phase-locked average was also performed under lock-in condition,  $Re_L = 1.5 \cdot 10^6$ , in the case of Donaldson trailing edge. However, two vortices are not defined near the wake similar to the oblique trailing edge one. Transverse LDV phase-locked average is performed in the case of oblique and Donaldson trailing edges to find more information about the vortices in the near wake. As the upper and the lower vortices pass through the measurement line at  $x/L = 1.022$ , in a vortex shedding period two peaks correspond to the positive tangential transverse velocity component of two vortices are detected. The maximum transverse velocity in a vortex shedding period is plotted in Figure 9.2 for the oblique and Donaldson trailing edges. The presence of two peaks in one vortex shedding period shows the passage of two vortices through the measurement line in the near wake, one corresponds to upper vortex and the other one to lower vortex, in the case of oblique trailing edge, Figure 9.2a. However, in the case of Donaldson trailing edge, 9.2b, only one peak is observed in one vortex shedding period that indicates the passage of one vortex. It could be concluded that in the case of oblique trailing edge after the collision between the upper and the lower vortices in the near wake, two vortices shed in the wake with different core diameter. However, in the case of Donaldson trailing edge due to the being free the separation point on the lower side of trailing edge, a smaller spatial phase shift between the lower and upper separation point is observed in comparison to the oblique one. As a result, the passage of one vortex, combination of upper and lower

vortex, is observed in the near wake after the collision between two vortices.

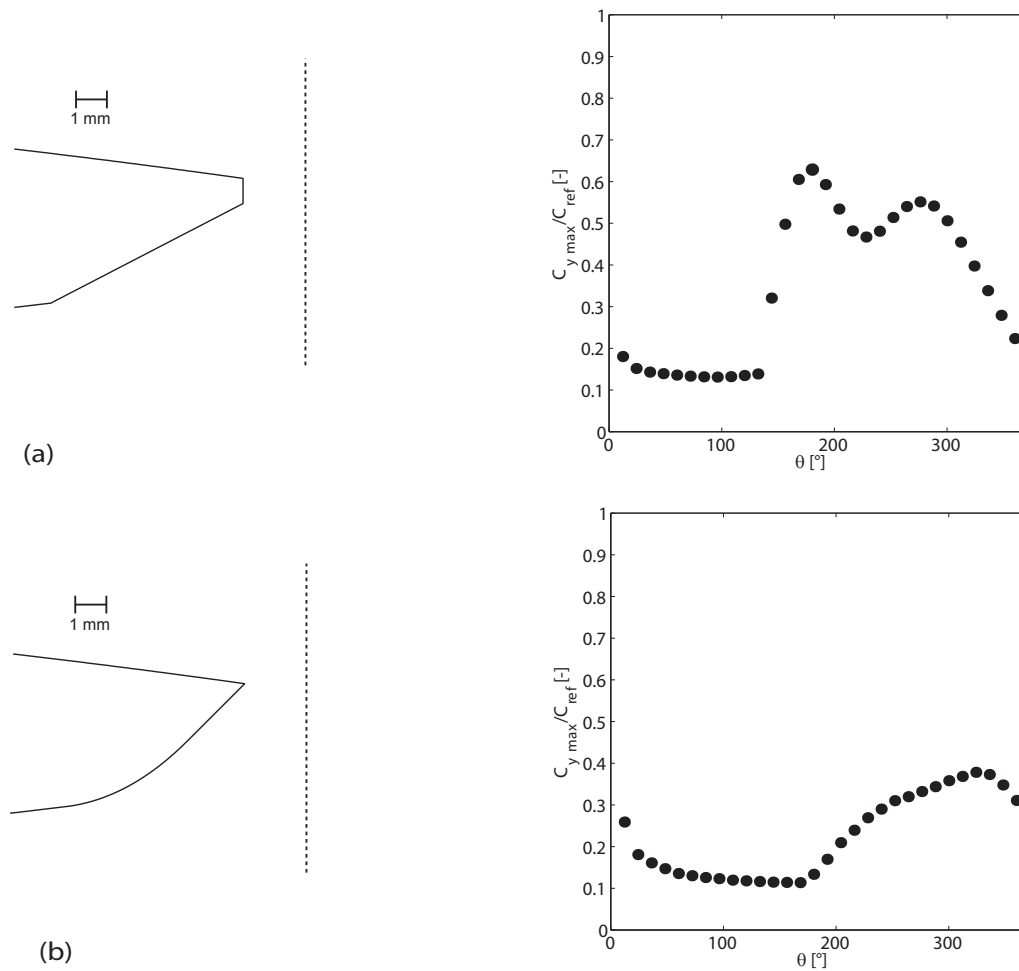


Figure 9.2: Maximum transverse velocity in one vortex shedding period in the case of a) Oblique,  $Re_L = 1.7 \cdot 10^6$ , and b) Donaldson trailing edges,  $Re_L = 1.5 \cdot 10^6$ ,  $x/L = 1.022$

The maximum transverse velocity in one vortex shedding is plotted at three position along the wake of Donaldson trailing edge,  $x/L = 1.022$ ,  $x/L = 1.062$ , and  $x/L = 1.152$ , Figure 9.3. As it was noted near the wake,  $x/L = 1.022$ , only one peak is observed. However, two peaks appear far from the trailing edge.

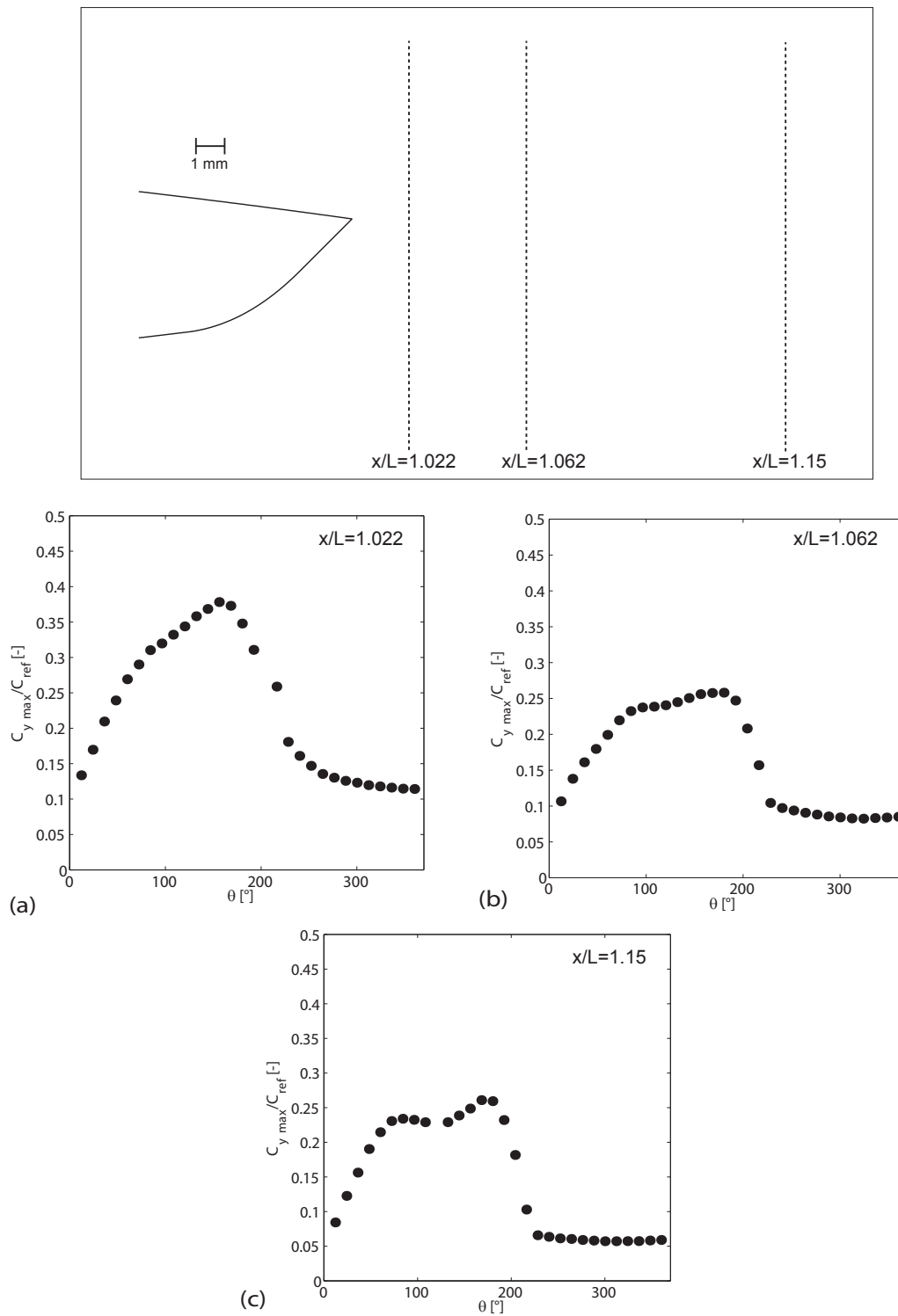


Figure 9.3: Maximum transverse velocity in one vortex shedding period in the case of Donaldson trailing edge, lock-in, a)  $x/L = 1.022$ , b)  $x/L = 1.062$ , c)  $x/L = 1.152$

### 9.1.2 Vortex characteristics

The normalized vortex core radius evolution along the wake of the oblique trailing edge is presented in Figure 9.4 in the case of natural and tripped transition. The radius of the vortices becomes larger along the wake for both trailing edges. However, the radius of the vortices in the case of tripped transition is larger than the natural transition. Moreover, a greater vortex core size is observed for the lower vortex street along the wake of tripped transition than the upper vortex street. The advection velocity of the vortices,  $C_{adv}$ , and the velocity at the edge of the vortex viscous core,  $C_t$ , along the wake of the oblique trailing edge are calculated in the case of tripped transition. In addition, the results are compared with the natural transition case. The advection velocity evolution along the wake for both cases are presented in Figure 9.5. In both cases the upper vortex street has a higher advection velocity than the lower vortex street. The difference between the advection velocity of upper and lower vortices becomes smaller far the wake.

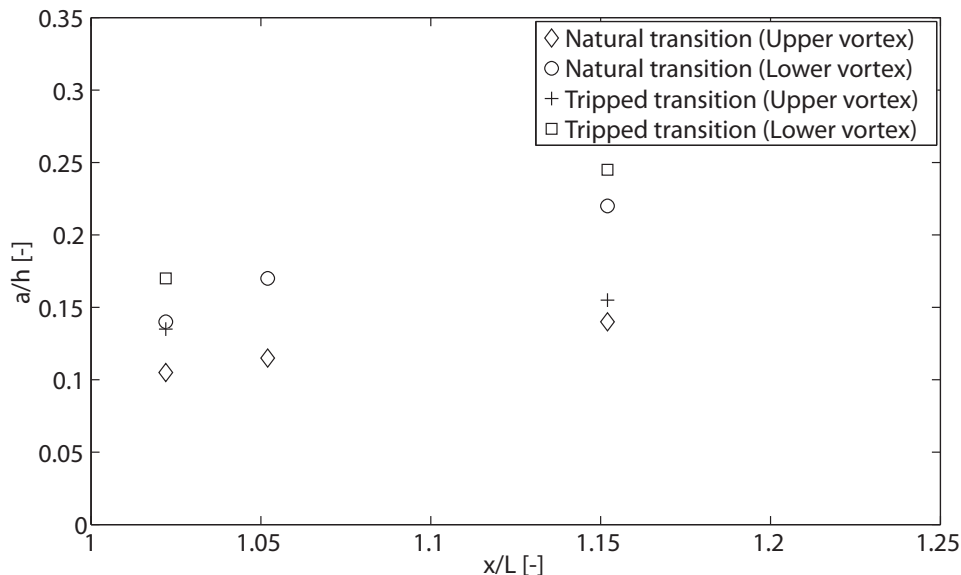


Figure 9.4: Normalized vortex core radius at different stations downstream of the oblique trailing edge, natural transition,  $Re_L = 1.3 \cdot 10^6$ , tripped transition,  $Re_L = 1.7 \cdot 10^6$

The evolution of normalized vortex strength along the wake in the case of natural and tripped transition is illustrated in the Figure 9.6. An increase in strength is found for tripped transition. However, nearly the same vortex strength value is observed for upper and lower vortex street in the case of natural and tripped transition.

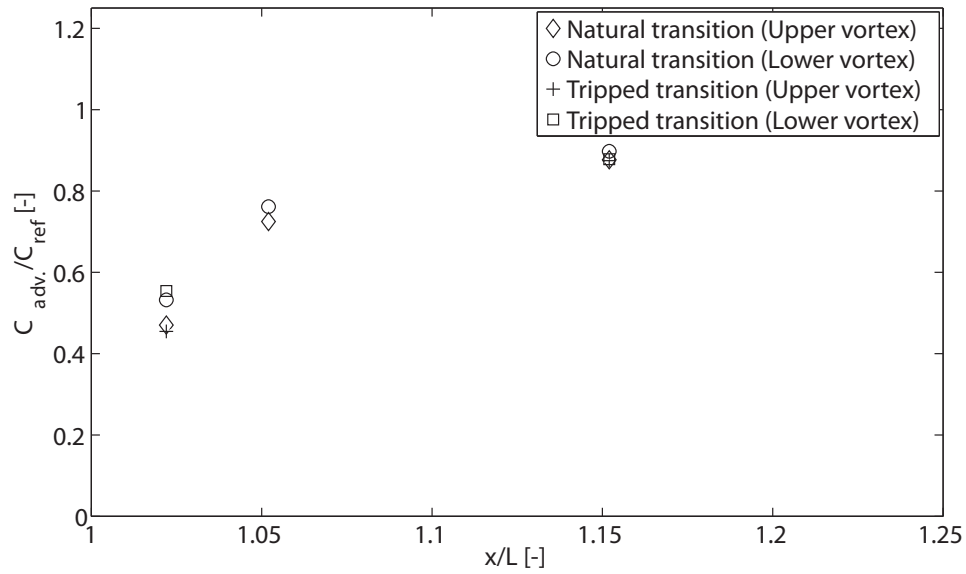


Figure 9.5: Normalized vortex advection velocity at different stations downstream of the oblique trailing edge, natural transition,  $Re_L = 1.3 \cdot 10^6$ , tripped transition,  $Re_L = 1.7 \cdot 10^6$

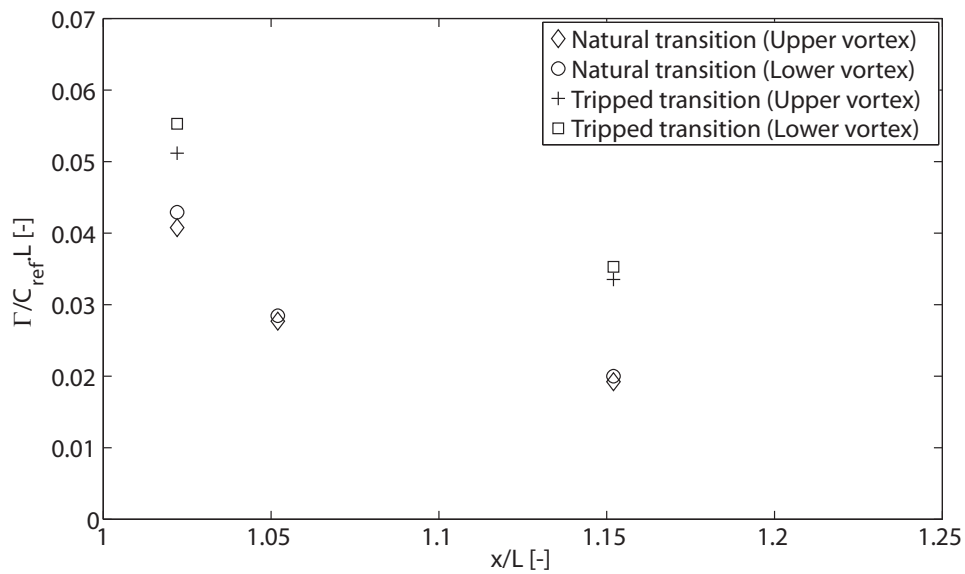


Figure 9.6: Normalized vortex strength at different stations downstream of the oblique trailing edge, natural transition,  $Re_L = 1.3 \cdot 10^6$ , tripped transition,  $Re_L = 1.7 \cdot 10^6$



## 9.2 Time-averaged velocity profiles

LDV measurements are performed at different positions along the wake in the context of tripped transition. Normalized by the free-stream velocity, the mean stream wise velocity and the stream wise velocity fluctuations are illustrated in Figures 9.7 and Figure 9.8 for the oblique and Donaldson trailing edges. In both cases, as the flow progresses downstream of trailing edge, the velocity deficit is reduced with slight asymmetric thickening of the wake downward. Moreover, the spreading of the lower part of the wake shows thickening of the core of lower vortices. However, the lower part of the wake for Donaldson trailing edge is thicker than for the oblique case. It is concluded that lower vortex core radius in the case of the Donaldson trailing edge should be larger than that for the oblique trailing edge. The stream wise velocity fluctuations are characterized by peaks produced by the passing of the upper and lower vortices. In the case of oblique and Donaldson trailing edges a higher velocity fluctuation is found for the lower peak. In addition, more turbulence appears in the center part of the wakes. It is believed that this is due to the collision between upper and lower vortices. It is concluded that the same phenomenon for the natural transition happens in the case of tripped transition. In addition, similar wake development is observed for both natural and tripped transition. However, the difference could be detected only in the vortex properties.

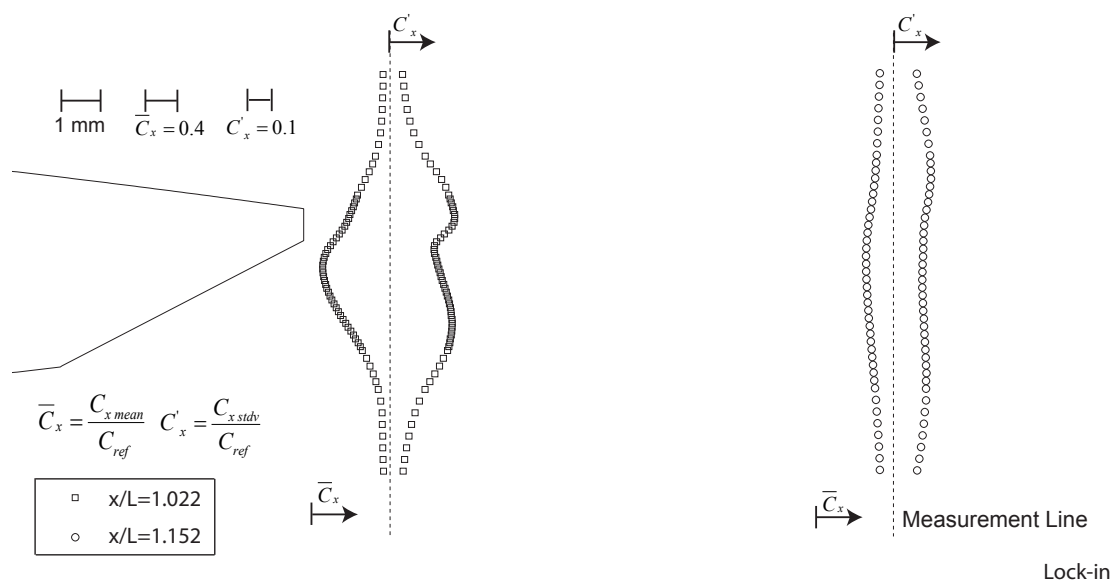


Figure 9.7: Traverse measurements along the wake at different stations under lock-in condition, normalized mean stream wise velocity and stream wise velocity fluctuations for oblique trailing edge, tripped transition

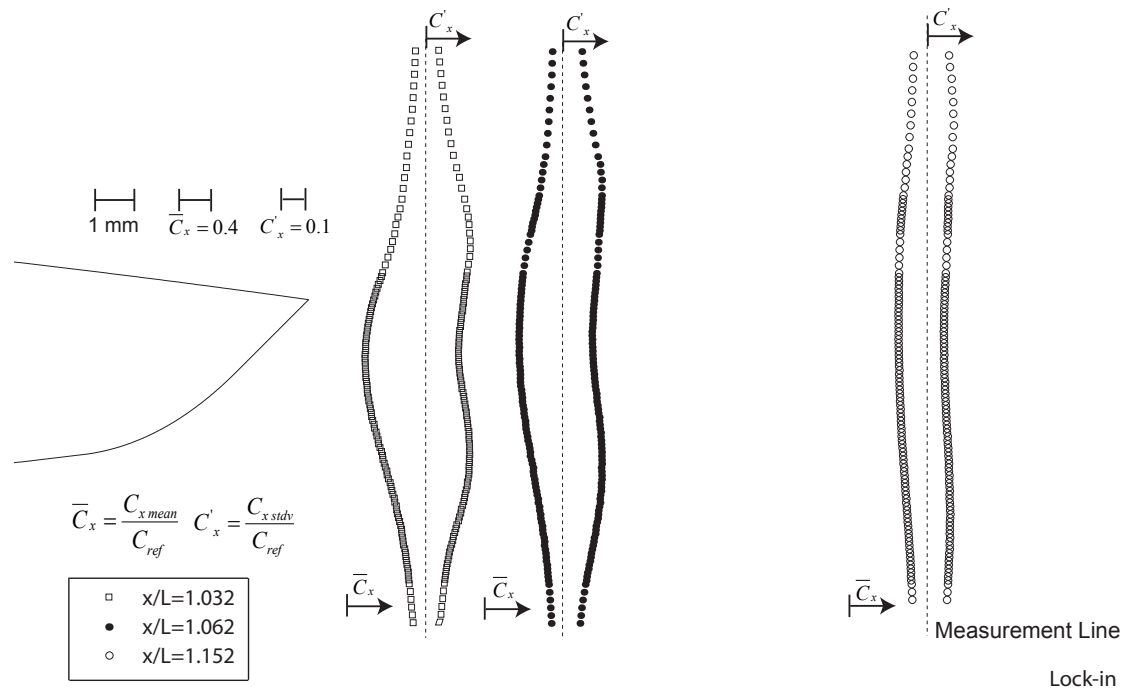


Figure 9.8: Traverse measurements along the wake at different stations under lock-in condition, normalized mean stream wise velocity and stream wise velocity fluctuations for Donaldson trailing edge, tripped transition

# Part V

## Conclusions and Perspectives



# Chapter 10

## Conclusions

In the present study, an experimental investigation of vortex shedding dynamics is carried out in the wake of oblique and Donaldson trailing edges hydrofoil to understand the phenomenon and the reasons for vibration reduction. This phenomenology could help optimize the trailing edge shape and obtain lower levels of vortex-induced vibration. Hydrofoils with oblique and Donaldson trailing edges are tested in high-speed cavitation tunnel at zero angle of attack and high Reynolds number,  $Re_L = 5 \cdot 10^5 - 3 \cdot 10^6$ . A velocity survey is performed via Laser Doppler Velocimetry, LDV, and Particle Image Velocimetry, PIV, using Proper-Orthogonal-Decomposition, POD, for post-processing. Besides, flow induced vibration measurements and high-speed visualizations are performed. In addition, the effects of a tripped boundary layer transition on the wake are investigated and compared with the condition of a natural boundary layer transition.

Vortex-induced vibration is found to decrease significantly for oblique and Donaldson trailing edges in comparison to the truncated case for the smooth and rough cases. However, the minimum vibration corresponds to the Donaldson trailing edge. The high-speed videos clearly demonstrate that for three tested hydrofoils the alternate vortices clearly detach from upper and lower corners of the trailing edge. However, for the oblique and Donaldson trailing edges the location of the lower vortex detachment is obviously shifted upstream with respect to the upper one. As a result, when the upper vortex rolls up, it coincides with the passage of the lower vortex, leading to their collision. This strong interaction leads to a redistribution of the vorticity, which does not concentrate within the core of Karman vortices any more. However, the collision between the vortices is more pronounced in the case of Donaldson trailing edge in comparison to the oblique trailing edge.

LDV phase-locked average measurement under lock-in condition for the oblique trailing edges shows the passage of two vortices after the collision in the near wake corresponding to the upper and lower vortices. A larger vortex core diameter is found for the lower vortex, contrary to the truncated trailing edge where the upper and lower vortices have the same core diameter. In addition, the unequal distance between the lower vortex and two neighboring upper vortices in the near wake, introduced by the oblique truncation of the trailing edge, is found to vanish in the far wake, where more organized shedding is recovered, as observed with the blunt trailing edge. In the case of Donaldson trailing edge LDV phase-locked average measurement in transverse direction shows the passage of one vortex after the collision in the near wake. However, the passage of two vortices corresponding to the upper and lower vortex, is found far from the trailing edge.

Under lock-off condition and in the case of oblique and Donaldson trailing edges, the evolution of velocity deficit and velocity fluctuation peaks shows the same results as lock-in condition such as an asymmetric wake, reduce of deficit velocity along the wake, and higher velocity fluctuation for lower vortex street in comparison to the truncated case. Nearly the same wake width is found for truncated and oblique trailing edges with a slight asymmetric thickening of the wake, downward in the case of the oblique trailing edge. However, in the case of Donaldson trailing edge the wake width increases significantly. Moreover, the minimum stream wise and transverse velocity fluctuation profile between three trailing edges corresponds to the Donaldson trailing edge.

The comparison between the boundary layer velocity profiles on the suction and pressure sides of Donaldson trailing edge reveals the thicker boundary layer for pressure side. In addition, the laminar-to-turbulent transition appears on the pressure side before the suction one. This is in contrary to the truncated trailing edge that the laminar-to-turbulent transition location is the same for both sides of hydrofoil. Moreover, the boundary layer velocity profiles comparison between the suction side of truncated and Donaldson trailing edges reveals a thicker boundary layer in the case of Donaldson trailing edge. It could be due to the collision between the upper and lower vortices.

The tripped transition investigation shows that the collision between the upper and lower vortices is also observed in this case, However, the vortex core diameter is larger, vortex strength is greater, vortex shedding is lower, and vortex-induced vibration increases in comparison to the natural transition.

At the end, these investigations let us believe that the collision between upper and lower vortices and the resulting vorticity redistribution is the main reason for the vibration reduction obtained with oblique and Donaldson trailing edges. This result opens the way for more effective hydrofoil geometry optimization for further reduction of flow induced vibration.

# Chapter 11

## Perspectives

Hydrofoil trailing edge geometry has direct effect on the wake dynamics and flow-induced vibration. The present study has shown that the Oblique and Donaldson trailing edges reduce the flow-induced vibration in comparison to the truncated trailing edge. However, there are some important issues which should be clearly studied:

### **Fluid-structure coupling**

The maximum flow-induced vibration is found under lock-in condition where the vortex shedding frequency coincidences with the hydrofoil eigen frequency and it is locked on a range of free-stream velocity. For industrial applications, avoiding the lock-in is an important issue. The results show that the Donaldson trailing edge offers a significant reduction of the vibration shape and also prevents the occurrence of the lock-in. The strong collision between upper and lower vortices and the resulting vorticity redistribution reduces the vibration amplitude. As a result the velocity range under lock-in condition becomes smaller. This explanation can be a reason that no lock-in was found. However, further investigations can be performed on the lock-in dynamic including free-stream velocity range, hysteresis effects and fluid damping to find the main effective parameters on the lock-in condition.

### **Oblique and Donaldson trailing edge hydrofoil mounting on the hydraulic machine model testing**

The hydraulic turbines containing a casing with stay vanes face the potential dynamic problem of stay vane vortex shedding. For hydraulic efficiency purposes the stay vanes tend to be relatively slender in the direction normal to the flow thus being flexible in this direction. As a result structural vibrations may be excited by the vortex shedding at the trailing edge of the vanes. When the excitation frequency coincides with one of the natural frequencies of the stay vane, resonance occurs, which potentially initiates premature cracks. Experimental investigations on Oblique and Donaldson trailing edges hydrofoil in the high speed cavitation tunnel shown a significant vibration reduction in comparison to the truncated one. Oblique and Donaldson trailing edges hydrofoil could be mounded on the hydraulic machine model testing to verify the vibration reduction that was found in the high speed cavitation tunnel. Besides, the effect of these trailing edge geometry on the hydrodynamic performances and efficiency of the hydraulic machine

model testing can be investigated .

### **Numerical Simulation validation and trailing edge geometry optimization**

Despite the mentioned experimental investigation and phenomenology behind the flow-induced vibration using oblique and Donaldson trailing edges, the numerical computations have still to be validated for this specific case. The trailing edge geometry can be optimized using the validated numerical simulation to find the minimum flow-induced vibration without altering the hydrodynamic performances. The optimized geometry could be tested in the High Speed cavitation Tunnel to verify the numerical simulation results and perform further investigation.



# References



# References

- [1] ADRIAN, R. J. Twenty years of particle image velocimetry. *Experiments in Fluids* 39 (2005), 159–169.
- [2] ALBRECHT, H., BORYS, M., DAMASCHKE, N., AND TROPEA, C. *Laser doppler and phase doppler measurement techniques*. Springer, 2003.
- [3] AUSONI, P. *Turbulent vortex shedding from a blunt trailing edge hydrofoil*. PhD thesis, EPFL, N° 4475, 2009.
- [4] AUSONI, P., FARHAT, M., ESCALER, X., EGUSQUIZA, E., AND AVELLAN, F. Cavitation influence on von Kármán vortex shedding and induced hydrofoil vibrations. *Journal of Fluids Engineering, Transactions of the ASME* 129, 8 (2007), 966–973.
- [5] AVELLAN, F., HENRY, P., AND RHYMING, I. A new high speed cavitation tunnel for cavitation studies in hydraulic machinery. In *American Society of Mechanical Engineers, Fluids Engineering Division FED* (1987), vol. 57, pp. 49–60.
- [6] BEARMAN, P. W. Investigation of flow behind a 2-dimensional model with a blunt trailing edge and fitted with splitter plates. *Journal of Fluid Mechanics* 21, Part 2 (1965), 241–255.
- [7] BEARMAN, P. W. The effect of the base bleed on the flow behind a two-dimensional model with a blunt trailing edge. *Aeronautical Quarterly* 18 (1967), 207–224.
- [8] BEARMAN, P. W. Vortex shedding from oscillating bluff bodies. *Annual review of fluid mechanics* 16 (1984), 195–222.
- [9] BEARMAN, P. W., AND OWEN, J. C. Reduction of bluff-body and suppression of vortex shedding by the introduction of wavy separation lines. *Journal of Fluids and Structures* 12 (1998), 123–130.
- [10] BENDAT, J., AND PIERSON, A. *Random data: Analysis and measurement procedures*. Wiley-Interscience, John Wiley, 1971.
- [11] BENNEY, D. J., AND LIN, C. C. On the secondary motion induced by oscillations in a shear flow. *Physics of Fluids* 3 (1960), 656–657.
- [12] BERKOOZ, G. E. A. The proper orthogonal decomposition in the analysis of turbulent flows. *Annual Review of Fluid Mechanics* 25 (1993), 539–575.
- [13] BLAKE, W. K. *Mechanics of flow induced sound and vibration*. Academic Press INC, Orlando, United States of America, 1986.

- [14] BLOOR, M. S. The transition to turbulence in the wake of a circular cylinder. *Journal of Fluid Mechanics* 19, 2 (1964), 290–304.
- [15] BUCHHAVE, P., GEORGE JR., W. L., AND LUMLEY, J. L. The measurement of turbulence with the laser-doppler anemometer. *Annual Review of Fluid Mechanics* 11 (1979), 443–503.
- [16] DAVIES, M. E. Comparison of the wake structure of a stationary and oscillating bluff body, using a conditional averaging technique. *Journal of Fluid Mechanics* 75, MAY27 (1976), 209–231.
- [17] DONALDSON, R. M. Hydraulic turbine runner vibration. *Journal of Engineering for Power* 78 (1956), 1141–1147.
- [18] DRYDEN, H. L. Review of published data on the effect of roughness on transition from laminar to turbulent flow. *Journal of the Aeronautical Sciences* 20, 7 (1953), 477–482.
- [19] DURAO, D. F. G. E. A. Bias effects in laser doppler anemometry. *Journal of physics. E, Scientific instruments* 13 (1980), 442–445.
- [20] DURST, F. E. A. *Principles and Practices of Laser-Doppler Anemometry*. Academic Press, 1981.
- [21] DWAYNE, A. E. A. Vortex shedding from a hydrofoil at high reynolds number. *Journal of Fluid M* 531 (2005), 293–324.
- [22] FAGE, A.; JOHANSEN, F. C. On the flow of air behind an inclined flat plate of infinite span. *Proceedings of the Royal Society of London. Series A, Containing Papers of a Mathematical and Physical Character* 116 (1927), 170–197.
- [23] FASEL, H. Investigation of the stability of boundary layers by a finite-difference model of navier-stokes equations. *Journal of Fluid Mec* 78 (1976), 355–383.
- [24] FISHER, R. K. E. A. Stayvane vibrations in the nkula falls turbines. *Hydropower & Dams* (1994), 15–20.
- [25] GERRARD, J. H. The mechanics of the formation region of vortices behind bluff bodies. *Journal of Fluid Mechanics* 25, Part 2 (1966), 401–413.
- [26] GILBERT, S., AND SIGURDSON, L. Hydrogen bubble flow visualization of a self-oscillating cylinder vortex street void. *Physics of Fluids* 17, 9 (2005), 091104.
- [27] GOLDWAG, E., AND BERRY, D. G. Von Kármán hydraulic vortices cause stay vane cracking on propeller turbines at Little Long generating station of Ontario Hydro. *Journal of Engineering for Power* 90, 3 (1968), 213–217.
- [28] GRAFTIEAUX, L. E. A. Combining piv, pod and vortex identification algorithms for the study of unsteady turbulent swirling flows. *Measurement science & technology* 12 (2001), 1422–1429.

- [29] GREENWAY, M. E., AND WOOD, C. J. The effect of a bevelled trailing edge on vortex shedding and vibration. *Journal of Fluid Mechanics* 61(2) (1973), 323–355.
- [30] GREIN, H., AND STAEHLE, M. Rupture par fatigue d’entretoises d’avant-distributeurs de grandes turbines. *Bulletin Escher Wyss* 1 (1978), 33–37.
- [31] GRIFFIN, O. M. Flow similitude and vortex lock-on in bluff body near wakes. *Physics of Fluids A* 1, 4 (1989), 697–703.
- [32] GRIFFIN, O. M. A note on bluff body vortex formation. *Journal of Fluid Mechanics* 284 (1995), 217–224.
- [33] GUMMER, J. H., AND HENSMAN, P. C. A review of stayvane cracking in hydraulic turbines. *Water Power and Dam Construction* 44(8) (1992), 32–42.
- [34] HERBER, T. On finite amplitudes of periodic disturbances of the boundary layer along a flat plate. *Lecture Notes in physics* 35 (1975), 212–17.
- [35] HERBERT, T. Secondary instability of the boundary layers. *Annual Review of Fluid Mechanics* 20 (1988), 487–526.
- [36] HERRIN, J. L., AND DUTTON, J. C. An investigation of ldv velocity bias correction techniques for high-speed separated flow. *Experiments in Fluids* 14 (1993), 354–363.
- [37] HESKESTAD, F., AND OLBERTS, D. R. Influence of trailing edge geometry on hydraulic-turbine blade vibration. *Journal of Engineering for Power* 82 (1960), 103–110.
- [38] HOOKER, S. G. On the action of viscosity in increasing the spacing ratio of a vortex street. *Proceedings of the Royal Society of London. Series A, Mathematical and Physical Sciences* 154 (1936), 67–89.
- [39] HWANG, J. Y. E. A. Reduction of flow-induced forces on a circular cylinder using a detached splitter plate. *Physics of Fluids* 15 (2003), 2433–2436.
- [40] KACHANOV, Y. S. Physical mechanism of laminar boundary layer transition. *Annual Review of Fluid Mechanics* 26 (1994), 411–482.
- [41] KERHO, M., AND BRAGG, F. Airfoil boundary layer development and transition with large leading edge roughness. *AIAA J* 35 (1997), 75–84.
- [42] KIM, W., YOO, J. Y., AND SUNG, J. Dynamics of vortex lock-on in a perturbed cylinder wake. *Physics of Fluids* 18, 7 (2006), 074103.
- [43] KLEBANOFF, P. S. E. A. The three-dimensional nature of boundary-layer stability. *Journal of Fluid Mechanics* 12 (1962), 1–34.
- [44] KONSTANTINIDIS, E. E. A. The timing of vortex shedding in a cylinder wake imposed by periodic inflow perturbation. *Journal of F* 543 (2005), 45–55.
- [45] KOVASZNAVY, L. Hot wire investigations of the wake behind cylinders at low reynolds numbers. *Proceedings of the Royal Society of London* 198 (1949), 174–190.

- [46] LAMB, H. *Hydrodynamics*. Cambridge University Press, 1924.
- [47] LIENHARD, J. *Synopsis of lift, drag, and vortex frequency data for rigid circular cylinders*. 1966.
- [48] LIESS, C. The cause and avoidnace of vortex-excited vibrations of turbine stayvanes. *Voith Research and Construction No 32e* (1986).
- [49] LOCKEY, K. J., KELLER, M., SICK, M., STAEHLE, M. H., AND GEHRER, A. Flow-induced vibrations at stay vanes: Experience on site and CFD simulations. *The International Journal on Hydropower and Dams* 5 (2006), 102–106.
- [50] MA, X. E. A. Dynamics and low-dimensionality of a turbulent near wake. *Journal of Fluid Mechanics* 410 (2000), 29–65.
- [51] MARRIS, A. A review on vortex streets, periodic waxes, and induced vibration phenomena. *Journal of Basic Engineering* 86 (1964), 185.
- [52] MOSALLEM, M. Numerical and experimental investigation of beveled trailing edge flow fields. *Journal of Hydrodynamics* 20 (2008), 273–279.
- [53] N., I. Spatial growth of finite wave disturbances in parallel and nearly parallel flows. *Transactions of the Japan Society of Aeronautics and Space Sciences* 17 (1974), 160–174.
- [54] NAUDASCHER, E., AND ROCKWELL, D. *Flow-induced vibrations: An engineering guide*. Blakema publishers, 1994.
- [55] OUDHEUSDEN, B. W. E. A. Phase-resolved characterization of vortex shedding in the near wake of a square-section cylinder at incidence. *Experiments in Fluids* 39 (2005), 86–98.
- [56] OZONO, S. Flow control of vortex shedding by a short splitter plate asymmetrically arranged downstream of a cylinder. *Physics of Fluids* 11 (1999), 2928–2934.
- [57] PARK, D. S., LADD, D. M., AND HENDRICKS, E. W. Feedback control of von Kármán vortex shedding behind a circular cylinder at low Reynolds numbers. *Physics of Fluids* 6 (1994), 2390.
- [58] PETRIE, H. L. E. A. Laser-doppler bias in separated turbulent flows. *Experiments in Fluids* 6 (1988), 80–88.
- [59] POPE, S. B. *Turbulent Flows*. Cambridge University Press, 2000.
- [60] RAFFEL, M. A. A. *Particle Image Velocimetry: A Practical Guide*. Springer, Berlin Heidelberg New York, 1998.
- [61] ROCKWELL, D. Vortex-body interactions. *Annual Review of Fluid Mechanics* 30 (1998), 199–229.
- [62] ROSENHEAD, L. Double row of vortices with arbitrary stagger. *Mathematical Proceedings of the Cambridge Philosophical Society* 25 (1929), 132–138.

- [63] ROSENHEAD, L. An experimental investigation of the flow behind circular cylinders in channels of different breadths. *Proceedings of the Royal Society of London. Series A, Containing Papers of a Mathematical and Physical Character* 129 (1930), 115–135.
- [64] ROSHKO, A. On the development of the turbulent wakes from vortex streets. *National Advisory Committee for Aeronautics* 1191, 2 (1954), 1–25.
- [65] SARPKAYA, T. A critical review of the intrinsic nature of vortex-induced vibrations. *Journal of Fluids and Structures* 19(4) (2004), 389–447.
- [66] SCHAEFFER, J. W., AND ESKINAZI, S. An analysis of the vortex street generated in a viscous fluid. *Journal of Fluid Mechanics* 6, 2 (1959), 241–260.
- [67] SCHLICHTING, H., AND GERSTEN, K. *Boundary layer theory*. McGraw-Hill Series in Mechanical Engineering, McGraw-Hill, 1979.
- [68] SIROVICH, L. Turbulence and the dynamics of coherent structures. *Quarterly of Applied Mathematics* 45 (1987), 561–571.
- [69] TANEDA, S. Experimental investigation of the wakes behind cylinders and plates at low Reynolds numbers. *Journal of Physical Society Japan* 11(3) (1956), 302–307.
- [70] TANI, I. Boundary layer transition. *Annual Review of Fluid Mechanics* 1 (1969), 169–196.
- [71] TANNER, M. A method for reducing the base drag of wings with blunt trailing edge. *Aeronaut Quart* 23 (1972), 15–23.
- [72] TOEBES, G. H. Hydroelastic vibrations of flat plates related to trailing edge geometry. *Journal of Basic* (1961), 671–678.
- [73] TOLLMIE, W. die entstehung der turbulenz. *Nachr. Ges. Wiss. Göttingen Math.-Phys* (1929), 21–44.
- [74] TOMBAZIS, N., AND BEA. A study of three-dimensional aspects of vortex shedding from a bluff body with a mild geometric disturbance. *Journal of Fluid* 330 (1997), 85–112.
- [75] TRITTON, D. J. Experiments on the flow past a circular cylinder at low Reynolds number. *Journal of Fluid Mechanics* 6 (1959), 547–567.
- [76] VON KÁRMÁN, T. Ueber den Mechanismus des Widerstandes, den ein bewegter Körper in einer Flüssigkeit erfährt. *Nachrichten von der Gesellschaft der Wissenschaften zu Göttingen Mathematisch-Physikalische Klasse* (1912), 547–556.
- [77] VONLANTHEN, R. Dynamique des structures tourbillonnaires dans le sillage. Master’s thesis, EPFL, 2005.
- [78] WHITE, F. M. *Viscous fluid flow*. McGraw-Hill Inc., New York, 1974.
- [79] WILCOX, D. C. *Basic Fluid Mechanics*. DCW Industries, 1997.

- [80] WILLIAMSON, C. H. K. Vortex dynamics in the cylinder wake. *Annual Review of Fluid Mechanics* 28 (1996), 477–539.
- [81] WILLIAMSON, C. H. K., AND GOVARDHAN, R. Vortex-induced vibrations. *Annual Review of Fluid Mechanics* 36 (2004), 413–455.
- [82] WILLIAMSON, C. H. K., AND ROSHKO, A. Vortex formation in the wake of an oscillating cylinder. *Journal of Fluids and Structures Volume 2, Issue 4* (1988), 355–381.
- [83] WOOD, C. The effect of base bleed on a periodic wake. *Journal of Royal Aeronautical Society* 68 (1964), 477–482.
- [84] ZHANG, Q., LEE, S. W., AND LIGRANI, P. M. Effects of surface roughness and freestream turbulence on the wake turbulence structure of a symmetric airfoil. *Physics of Fluids* 16, 6 (2004), 2044–2053.



# Curriculum Vitae

## Amirreza Zobeiri

Av. de Rosemont 3  
1006 Lausanne (VD)

Tél. Prof.: +41 21 311 69 16  
Portable: +41 78 893 86 30  
E-mail: amirreza.zobeiri@gmail.com

### Education

---

2007-2011: **PhD in mechanical engineering**  
École polytechnique fédérale de Lausanne (EPFL), Switzerland  
2004-2006: **Master in mechanical engineering**  
École polytechnique fédérale de Lausanne (EPFL), Switzerland  
1997-2002: **Bachelor in mechanical engineering**  
Tehran University, Iran

### Professional experience

---

2007-2011: **École Polytechnique Fédérale de Lausanne (EPFL), Suisse**  
**Laboratory for Hydraulic Machines (LMH)**  
Researcher and Project liaison of HYDRODYNA Project in collaboration with ALSTOM Hydro, VOITH Hydro, Swisselectric and UPC-CDIF) and HYDRODNET Project in collaboration with CCEM, Swisselectric, EMPA, and Hochschule Luzern  
2005-2006: **École Polytechnique Fédérale de Lausanne (EPFL), Suisse**  
**Heat and Mass Transfer Laboratory (LTCM)**  
Researcher and Project liaison of Solar Impulse Project  
2002-2003: **Hamed (technical engineering company), Iran**  
2000: **Schlumberger (Oil Company), Iran**

### Computer Skills

---

Matlab, Labview, Microsoft office, Fluent, Femlab, LaTeX, FDS

### Languages

---

English: Fluent (C2)  
German: Advanced (C2)  
French: Good (B2)  
Persian: Native language

## Publications

Zobeiri A., Ausoni, P., Avellan, F. and Farhat M., "How oblique trailing edge of a hydrofoil reduces the vortex-induced vibration", Journal of Fluids and Structures accepted for publication, 2011

Nicolet ch., Zobeiri A., Maruzewski P., Avellan, F., " Experimental Investigations on Upper Part Load Vortex Rope Pressure Fluctuations in Francis Turbine Draft Tube, International Journal of Fluid Machinery and Systems accepted for publication, Vol. 3, No. 1, January-March 2011

Ausoni P., Zobeiri A., Avellan F. and Farhat M., "Effect of boundary layer state on the vortex shedding", Journal of Fluids Engineering submitted for publication, 2011

Zobeiri, A. ; Ausoni, P. ; Avellan, F. ; Farhat, M., " Vortex shedding from blunt and oblique trailing edge hydrofoils", 3rd IAHR International Meeting of the Workgroup on Cavitation and Dynamic Problems in Hydraulic Machinery and Systems, Brno, vol. 1, 2009, p. 245-252

Zobeiri A., Ausoni, P., Avellan, F. and Farhat M., "Experimental investigation of the vortex shedding dynamic in the wake of oblique and blunt trailing edge hydrofoils using PIV-POD method", 7th International Symposium on Fluid-Structure Interactions, Flow-Sound Interactions and Flow-Induced Vibration and Noise, August 1-5, 2010, Montreal, Canada

Nicolet ch., Zobeiri A., Maruzewski P., Avellan, F., " On the Upper Part Load Vortex Rope in Francis Turbine: Experimental Investigation, 3rd 25th IAHR Symposium on Hydraulic Machinery and Systems, September 20-24, 2010, Timisoara, Romania

Zobeiri A., Avellan, F. and Farhat M., "The effect of hydrofoil trailing edge geometry on vortex shedding", IUTAM Symposium on Bluff Body Wakes and Vortex-Induced Vibrations, 22-25 June 2010 Capri Island, Italy

Zobeiri A., Ausoni, P., Avellan, F. and Farhat M., "Physics behind vortex-induced vibration reduction using oblique trailing edge", 63rd Annual Meeting of the APS Division of Fluid Dynamics Volume 55, Number 16, November 21-23, 2010, Long Beach, California

Zobeiri A., Avellan, F. and Farhat M., "Vortex shedding from a hydrofoil with two different trailing edge geometries", Proceedings of the 1st EPFL Doctoral Conference in Mechanics, Lausanne, February, 19, 2010